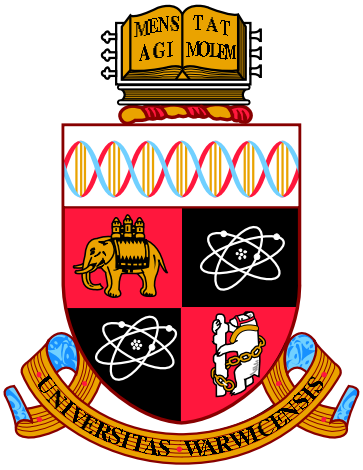

Physics of Biomembranes

by

Stefan Alexandru Rautu

Thesis

Submitted to the University of Warwick

for the degree of

Doctor of Philosophy

Department of Physics

April 2015

THE UNIVERSITY OF WARWICK

Contents

List of Tables

List of Figures

Acknowledgments

Usually a full paragraph of acknowledgements is included in a rather short four-page article that is published in the *Physical Review Letters* journal. By a simple scaling argument, this might naively suggest that I need to write here almost 30–40 paragraphs of acknowledgements. Since I am not willing to use this much space, for the sake of brevity (but also for the sake of my sanity!), I would like to use this opportunity to express as short as possible my sincere appreciation to a number of people that supported me and helped make this thesis possible.

Firstly, I would like to acknowledge both my supervisor, Matthew Turner, and George Rowlands, to whom I extend my heartfelt gratitude for their huge support throughout my doctoral studies, as both teachers and close friends. Notably, they have guided me with great patience, whilst also being hard working and meticulous. Above all, they have always acted with warmth and friendliness towards me which has helped making my research at Warwick very enjoyable. Also, thanks for all the casual and interesting conversations that we had over a couple of good beers in the famous *Virgins and Castle* (notoriously known for the game of spoof).

Secondly, I owe a debt of gratitude to Nina, Alex, Steph, and all the guys of PS.001, including Dan, Andy, Matt, Edu, Jack, Erick, and Anja. Thanks for your friendly support and all the laughs, and more importantly thank you for the numerous discussions ranging from utter silliness to refreshingly insightful topics.

Last but not least, I would like to thank my family for their best wishes and constant encouragement. In particular, I would like to give a special thanks to my eldest brother, Lucian, for his tremendous support throughout my life, for which I feel very privileged, and I am forever grateful.

Declarations

I hereby declare that my thesis entitled *Physics of Biomembranes* is the result of my own work, unless stated otherwise. This thesis is submitted to the University of Warwick as my application towards the degree of Doctor of Philosophy. It has been composed by myself and no part of this thesis has been submitted for a degree at any other university. This work has been carried out under the supervision of Prof. Matthew S. Turner and Prof. George Rowlands at the University of Warwick from October 2011 to April 2015. The following research work has been submitted to refereed journals for publication:

1. S. A. Rautu, G. Rowlands, and M. S. Turner, *Membrane Composition Variation and Underdamped Mechanics near Transmembrane Proteins and Coats*, Phys. Rev. Lett. **114**, 098101 (2015)

2. S. A. Rautu, D. Orsi, G. Rowlands, M. S. Turner, and P. Cicuta, *The Role of Optical Projection on Vesicle Fluctuations* [In preparation]

3. S. A. Rautu, G. Rowlands, and M. S. Turner, *Size-dependent Recycling in Non-equilibrium Membranes* [In preparation]

"*The road to wisdom?–Well, it's*
plain and simple to express:

Err
and err
and err again,
but less
and less
and less."

– Piet Hein (1940)

Abstract

The basic building blocks of all biomembranes are lipid molecules, which self-assemble to form a very thin and stable barrier, where a variety of proteins can be incorporated into its structure. These two-dimensional systems exhibit a plethora of physical phenomena, which are an abundant source of inspiration for a physicist. The physical aspects of biomembranes are described within a phenomenological model, the so-called Canhan–Helfrich theory, which relies primarily on the geometrical aspects of the membrane surface at large scales.

Using this theory, we study the response of a membrane to the inclusion of a transmembrane protein or a protein coat by coupling the composition to the mean curvature. A transition is found from an overdamped to an underdamped regime for the membrane shape and its compositional variation. This leads to large membrane undulations near the inclusion, resulting in the activity suppression of mechanosensitive channels and a preference for the formation of protein coats.

We also re-examine the methodology for inferring the bending modulus of membranes from their observed thermal fluctuations. Particularly, we analyse the effect due to the optical projection of such shape undulations across the focal depth of the microscope. A comparison of this with the literature approaches reveals a systematic decrease in the value of the bending modulus, resolving a previously recognised discrepancy between shape measurements and other known techniques.

Lastly, we investigate an non-equilibrium model for the formation of membrane domains that also involves membrane recycling. The dynamics and the steady-state features of the domain size distribution are analytically revealed and the implication to the heterogeneity observed in biomembranes is discussed.

Chapter 1

Introduction

The research area of biomembranes has become an important interdisciplinary meeting point for various fields of science and technology ranging from applied mathematics to nano-medicine. There are very good reasons for its wide appeal and interest. Firstly, its biological significance: each living cell, including their organelles, is bounded by a sac-like membrane that plays an active and crucial role in almost every cellular process. Membranes spatially separate intracellular compartments and define a boundary with the extracellular medium [1]. This compartmentalization is fundamental for an organism, allowing highly specialised functions [2]. Hence, a complete knowledge of membrane phisicochemical properties is essential for understanding the diverse phenomena observed in cells, which are the building blocks of all *living matter*. A few examples include the selective transport of ions across membranes through protein channels [3], regulation of the response to osmotic shock [4–6], cellular transport, signal transduction, cell adhesion, DNA replication, protein biosythesis [7], and the flow of red blood cells through narrow capillarities [8]. Many important medical problems also involve membranes, such as understanding the nerve pulse conduction and the mechanism of general anaesthesia [9]. Moreover, much of the recent effort in drug development concerns with the design of specific molecules that target the activity of proteins present in membranes. Approximately one third of all proteins are membrane resident, and these are the targets of about 60% of all currently approved drugs [10]. Another motivation is biomimetics and the use of membranes for constructing biotechnological applications, including drug-delivery systems [11], miniature chemical reaction vessels [12], and biosensors that combine electronic devices with membranes [13]. Biomembranes are therefore of central interest to the biochemical, life, and medical sciences.

The reasons for studying biomembranes from a purely physical point of view are that living systems, such as cell membranes, have to abide by the same laws of physics as inanimate objects. However, biological materials are extremely complex systems (usually, out of equilibrium), with non-trivial properties that are often specific rather than generic [14]. Despite this complexity the physical properties of biomembranes can be studied within a thermodynamic framework using course-grained models that span specific spatial and temporal scales [15]. Interestingly, the characteristic energies identified in biomembranes (for example, the aggregation energy per monomeric constituent) are typically an order of magnitude larger than the thermal energy (namely $k_B\,T$, where k_B is Boltzmann's constant and $T \approx 300$ K is the room temperature). As a result, biological membranes are usually found to be stable against thermal fluctuations at physiological relevant temperatures, but also sufficiently soft so that they can be readily deformed by membrane proteins or other biochemical processes [14–16], e.g. ATP hydrolysis [1,2]. Their ability to bend under very low stress is one of the main mechanical properties of membranes. This feature can be easily observed under an optical microscope, where the thin wall of cells is found to fluctuate (the so-called flicker phenomenon) [14]. Another attractive reason for a physicist to study biomembranes is because of the separation of scales, that is, the thickness of membranes is much smaller than their lateral extent. This allows us to model membranes as two-dimensional systems, reducing the dimensionality of the problem in the limit of large scales (see [15] and [16] for a detailed review). By exploring biomembranes in this way, we can attain general insights into the physical properties of cell membranes and their associated phenomena, such as scaling laws, and more importantly how these findings may couple to particular biological functions. Therefore, biological membranes provide an abundant source of inspiration to both physicists and applied mathematicians.

1.1 Historical Perspective

The current picture of biological membranes is a legacy of nearly a century of scientific research. Thus, in order to introduce the basic constituents of a membrane, as well as the orders of magnitude of the relevant physical quantities, a short history about the discovery of the membrane structure and its composition is presented in this section (see [7], [9], [14], and [17], where a number of reviews on the history of biological membranes is discussed in great detail).

Arguably, the physics and chemistry of biological membranes began with the experiments performed in the late nineteenth century by Ernest Overton, who

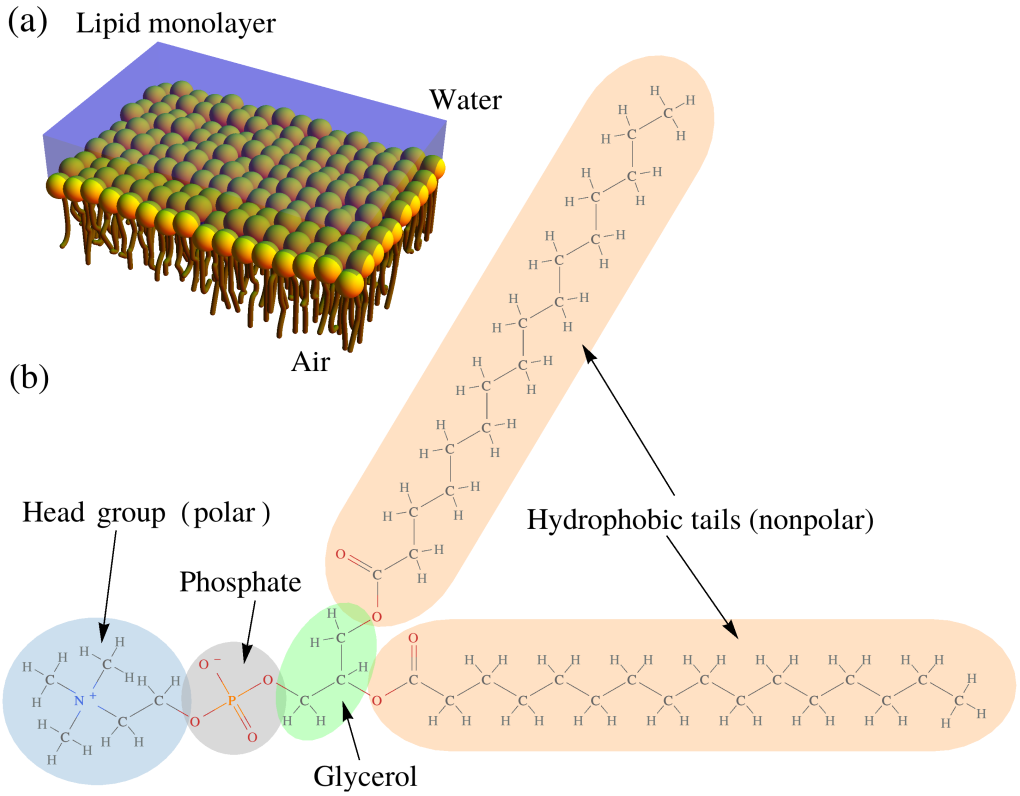

Figure 1.1: (a) Schematic diagram of lipids (amphiphilic molecules) which form a Langmuir monolayer at a water-air interface, and (b) the structural formula of a single lipid shown above as a 1,2-dipalmitoyl-sn-glycero-3-phosphocholine molecule (abbreviated DPPC) with two hydrocarbon chains linked via a glycerol moiety to a negatively charged phosphate group. Most lipids in biological membranes posses a hydrophilic head group (depicted in (a) by the yellow spheres) that is in direct contact with an aqueous solution and a nonpolar chain region (represented in (a) by the various brown strings or tails) forming the basic interior of membranes.

investigated the permeability of cell membranes for various compounds [18]. It was observed that cells are enclosed in a selectively permeable barrier, and fat-soluble molecules are more likely to penetrate it than water-solvable molecules or ions [17]. Overton's findings led to the speculation that membranes have similar properties to oils, being a lipid of some sort, which nowadays is known to be rich in cholesterol and phospholipids [2] (their composition is discussed in more details in Section 1.2).

In a seminal paper published in 1917, Irving Langmuir provided a simple technique for measuring the lateral pressure exerted by a lipid membrane as it spreads at a water-air interface [19]. Using the proposed apparatus, which is known as the Langmuir trough, he was able to show that lipids form a closely packed mono-molecular layer on the surface of water, where the area per lipid was found to be about $A_{\text{lipid}} = 0.7\ \text{nm}^2$. Langmuir also suggested the amphiphilic nature of these molecules, as shown in Figure 1.1 (a). Amphiphiles are molecules made of a polar hydrophilic head group, possessing high affinity for water, and one (or two) hydrophobic hydrocarbon tail(s), which has (have) a low affinity for water – see Figure 1.1 (b).

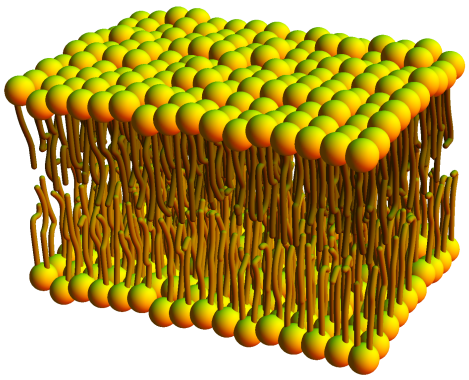

Figure 1.2: Diagram of the lipid bilayer structure according to the model proposed by Gorter and Grendel [20].

In 1925, using Langmuir's methods, E. Gorter and F. Grendel revealed that the membrane structure of erythrocytes (or red blood cells) is a lipid bilayer [20], where the hydrophobic part of the molecules is isolated from water by the layers of hydrophilic heads (see Figure 1.2). This was achieved by dissolving the lipids using acetone, then measuring the surface area of the extracted lipids in a Langmuir trough, and lastly comparing this value with the area of dried red blood cells. However, their studies included two errors: acetone does not extract all the lipids, but this error was compensated by their error in measuring the surface area of erythrocytes [7, 9]. Nonetheless, their experiment concluded that the ratio of surface area occupied by lipids to the area of the cell is approximately two, a number consistent with the theory that cells are enveloped by a lipid bilayer structure [17]. Or, in the words of the pioneering study [20]:

> "[...] all our results fit well with the supposition that the chromocytes are covered by a layer of fatty substances that is two molecules thick."

This bimolecular configuration forms the basic structure of all biomembranes, and represents the predominant structure out of the large conformational polymorphism exhibited by amphiphiles [14]. Namely, a mixture of water and amphiphilic molecules can generate a broad diversity of thermodynamically stable phases besides the lamellar phase illustrated in Figure 1.2 (see Section 1.3 for further details).

In the 1930s, H. Davson and J. F. Danielli [21] elaborated a new membrane model, where both sides of the lipid bilayer are coated by a layer of proteins, in order to explain the measured differences in the permeability (of ions or other apolar molecules) between an artificial membrane and the plasma membrane found in cells [14]. This selective permeability was hypothesised to be governed by electrostatic interactions and membrane potential. The Dawson–Danielli unit membrane model was the first commonly accepted model, dominating the membrane research in the subsequent years, and undergoing only minor changes in the 1950s due to the advent of electron microscopy [17]. The latter allowed the structure of membranes to be directly imaged, primarily through the works of J. D. Robertson [22], who discovered that the plasma membrane and all cell-organelle membranes (e.g. membrane of the cell nucleus, the Golgi apparatus, and the double layers of mitochondria) have a common construction principle, supporting the previous models introduced by Gorter and Grendel, in 1925, and Davson and Danielli, in 1935 [9]. Moreover, direct and indirect measurements of the membrane thickness (through electron micrographs and X-ray diffraction techniques, respectively) yield a value on the order of 5–8 nm, with a hydrophobic core of about 3–4 nm [14].

The next major phase in biomembrane research arrived in the late 1960s, when numerous studies [23], involving freeze-fracture electron microscopy methods, determined that proteins do not cover the bilayers, but they form globular particles, which are embedded within the membrane [7]. At the same time, with the rapid development of magnetic resonance methods (such as, nuclear magnetic resonance and electron spin resonance), many experiments showed that lipids can move laterally in the plane of the membrane [24], with a characteristic diffusion constant given by $D_{\text{lipids}} \sim 10^{-8}\ \text{cm}^2/\text{s} \approx 10^6\, A_{\text{lipid}}/\text{s}$ [14], revealing the fluid nature of biomembranes [17]. Some proteins were also found to freely diffuse in the lipid bilayer, with a diffusion constant that is much smaller than that of lipids: typically, $D_{\text{proteins}} \sim 10^{-10}\ \text{cm}^2/\text{s} = 10^{-2}\, D_{\text{lipids}}$ [14]. Furthermore, the asymmetry between the inner and outer layer of membranes was established, and the notion of transmembrane proteins was confirmed, being firstly observed on red blood cells, where the same protein was successfully labelled from both sides of the membrane [25].

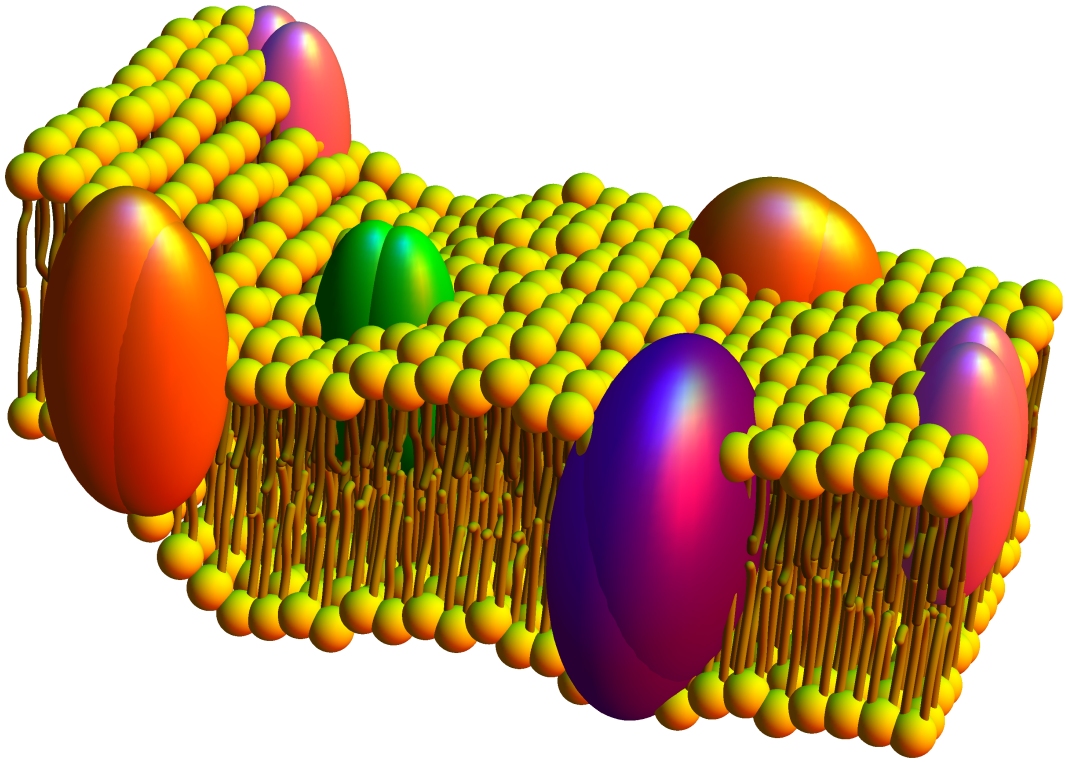

Figure 1.3: A three-dimensional representation and cross-sectional views of a biological membrane in a modern perspective of the *fluid mosaic model* originally proposed by Singer and Nicolson [26] in 1972. The lipid molecules (with the lipid species not distinguishable in this sketch) are arranged in a bilayer structure that is highly heterogeneous and dynamic. The polar heads are exposed to the aqueous environment, while the region of hydrocarbon chains forms the interior of the membrane. Its thickness near membrane proteins is commensurate with the hydrophobic belt of the corresponding protein. Also, the proteins (illustrated as the coloured ellipsoidal-like objects) can be partially or completely embedded into the lipid bilayer.

This research culminated in the *fluid mosaic model* of biomembranes (1972), also known as the Singer–Nicolson model [26], which describes a membrane as a fluid (that is, the lipidic bilayer made of various phospholipids and cholesterol) in which other macromolecules are incorporated, such as peripheral (adsorbed on the membrane surface) and integral (embedded in the bilayer) membrane proteins, as shown in Figure 1.3. The proteins act as active components and provide a variety of biological functions, including cellular transport, adhesion and signalling [1, 2]. As a loose comparison, the lipid bilayer became the arctic sea in which various icebergs (proteins) can float freely. Interestingly, the lipid-to-protein ratio varies significantly across different biological membranes; for example, the inner mitochondrial membrane is approximately 76% protein, while the myelin membrane is only 18% [7].

Although the Singer–Nicolson model is a major influential step in the study of biomembranes, integrating various experimental findings from the preceding decade on the physics and chemistry of membranes, many refinements have been amended over the past years [17, 27]. We now know that the bilayer is a highly dynamic system, where the lipids and proteins are not homogeneously distributed, but they form domains and clusters [9]. In particular, intermediate-sized domains with a diameter between 10–100 nm (and rich in sphingolipids and cholesterol) have been proposed in biomembranes – the so-called *lipid raft hypothesis* – to explain the problem of sorting and trafficking lipids and lipid-anchored proteins [28, 29]. This phenomena is discussed in much more detail in Chapter 5. Another amendment is due to the hydrophobic matching: if the hydrophobic core of the membrane is longer or shorter than the hydrophobic belt of the embedded protein, this leads to membrane thickness deformations [30]. Either the protein deforms to the match the thickness of the bilayer or the adjacent lipids stretch to compensate for this hydrophobic mismatch, or both. This effect results in non-trivial protein-lipid interactions as well as lipid-lipid interactions [31–35]. Membrane curvature is also an important key concept, which can drive lipid sorting and membrane mediated interactions [36, 37]. This is explored in more details in Chapter 3. Lastly, another interesting aspect concerns the presence of specific lipids in the vicinity of proteins in order to regulate their biological function. Arguably, this might be one of the reasons for the very large number of lipid species present in biological membranes (on the order of thousands); however, the reasons for this diversity remain an open question in cell biology [9].

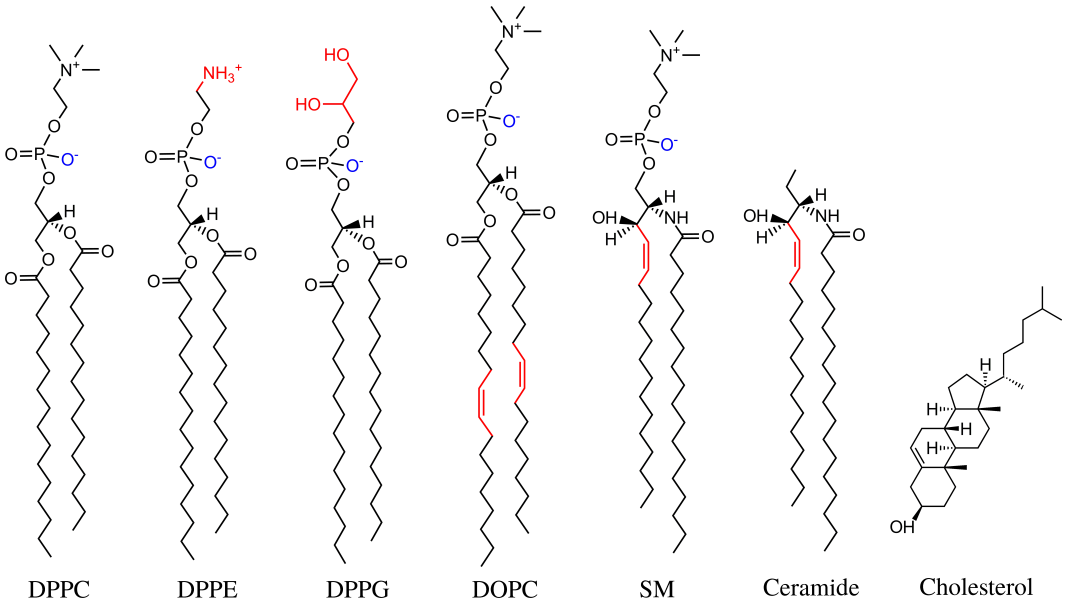

Figure 1.4: The chemical structure of some common membrane lipids. Three phospholipids with two palmitic chains are shown, where the head groups are given by phosphatidylcholine (DPPC), phosphatidylethanolamine (DPPE), phosphatidylglycerol (DPPG), as well as a phospholipid with two oleic chains and a phosphatidylcholine head group (DOPC). Some lipids without phosphate groups are also shown, such as sphingomyelin (SM), ceramide, and cholesterol.

1.2 Membrane Lipids

The macromolecules found in biological systems can be classified in four main classes: the carbohydrates, the fats, the proteins, and the nucleic acids [1]. Out of all these types, the fats (e.g. lipids) are the only one that do not form polymers, but instead they self-assemble into aggregates in an aqueous solution (e.g. water), leading to a variety of structural phases [7]. This behaviour is due to their amphiphilic nature, namely they are made up of a hydrophilic head group and a hydrophobic region [14]. Despite this simple construction principle, the compositions of both the hydrophilic groups and the hydrocarbon chains display a large variation, giving raise to a zoo of numerous types of lipid species (several thousands) [9]. To put this number into a biological perspective, the *alphabet* of possible lipid mixtures in biomembranes hugely exceed the 4-letter alphabet used to identify the nuclei acids, as well as the 20-letter alphabet of the amino acids that describe proteins [38].

Out of this plethora of lipid species, phospholipids are the most abundant type [2, 7]. Their molecular structure consist of two fatty acids that are covalently bounded to a glycerol group (esterified in its first and second position), which, in

Name	Chain length: number of double bonds	Position of unsaturations
Lauric	12:0	–
Myristic	14:0	–
Myristoleic	14:1	–
Palmitic	16:0	–
Palmitoleic	16:1	9-cis
Stearic	18:0	–
Oleic	18:1	9-cis
Linoleic	18:3	6-cis, 9-cis, 12-cis
Arachidic	20:0	–
Aracidonic	20:4	5-cis, 8-cis, 11-cis, 14-cis

Table 1.1: A selection of common saturated and unsaturated fatty acids that form the hydrocarbon chains of lipids. Adapted from [9].

turn, is linked (through the third position) to a negatively charged phosphate group that carries the terminal polar head [7]. The latter group can be composed by various organic compounds, such as choline, ethanolamine, serine, inositol, or even glycerol (see Figure 1.4 for some examples of their chemical structure) [7]. There is also an enormous range of possible fatty acids, which can vary by chain length and degree of saturation [9] (see Table 1.1 for the most common fatty acids found in nature). The typical hydrocarbon chain length is most frequently an even number between 12–20, but chains as short as 8 carbon atoms have also been found in some bacteria [39]. Furthermore, most of the hydrocarbon chains are unsaturated, where several double bonds between the carbon atoms are present along the chain. This number represents the degree of saturation, and it is typically between 1–3 (see Table 1.1). Lipid molecules that have only single bonds are known to be saturated.

As a consequence, a sophisticated (and also relatively intimidating) terminology has been developed to efficiently describe the structural form of phospholipids [7]. For example, the lipid molecule shown in Figure 1.1 (b), which has a choline head group and two palmitic chains, is named 1,2-dipalmitoyl-sn-glycero-3-phosphocholine. This is usually abbreviated as DPPC, using a common four-letter convention of the form DTPH, where DT stands for the double hydrocarbon chain groups, P for the phosphate group, and H for the polar head group. If the hydrocarbon chains are different, then the form T_1T_2PH is adopted, where T_1 and T_2 represent the corresponding hydrophobic chain-types, e.g. 1-palmitoyl-2-oleoyl-sn-

glycero-3-phosphoethanolamine is shortened as POPE.

There are many other ways of making lipids: for example, the glycerol backbone can be replaced by a sphingosine, which belongs to the family of amines [38]. The simplest version of this molecule is ceramide, as shown in Figure 1.4. Since this is a purely hydrophobic compound, a hydrophilic head can be attached in principle, which leads to variety of other lipids, e.g. sphingomyelin, if the head group is a phosphatidylcholine [38]. These lipids often occur with long saturated tails (24 carbons) and they are believed to play a role in the formation of microdomains (or rafts) in biomembranes [9]. Another important example is cholesterol, which is a member of the steriod family and it is ubiquitous in the membrane of eukaryotic cells [39]. Instead of a fatty-acid chain as its hydrophobic region, the cholesterol has a steriod ring structure, and its hydrophilic polar head is simply given by a small hydroxyl group -OH [7], see Figure 1.4. Interestingly, the cholesterol is known to influence the membrane fluidity [14], increasing the viscosity in the fluid phase (where the lipids diffuse freely and their hydrocarbon tails are disordered), while decreasing the melting temperature (we shall discuss this in more details in Section 1.4).

Not surprisingly, this chemical variability makes lipids the most diverse group of molecules found in cells. The reason for this striking feature is still an open question, although there is an increasing understanding of the collective and functional role of lipids in biomembranes [38, 39]. For a fuller account on the classification of the membrane lipids, the reader is referred to [2] and [7].

1.3 Self-assembly of Lipids

Due to the hydrophilic effect, the lipid molecules self-assemble into many possible super-molecular structures [2], see Figures 1.5–1.7 for a few examples. In other words, in a mixture of water and lipid molecules, the system tends to minimise the free-energy by shielding the hydrocarbon chains from the water, with larger assemblies more favourable at higher lipid concentrations [2, 9]. The self-assembly process also depends on the other intensive thermodynamic variables of the system, such as the temperature, the ambient pressure, or the chemical potentials of solvents [9].

Micelles occur when the solution is sufficiently dilute, such that the concentration of lipids is above some critical value that is known as the critical micelle concentration [9]. In a micelle, all the hydrophobic tails point radially towards each other, and their hydrophilic parts form a sphere-like surface, as shown in Figure 1.5 (a). Inverted micelles can also be generated where the hydrocarbon chains radiate away from the centrally assembled head groups that surround the water,

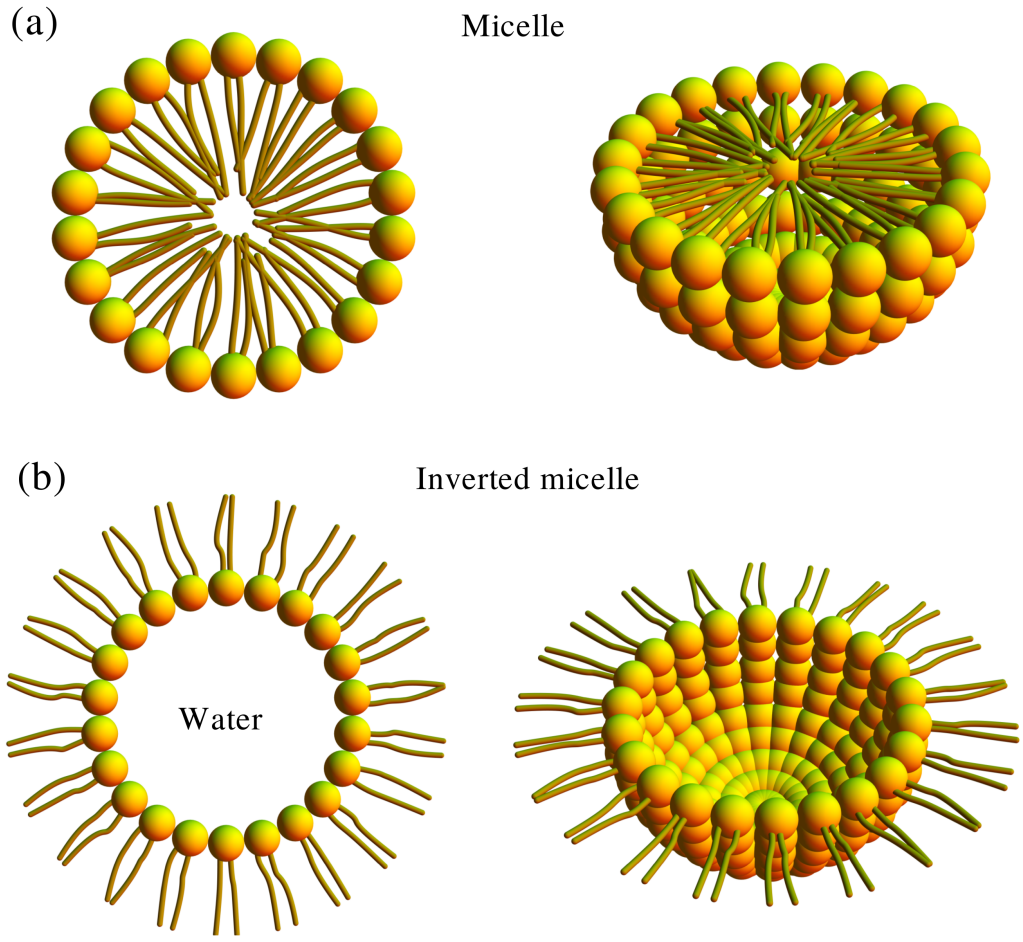

Figure 1.5: Structures of micelles formed by amphiphilic molecules. Equatorial cross-sections (on left-hand-side) and three-dimensional views (on right-hand-side) of a spherical micelle, see (a), and an inverted spherical micelle, as shown in (b).

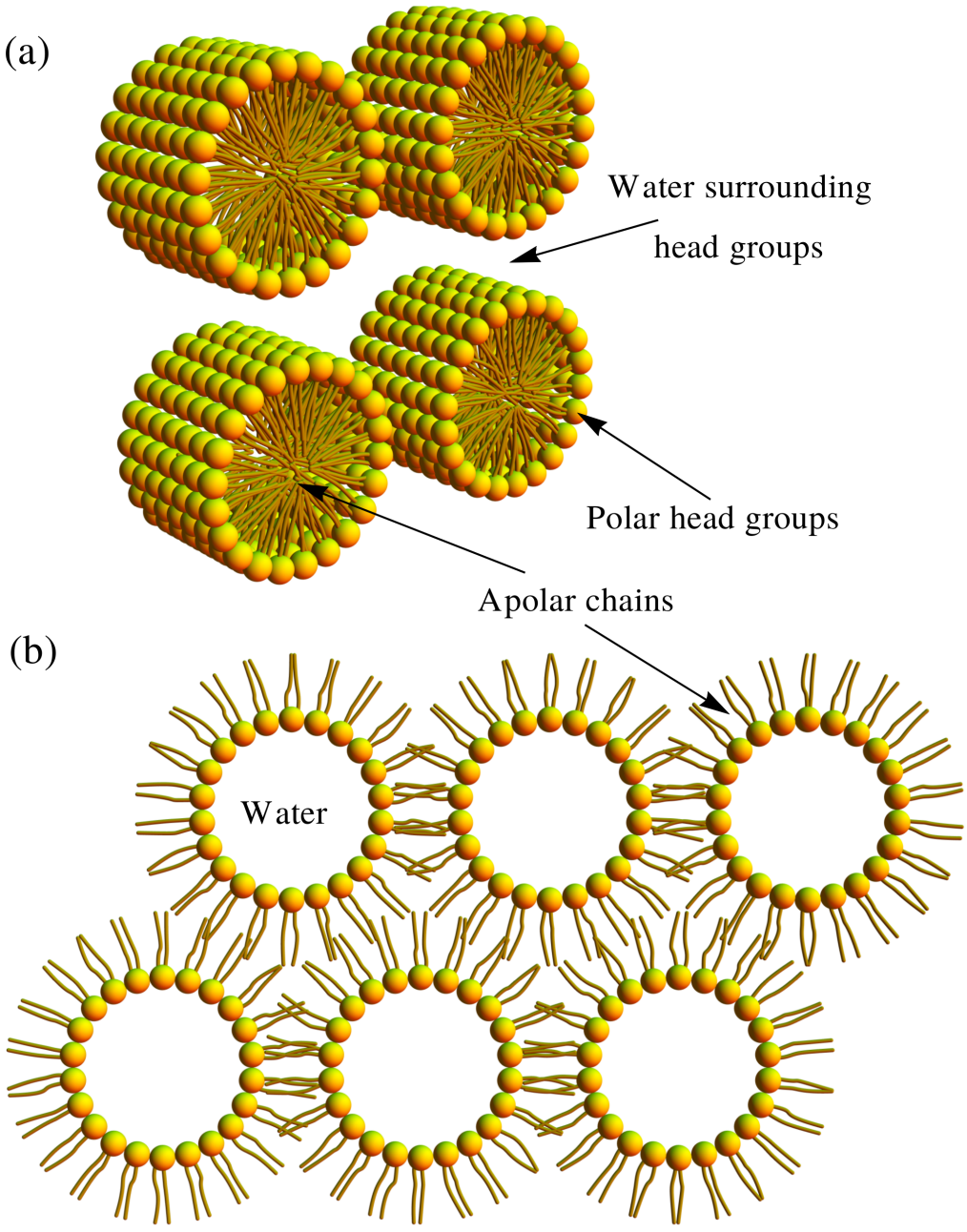

Figure 1.6: (a) Schematic picture of a lipid hexagonal phase, namely cylinders of indefinite length packed in a hexagonal arrangement. (b) Cross-sectional view of a lipid aggregate in the inverted hexagonal phase, where the water is contained within the inverted micellar cylinders, whilst the outside is filled by the hydrocarbon tails.

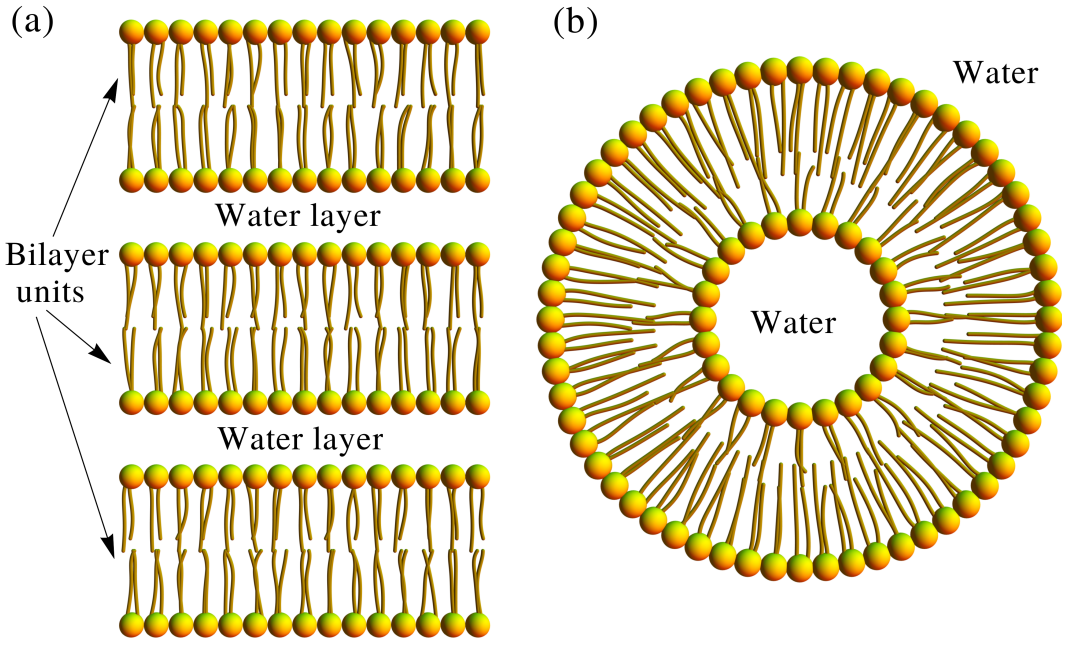

Figure 1.7: (a) Schematic illustration of lipid molecules forming a lamellar phase, namely a stack of bilayer units which are seperated by a water layer. (b) Diagram of a uni-lamellar liposome, also known as a lipid vesicle.

see Figure 1.5 (b). The formation of inverted micelles occurs at very low water concentrations, or in an oil-water mixture when the amount of water is small [2].

If the lipid concentration is increased even more, there is generally a transition from the configuration of spherical micelles to other geometries, such as cylindrical aggregates ordered in a hexagonal arrangement (known as the hexagonal phase), see Figure 1.6 (a), where the spacing between the micellar cylinders varies between 1–5 nm depending on the relative concentration [2]. An inverted hexagonal phase can exist, which is exactly the same as the hexagonal phase, but with the apolar chains radiating outwards from the cylinders that enclose the water. Typically, the diameter of these inner cylinders is about 1–2 nm [2]. However, the exterior space is completely filled by the hydrophobic chains, as shown in Figure 1.6 (b), and thus the spacing between cylinders is much smaller than in the hexagonal phase.

Moreover, a range of cubic crystal phases with a periodic three-dimensional order are possible, which can be formed, as before, in a water-continuous manner or in a hydrocarbon-chain-continuous manner [2]. The simplest cubic phase is given by a cubic arrangement of small aggregates, such as spherical micelles or inverted micelles. Other possible cubic phases are bicontinuous, where the cubic arrange-

ments are composed by a large continuous network of channels, which can be either water continuous or apolar chain continuous [2]. Another interesting phase, which is usually found in detergent systems and possibly in some lipid systems, is the sponge phase. This topologically mimics a bicontinuous cubic phase, but it does not display any periodic three- or two-dimensional structure [9].

Lastly, the simplest and also the most ubiquitous lipid phase found in nature is the lamellar phase, see Figure 1.7 (a), which includes single bilayers or multi-layered arrangements of bilayers that are stacked on top of each other, and spaced by a water layer with a thickness of about 1–10 nm [2,39]. Evidently, open ends are energetically very costly due to the exposure to water, and hence the bilayers and multi-lamellar bilayers normally close onto themselves, forming closed structures, see Figure 1.7 (b), which are typically referred as uni-lamellar and multi-lamellar liposomes (or lipid vesicles) [39], respectively. Vesicles, either uni-lamellar or multi-lamellar, are stable on a time-scale of days [15] and they can be artificially produced in the laboratory (a review of the preparation techniques can be found in [40]). These vesicles, which can be made from a few lipids and membrane proteins, are essential for the physical, life, and biochemical sciences as they represent a simplified model of a cell membrane, where specific biological functions of the membrane can be investigated on a molecular level [39].

Although we introduced the various aggregate structures as a function of the lipid concentration, this is by no means the only control parameter that determines the equilibrium phase and its stability. As previously mentioned, the self-assembly mechanism into different aggregates depends sensitively on temperature, chemical structure and other environmental conditions [9] (e.g. a temperature increase can lead to a crossover transition from a lamellar structure into an inverted hexagonal or cubic structure [39]). This leads to a high dimensional phase space with a very complex phase diagram, where different regions support a particular structure of lipid assemblies (see [2] for a complete review).

Remarkably, many of these factors can be described qualitatively within a very simple framework that involves only the effective molecular shape of a lipid molecule [38]. However, it is important to emphasise that a lipid incorporated into an aggregate does not occupy a well-defined volume, as there are no hard edges on this length scale [39]. This effective molecular shape can be related to the mean cross-sectional area a and the volume v that a lipid would occupy on average, and also how deeply it is embedded in the lipid aggregate, say ℓ. These parameters are influenced by numerous geometrical constraints, such as the size of the polar head, the length of the fatty acid chains, and their degree of saturation [39]. The latter

affects the configuration of the hydrocarbon chains, as the presence of double bonds causes kinks in the usual linear arrangement of the carbon atoms (that is, all-*trans*, see Section 1.4). Moreover, the temperature leads to rotational excitations around the C–C bonds and, as a result, increases the area occupied by the hydrocarbon tails [7]. This effect causes membrane melting transitions [9], which are discussed in more details the following section. In addition, the charge and the hydration of the head groups can also contribute to the phase preference [41] and hence to the effective shape of the lipid molecule [39].

The consequences of the effective molecular shape of a lipid has been studied by Israelachvili, Mitchell, and Ninham in a famous paper from 1976 [42], which to a physicist it is a marvellous example of the power of simple geometrical arguments. The ability of a lipid to fit into a specific aggregate is described by a packing parameter P, which is given by

$$P = \frac{v}{a\,\ell}, \tag{1.1}$$

where a, v, and ℓ are defined above. Since micelles are spherical aggregates, their total area and volume can by computed through the equations $Na = 4\pi R_{\mathrm{m}}^2$ and $Nv = 4\pi R_{\mathrm{m}}^3/3$, respectively, where R_{m} is the radius of the micelle and N is the number of lipid molecules in that spherical aggregate. Since the length ℓ of the individual lipids needs to be at least greater than the radius R_{m} for packing reasons, namely $\ell \geq R_{\mathrm{m}}$, we find that the parameter P must be smaller than $1/3$ in order to produce stable spherical aggregates. For a cylindrical aggregate of radius R_{c} and a very long length $L \gg R_{\mathrm{c}}$, we have two similar equations for their area and volume, that is, $Na = 2\pi L R_{\mathrm{c}}$ and $Nv = \pi L R_{\mathrm{c}}^2$, which yields that $P \leq 1/2$ since $\ell \geq R_{\mathrm{c}}$ must hold as before for closed packing. However, we already know that if $P \leq 1/3$ this leads to the formation of micelles. Thus, the stability condition for cylindrical aggregates is given by $1/3 \leq P \leq 1/2$. By repeating the same argument for planar or lamellar structures, the condition required for stable lipid bilayers can easily be derived, namely $1/2 \leq P \leq 1$. Moreover, as the volume v of a cylindrical-shaped lipid is exactly $a\ell$, then values of $P > 1$ suggest an effective molecular shape in form of an inverted cone, and cubic and inverted non-lamellar phases can be expected [39].

Interestingly, lipids extracted experimentally from real biological membranes, which are typically multi-component systems and appear to be in the lamellar phase, often self-aggregate into non-lamellar structures when suspended in water, regardless of whether they were removed from various different organisms or different types of cells from the same organism [38,39]. This suggests that many of the lipids present in cells are non-lamellar-forming lipids, resulting therefore in several curvature stresses within the lipid bilayer [38]. This local stress can be released by the insertion of

membrane proteins, local membrane composition, or by budding of the membrane in exocytosis and endocytosis processes [38]. The former two examples are explored in more details in Chapter 3, where the role of membrane compositional asymmetry near a trasmembrane protein is analysed within a continuum model.

1.4 Membrane Melting

Throughout the rest this thesis, we study only one of the phases mentioned above, namely membranes in the lamellar phase and formed by a single bilayer. However, the lipid order within a bilayer passes as well through different states, which depend primarily on the temperature [9]. The following lipid phases can be found in bilayers and they are listed below in terms of their occurrence at decreasing temperature:

- *Fluid phase* (L_α): This phase occurs at high temperature [2], where the lateral distribution of lipids is rather random, and all their hydrocarbon tails are rather disordered (fluid-like). This phase is believed to represent the typical bulk of biological membranes.

- *Ripple phase* ($P_{\beta'}$): The surface of the bilayer displays ripples, or wave-like structures, which can be observed in electron micrographs [7]. This phase consists of a binary mixture of lipids in L_α and $L_{\beta'}$ phases (see below) that are most often arranged in an one-dimensional periodic structure [9].

- *Gel phase* ($L_{\beta'}$): The lateral distribution of lipids shows a two-dimensional triangular lattice, and their fatty acid chains are mainly ordered in the all-*trans* configuration (see Figure 1.9) and tilted with respect to the membrane normal (hence, use of the prime symbol in its short notation) [9]. This tilt is due steric effects, that is, a mismatch between the head groups and hydrophobic tails, which does not allow the lipids to be stacked parallel to the normal [43].

- *Crystalline phase* (L_c): This occurs at much lower temperatures, and it is similar to the gel phase, expect there is no tilt angle [9]. Moreover, this is usually characterised by a three-dimensional order of a multi-lamellar configuration of lipids, where the water layer is completely absent [2].

These phases are illustrated in Figure 1.8. The crossover transition between these four phases occurs at well-defined transition temperatures, which mostly depend on the length of the chains and their degree of saturation, but also on other ambient conditions (e.g. pressure), and the addition of detergents, peptides, or cholesterol [9].

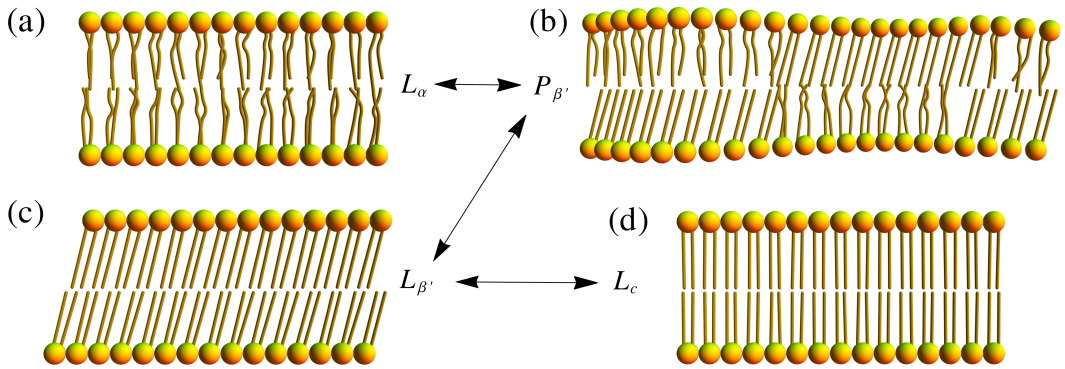

Figure 1.8: Schematic diagram of the phases within a lipid bilayer, where the temperature decreases from (a) to (d). Namely, the fluid phase (L_α), the ripple phase ($P_{\beta'}$), the gel phase ($L_{\beta'}$), and the crystalline phase (L_c), respectively. The conformational ordering of the hydrocarbon chains increases as the temperature drops.

The transitions $L_{\beta'} \leftrightarrow P_{\beta'}$ and $P_{\beta'} \leftrightarrow L_\alpha$ are known in the biomembranes literature as the pre-transition and main-transition [2], respectively. They are both fundamentally controlled by the hydrocarbon chain melting process. Namely, rotations about C–C bonds in a saturated chain result in three distinct energy minima that correspond to different conformations (or isomerisations), so-called *gauche*$^-$, *trans*, and *gauche*$^+$ [7], as illustrated in Figure 1.9. The *trans* isomer is the most stable, being the global energy minimum, and a chain configuration with all single carbon–carbon bonds in this state (i.e. all-*trans*) yields a hydrocarbon tail that is maximally extended [39]. At high temperatures every isomer is equally probable, and therefore the chain conformation becomes more disordered, disrupting the crystalline structure of the lipid bilayer. The melting temperatures (namely, the temperatures at the pre-transition and main-transition) are higher as the length of the chain is longer [9]. However, the presence of double *cis* bonds* greatly reduces the melting point [9]. As an example, the melting temperature (of the main transition) of DSPC is around 53° C, whilst DOPC has a much lower melting point, about -20° C, although the difference between the lipids is only an extra double bond in DOPC [9]. Therefore, saturated lipids melt at considerably higher temperatures (i.e. they are easier to order) than lipids with unsaturated chains which have permanent kinks. This effect is used by a variety of organisms that adjust their membranes to function at lower or higher temperatures (or even at different ambient pressures) [9].

*A *cis–trans* isomerism exists in the case of a C=C bond [7]; however, nature usually makes *cis*-bonds, and a transition between the isomers occurs only through chemical reactions [39]. Typically, the *trans*-double bonds have a significant ordering effect – they do not cause kinks as the *cis*-bonds.

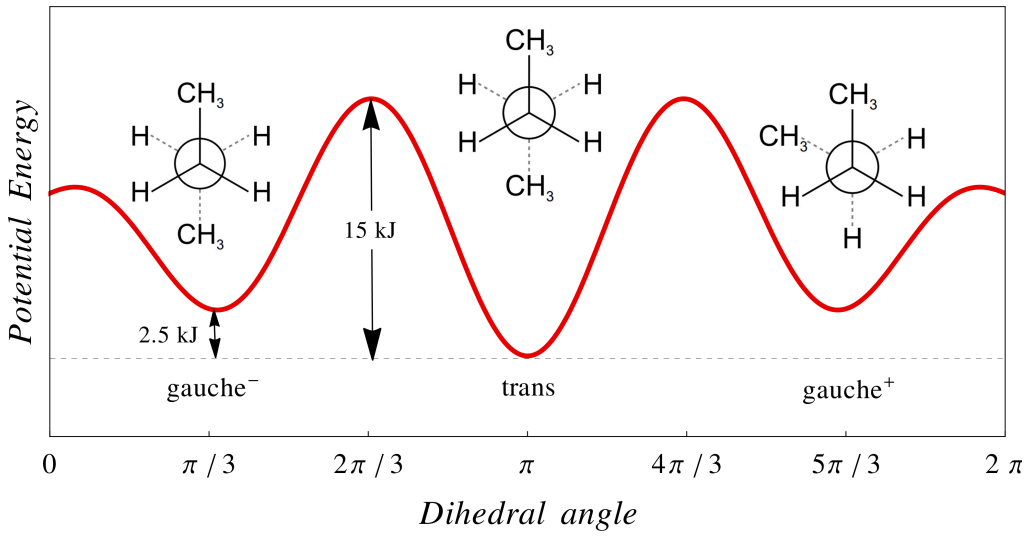

Figure 1.9: Rotations about a C–C bond in a fatty acid chain produce different conformations, the so-called *trans-gauche* isomerisations. This leads to three local minima seperated by 120°, namely *gauche*$^-$, *trans*, and *gauche*$^+$, which correspond to the orientations shown above each minimum in a Newman projection diagram. The chain configuration with all of its C–C bonds arranged in the *trans* isomer has the lowest energy state, corresponding to a zig-zag arrangement of the carbon atoms. The other two *gauche* configurations are mirror images of each other, and they have a higher potential energy than the *trans* isomer. Adapted from [7].

The addition of cholesterol in lipid bilayers has a dual effect, namely, it encourages the close packing of the hydrocarbon tails in the L_α phase, while it disturbs the chain ordering in the $L_{\beta'}$ phase [39]. Thus, in a mixture of lipid molecules and cholesterol, a *liquid-ordered* phase (L_o) and a *liquid-disordered* phase (L_d) appear when the concentration of cholesterol is found in large ($\gtrsim$ 40%) and moderate amounts [44], respectively. In the former phase, the hydrophobic tails are relatively ordered, but the membrane still preserves its fluidity. Thus, a membrane in the *liquid-ordered* phase behaves as a fluid with translational disorder and high lateral mobility, decreasing as a result the melting temperature [2]. Furthermore, the high concentration of cholesterol makes the thickness of the membrane larger and also less flexible [39]. On the other hand, the L_d phase is equivalent, in fact, with the previously introduced L_α phase, where its fatty acid chains are less ordered in comparison with the L_o phase (in terms of both translational and conformational degrees of freedom) [2, 39]. In a binary mixture of L_o and L_d phases, the minority phase normally forms domains due to phase separation [45]. The phenomena associated with this lateral phase separation in multi-component membranes has been widely studied from both theoretical and experimental perspectives [45]. This great

interest is motivated by the appealing theoretical challenges that are ingrained in this system, but also by the aspiration to gain physical insights into the nature of lipid rafts observed in membrane cells. This is discussed more in Chapter 5.

1.5 Outlook

The fundamental building blocks of all cell membranes are lipid molecules, which self-assemble to form a very thin and stable barrier where a multitude of proteins can be incorporated. In addition, they exhibit a wealth of physical phenomena including self-assembly, phase transitions, domain formation, and many other dynamical processes. For a physicist, the challenges are to understand and model these phenomena, and to generate testable predictions which can be then compared with data from biological experiments.

In this thesis, we focus on a number of problems concerning the mechanical and dynamical properties of fluid membranes, namely lipids organised in a bilayer that display a liquid-crystalline phase. On length scales larger than the membrane thickness, they can be treated as two-dimensional elastic sheets whose equilibrium shape and thermal fluctuations are only controlled by a handful of coarse-grained material parameters. The physical and mathematical aspects of this description are presented in Chapter 2, which is structured as follows: firstly, we present the essential differential geometry of two-dimensional surfaces; secondly, we show how these geometrical tools can be used to describe a fluid membrane through the so-called Canhan–Helfrich theory; and, lastly, we review some of the experimental studies carried out to estimate the phenomenological parameters in this model. Using this theory, in Chapter 3, we develop a model for the response of a fluid membrane, in terms of composition and shape, to the inclusion of a rigid transmembrane protein or a protein coat. In Chapter 4, we re-examine the methodology for inferring mechanical information about membranes from their observed fluctuations and dynamics. Particularly, we analyse, within a Gaussian approximation, the effect produced by the optical projection of surface modes across the focal depth of the microscope. In Chapter 5, we study an out of equilibrium model for the kinetics of the spontaneous membrane raft formation via membrane recycling. Finally, Chapter 6 summarises the work carried out in the thesis, highlighting any possible future refinements of the analysis, and also discusses other possible avenues of future research.

Chapter 2

From Differential Geometry to Fluid Membranes

Fluid membranes have a clear separation of scales, namely the thickness of lipid bilayers (about 5 nm thick) is typically several orders of magnitude smaller than their lateral extent (e.g. the diameter of liposomes and lipid vesicles is typically in the range of 50 nm to 100 μm). This suggests that some generic properties of fluid membranes may be adequately described by two-dimensional objects embedded into a three-dimensional space. Later we discuss what exactly this may entail, but first we summarise some of the key mathematical concepts of differential geometry that apply to two-dimensional surfaces.

2.1 Two-dimensional Surfaces

Although there is an extensive literature on differential geometry, with emphasis on both mathematics (e.g. see [46]) and applications in physics (e.g. see [47]), herein, we outline only a few of the important concepts out of this wide mathematical field, focusing primarily on the practical aspects rather than mathematical rigour.

2.1.1 Coordinate Systems and Area Elements

A two-dimensional surface, say $\mathcal{M}$, embedded in the three-dimensional space $\mathbb{R}^3$ can be uniquely determined by a three-dimensional vector $\mathbf{R} = (X, Y, Z)^{\mathsf{T}}$, where X, Y, and Z are the Cartesian coordinates, and T denotes a transpose [48]. However, these coordinates are not independent, but they satisfy a constraint condition that dictates the actual form of the surface. Thus, the choice of two coordinates determines exactly the value of the third. This means that a point on a surface in $\mathbb{R}^3$ can be

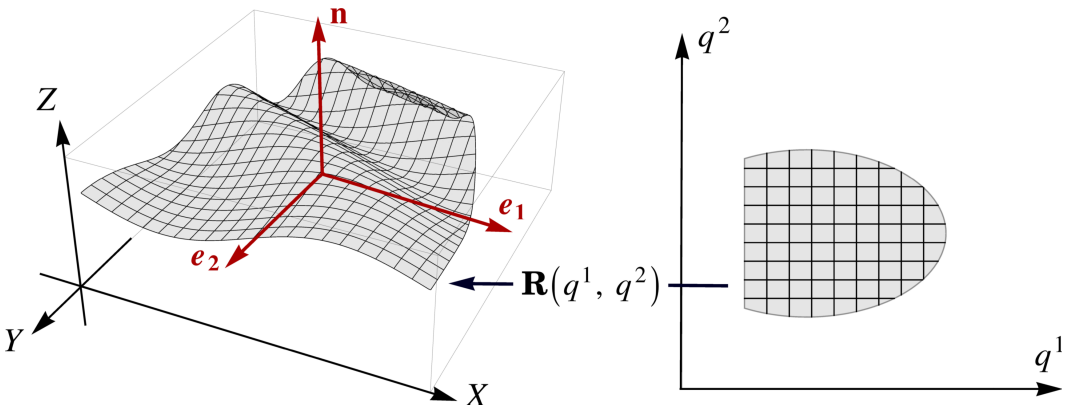

Figure 2.1: Sketch of the surface parametrisation, where a region in the q^1q^2-plane is mapped to a two-dimensional surface embedded in a three-dimensional space $\mathbb{R}^3$ through a real vector function $\mathbf{R}(q^1, q^2)$. Here, the vectors $\mathbf{e}_1$ and $\mathbf{e}_2$ depict the tangent vectors along the constant lines of q^1 and q^2, respectively, whereas $\mathbf{n}$ is the normal vector that is perpendicular to both $\mathbf{e}_1$ and $\mathbf{e}_2$.

represented by a pair of two real variables, say (q^1, q^2). In other words, q^1 and q^2 parametrise, in some arbitrary way, all the points on the surface, namely

$$\mathcal{M} = \left\{ \mathbf{R}(q^1, q^2) = \Big(X(q^1, q^2),\, Y(q^1, q^2),\, Z(q^1, q^2) \Big)^{\mathsf{T}} \,\Big|\, (q^1, q^2) \in \mathbb{B} \subset \mathbb{R}^2 \right\}, \quad (2.1)$$

where $\mathbb{B}$ is a bounded subset of the q^1q^2-plane. By (2.1), to any point (q^1, q^2) of $\mathbb{B}$ there is associated a point of $\mathbb{R}^3$ with position vector $\mathbf{R}(q^1, q^2)$ [48], as illustrated in Figure 2.1. Although the choice of the parametric representation is completely arbitrary, in practice, we choose the parametrisation that is best adapted to the particular problem at hand. Furthermore, in order to apply differential calculus to geometric problems, the existence of certain partial derivatives of $\mathbf{R}(q^1, q^2)$ with respect to coordinates q^1 and q^2 are therefore assumed [48].

Hence, given a choice of parametrisation, we can form a coordinate system at every point on the surface by constructing the tangent vectors and their associated normal vector (see Figure 2.1), which are usually defined by

$$\mathbf{e}_\mu := \frac{\partial \mathbf{R}}{\partial q^\mu} = \partial_\mu \mathbf{R}, \quad \text{with } \mu \in \{1, 2\}, \quad \text{and } \mathbf{n} := \frac{\mathbf{e}_1 \times \mathbf{e}_2}{\|\mathbf{e}_1 \times \mathbf{e}_2\|}, \quad (2.2)$$

respectively. Provided that vectors $\mathbf{e}_1$ and $\mathbf{e}_2$ are linearly independent everywhere, the mapping $(q^1, q^2) \mapsto \mathbf{R}(q^1, q^2)$ defines a smooth surface embedded in $\mathbb{R}^3$ [48].

The tangent vectors $\mathbf{e}_\mu$ also allows us to compute the infinitesimal area element at every point on the surface. The area $\mathrm{d}S$ of a small patch of $\mathcal{M}$ is simply

the area of a parallelogram spanned by the vectors $\mathbf{e}_1\,\mathrm{d}q^1$ and $\mathbf{e}_2\,\mathrm{d}q^2$, which can be written in terms of the magnitude of their cross product [47], namely

$$\mathrm{d}S = \|\mathbf{e}_1 \times \mathbf{e}_2\|\,\mathrm{d}q^1\mathrm{d}q^2 = \sqrt{\|\mathbf{e}_1\|^2\,\|\mathbf{e}_2\|^2 - (\mathbf{e}_1 \cdot \mathbf{e}_2)^2}\;\mathrm{d}q^1\mathrm{d}q^2, \tag{2.3}$$

where a vector calculus identity is used in the last step. The total area $\mathcal{A}$ of the surface $\mathcal{M}$ is simply the double integral of (2.3), which is required to be invariant under our choice of coordinates (q^1, q^2). This can be shown by rewriting (2.3) in terms of the *metric tensor* (or the first fundamental form) [16], which is defined by

$$g_{\mu\nu} := \mathbf{e}_\mu \cdot \mathbf{e}_\nu, \tag{2.4}$$

and it can also be represented by the following 2×2 symmetric matrix:

$$\mathbf{G}\left(q^1, q^2\right) = \begin{pmatrix} \dfrac{\partial \mathbf{R}}{\partial q^1} \cdot \dfrac{\partial \mathbf{R}}{\partial q^1} & \dfrac{\partial \mathbf{R}}{\partial q^1} \cdot \dfrac{\partial \mathbf{R}}{\partial q^2} \\ \dfrac{\partial \mathbf{R}}{\partial q^2} \cdot \dfrac{\partial \mathbf{R}}{\partial q^1} & \dfrac{\partial \mathbf{R}}{\partial q^2} \cdot \dfrac{\partial \mathbf{R}}{\partial q^2} \end{pmatrix}. \tag{2.5}$$

Since the expression under the square root of equation (2.3) is exactly the determinant of the matrix $\mathbf{G}\left(q^1, q^2\right)$, we have that

$$\mathcal{A} = \iint_{\mathcal{M}} \sqrt{\det \mathbf{G}\left(q^1, q^2\right)}\;\mathrm{d}q^1\mathrm{d}q^2. \tag{2.6}$$

Under a change of coordinates from (q^1, q^2) to (p^1, p^2), the new tangent vectors are given by

$$\tilde{\mathbf{e}}_\alpha = \frac{\partial \mathbf{R}}{\partial p^\alpha} = \frac{\partial q^\mu}{\partial p^\alpha}\,\mathbf{e}_\mu, \tag{2.7}$$

where we apply the chain rule and implicitly sum over the repeated index μ (that is, we employ the Einstein index convention) [48]. Furthermore, under this change of parametrisation, the new metric tensor is found to be

$$\tilde{g}_{\alpha\beta} := \tilde{\mathbf{e}}_\alpha \cdot \tilde{\mathbf{e}}_\beta = \frac{\partial q^\mu}{\partial p^\alpha}\,\frac{\partial q^\nu}{\partial p^\beta}\,g_{\mu\nu}, \tag{2.8}$$

where (2.4) and (2.7) are used to obtain the expression in the final step. If we define the transformation matrix $\mathcal{J}$ (the so-called Jacobian matrix) by $\mathcal{J}_{\alpha\mu} = \partial q^\mu / \partial p^\alpha$, then the metric tensor in (2.8) can be written in a matrix form as follows:

$$\tilde{\mathbf{G}}\left(p^1, p^2\right) = \mathcal{J}^\mathsf{T}\,\mathbf{G}\left(q^1, q^2\right)\mathcal{J}, \tag{2.9}$$

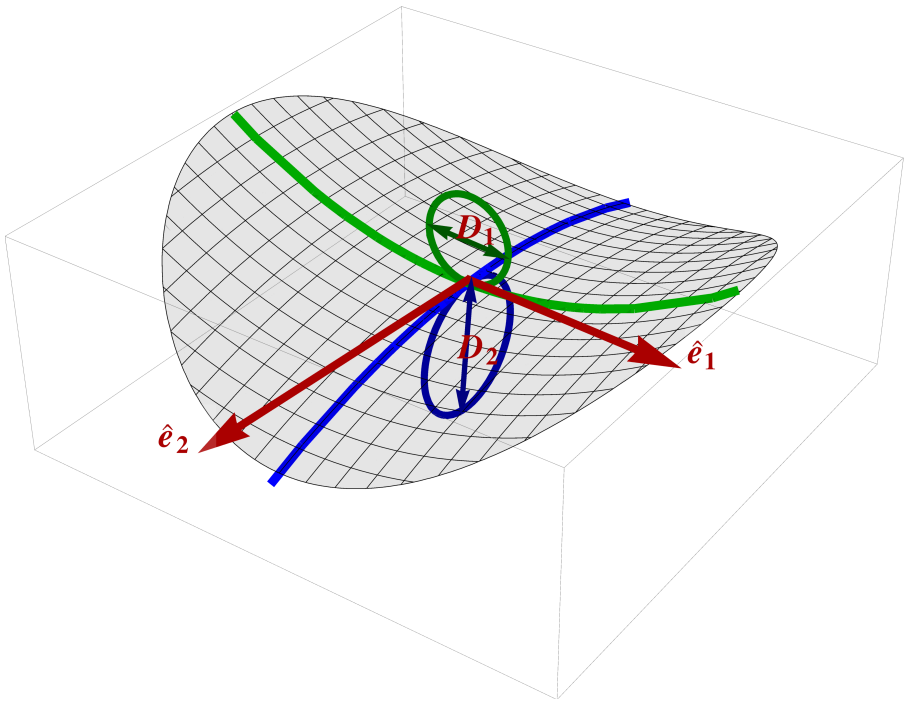

Figure 2.2: Illustration of a saddle surface embedded in $\mathbb{R}^3$. The thick blue and green lines indicate the principal directions of a point on the surface, where $\hat{\mathbf{e}}_1$ and $\hat{\mathbf{e}}_2$ are the corresponding tangent vectors that are orthogonal to each other. The two circles illustrate the principal curvatures (herein, denoted by k_1 and k_2) associated to each principal direction, where the diameters $D_1 = 2k_1^{-1}$ and $D_2 = 2k_2^{-1}$.

where $\mathcal{J}^\mathsf{T}$ denotes the matrix transpose of $\mathcal{J}$. Therefore, by employing some basic properties of determinants, we can show that $\det\left(\mathcal{J}^\mathsf{T}\mathbf{G}\,\mathcal{J}\right) = (\det\mathcal{J})^2\,(\det\mathbf{G})$. By using this result and the fact that $\mathcal{J}$ is the Jacobian of the transformation [49], that is, $\mathrm{d}q^1\mathrm{d}q^2 = |\det\mathcal{J}|\,\mathrm{d}p^1\mathrm{d}p^2$, we find that the total area $\mathcal{A}$ remains unchanged under coordinate transformations:

$$\mathcal{A} = \iint_{\mathcal{M}} \sqrt{\det\mathbf{G}\left(q^1,q^2\right)}\;\mathrm{d}q^1\mathrm{d}q^2 = \iint_{\mathcal{M}} \sqrt{\det\tilde{\mathbf{G}}\left(p^1,p^2\right)}\;\mathrm{d}p^1\mathrm{d}p^2. \tag{2.10}$$

2.1.2 Mean and Gaussian Curvatures

Intuitively, the notion of curvature of a surface embedded in a three-dimensional space quantifies how much its normal vector changes as we move along that surface, or, colloquially, how *curved* is the neighbourhood of a point on the surface as we step towards a chosen direction. Since there are many ways to move on a surface, this object must involve derivatives of the surface normal along every tangent direction. Using the specific parametrisation introduced previously in (2.2), this can

be constructed by taking directional derivatives of $\mathbf{n}$ along each $\mathbf{e}_\mu$ which are then projected onto each tangent vector $\mathbf{e}_\nu$. This forms a tensor that is known as the second fundamental form, or the *extrinsic curvature tensor*, and it is defined by

$$c_{\mu\nu} := \mathbf{e}_\mu \cdot (\mathbf{e}_\nu \cdot \nabla)\, \mathbf{n}, \tag{2.11}$$

which, as analogous to the metric tensor, can also be represented as a matrix:

$$\mathbf{C}\left(q^1, q^2\right) = \begin{pmatrix} \mathbf{e}_1 \cdot (\mathbf{e}_1 \cdot \nabla)\, \mathbf{n} & \mathbf{e}_2 \cdot (\mathbf{e}_1 \cdot \nabla)\, \mathbf{n} \\ \mathbf{e}_1 \cdot (\mathbf{e}_2 \cdot \nabla)\, \mathbf{n} & \mathbf{e}_2 \cdot (\mathbf{e}_2 \cdot \nabla)\, \mathbf{n} \end{pmatrix}. \tag{2.12}$$

where ∇ is the gradient operator. However, since the normal vector $\mathbf{n}$ is a function of the surface parameters q^μ, then $\partial_\nu \mathbf{n} = (\mathbf{e}_\nu \cdot \nabla)\, \mathbf{n}$ using the chain rule. Moreover, by differentiating the identity $\mathbf{e}_\mu \cdot \mathbf{n} = 0$ with respect to the coordinate q^ν, we find that $\partial_\nu \mathbf{e}_\mu \cdot \mathbf{n} + \mathbf{e}_\mu \cdot \partial_\nu \mathbf{n} = 0$, which in turn allows us to rewrite (2.11) as

$$c_{\mu\nu} = -\mathbf{n} \cdot \partial_\nu \mathbf{e}_\mu, \tag{2.13}$$

showing that $c_{\mu\nu}$ is a symmetric tensor since $\partial_\nu \mathbf{e}_\mu = \partial_\mu \mathbf{e}_\nu$. The usual convention of differential geometry is to define (2.11) with the opposite minus sign, in contrast to the majority of membrane related literature. However, this sign ambiguity is simply a convention of whether we decide to call a curvature away from the surface normal as negative or positive. Hereinafter, we choose the latter so that the curvature of a sphere with outward pointing normal has a positive value.

As alluded previously, there is nothing special with our selection of tangent directions and clearly the precise form of (2.11) depends on the particular choice of coordinates (q^1, q^2). However, using a similarity transformation [49], it is possible to diagonalise the matrix (2.12), that is, $\mathbf{D}\left(q^1, q^2\right) = \Lambda^{-1}\, \mathbf{C}\left(q^1, q^2\right) \Lambda$, in order to obtain the extremal curvatures and their corresponding directions. In this diagonal basis, the non-zero elements of $\mathbf{D}$ (i.e. eigenvalues) are known as the *principal curvatures*, say k_1 and k_2, and their associated eigenvectors are the *principal directions*, which we denote here by $\hat{\mathbf{e}}_1$ and $\hat{\mathbf{e}}_2$. Thus, k_1 and k_2 are purely determined by a derivative of the surface normal along the directions $\hat{\mathbf{e}}_1$ and $\hat{\mathbf{e}}_2$, respectively, without any contribution along the other orthonormal directions (see Figure 2.2).

Once, the principal curvatures and their associated directions are found, then the curvature*, k_n, in every other direction, say along $\mathbf{t} = \hat{\mathbf{e}}_1 \cos\varphi + \hat{\mathbf{e}}_2 \sin\varphi$, can

*In fact, this is the *normal curvature* of an embedded curve on the surface, which is solely due to *shape* of that surface. Another curvature can be constructed, known as the *geodesic curvature*, which is exclusively due to the conformation of the curve alone. More details can be found in [48].

be determined through a simple formula which was originally derived by Euler [48], namely

$$k_n = k_1 \cos^2 \varphi + k_2 \sin^2 \varphi, \tag{2.14}$$

where φ is the angle between the principal direction $\hat{\mathbf{e}}_1$ and the chosen direction $\mathbf{t}$.

Although, by construction, the principal curvatures are independent of our choice of parametrisation, in practice, they are not the most advantageous mathematical quantities to work with. Instead, the arithmetic mean and the product of k_1 and k_2 are typically used, which are known as the mean curvature, H, and the Gaussian curvature, K, respectively. Interestingly, as the matrix $\mathbf{D}$ is diagonal, we find that $\det \mathbf{D} = k_1 k_2$ and $\operatorname{Tr} \mathbf{D} = k_1 + k_2$. On the other hand, since the trace and determinant of a matrix are similarity invariant [49], that is, $\det \mathbf{C} = \det \mathbf{D}$ and $\operatorname{Tr} \mathbf{C} = \operatorname{Tr} \mathbf{D}^{\dagger}$, then we can easily extract the curvatures H and K from the extrinsic curvature tensor in any given parametrisation [47], namely

$$H\left(q^1, q^2\right) = \frac{1}{2} \operatorname{Tr} \mathbf{C}\left(q^1, q^2\right) \quad \text{and} \quad K\left(q^1, q^2\right) = \det \mathbf{C}\left(q^1, q^2\right). \tag{2.15}$$

As a consequence, the mean and Gaussian curvature are surface intrinsic properties, encapsulating all the information required to quantify the curvature of a surface [47].

Another alternative formula for the mean curvature H, which also shows its coordinate invariance, can be found in terms of the gradient of the surface normal. By using the definition (2.11), the principal curvatures k_μ can be re-expressed in the tangent basis $\hat{\mathbf{e}}_\mu$, namely $k_1 = \hat{\mathbf{e}}_1 \cdot \partial_1 \mathbf{n}$ and $k_2 = \hat{\mathbf{e}}_2 \cdot \partial_2 \mathbf{n}$. For the mean curvature, this yields

$$H = \frac{1}{2}\left(\hat{\mathbf{e}}_1 \cdot \partial_1 \mathbf{n} + \hat{\mathbf{e}}_2 \cdot \partial_2 \mathbf{n}\right) = \frac{1}{2} \nabla \cdot \mathbf{n}, \tag{2.16}$$

where the last result is found by employing the orthogonality of the basis $(\hat{\mathbf{e}}_1, \hat{\mathbf{e}}_2, \mathbf{n})$.

2.1.3 Monge Parametrisation

The coordinate invariance of the total area, the mean and Gaussian curvature is an extremely valuable property, as it gives us the freedom to describe a surface in the parametrisation that is the best suited to the problem at hand. There are many possible avenues that one can take in order to describe a surface embedded in $\mathbb{R}^3$, for example, by exploiting the symmetries of the problem. The most simple choice of coordinates is the so-called *Monge parametrisation*, where a surface is determined by its height from a flat reference plane, as illustrated in Figure 2.3. In other words,

[†] This can be proven by employing the product identity $\det(\mathbf{AB}) = \det \mathbf{A} \det \mathbf{B}$, and the cyclic property of the trace, namely $\operatorname{Tr}(\mathbf{ABC}) = \operatorname{Tr}(\mathbf{BCA}) = \operatorname{Tr}(\mathbf{CAB})$, for any matrix $\mathbf{A}$, $\mathbf{B}$, and $\mathbf{C}$.

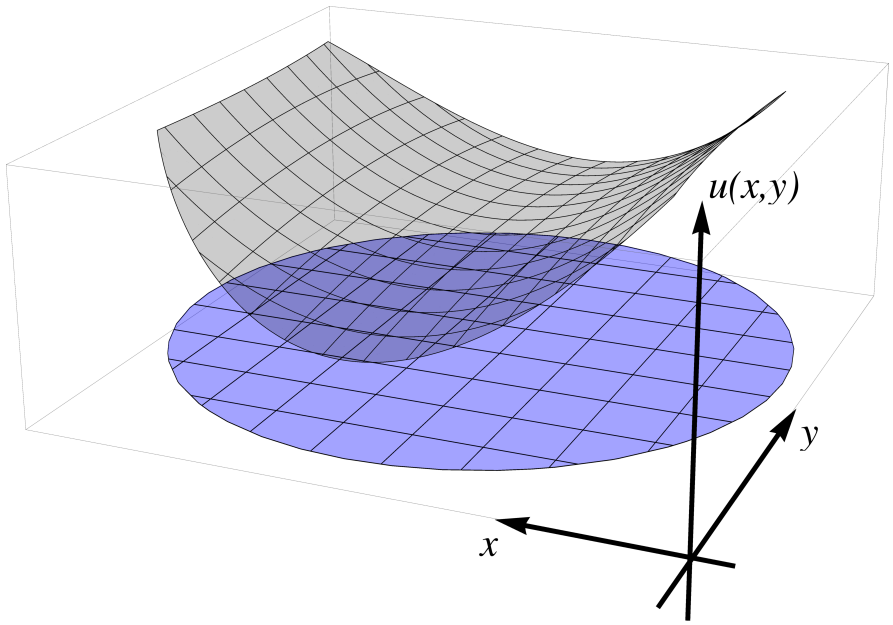

Figure 2.3: The Monge parametrisation of a two-dimensional surface (coloured here as grey), namely, a surface described by a height function $u(x, y)$ above the xy-plane. The blue region depicts the projection of this surface onto the xy-plane. Note that it would not be possible to capture features such as folding with a single-valued function $u(x, y)$.

the position vector $\mathbf{R}$ is given by

$$\mathbf{R}\,(x,\,y) = \Big(x,\,y,\,u\,(x,y)\Big)^{\mathsf{T}}, \tag{2.17}$$

where $u(x, y)$ is a height function, with x and y being the parametric variables which form the reference plane. A corollary shortcoming of this description consists in the requirement that, for each x and y, there exists only a single height, and therefore this parametrisation is unable to describe *overhangs*. Nonetheless, it is very useful in describing surfaces that weakly deviate from the reference plane, that is, a nearly flat surface with the magnitude of the gradient being small (see below).

Using the equations (2.2) and (2.17), the local tangent vectors, $\mathbf{e}_x$ and $\mathbf{e}_y$, and their associated normal unit vector $\mathbf{n}$ are given by

$$\mathbf{e}_x = \begin{pmatrix} 1 \\ 0 \\ u_x \end{pmatrix}, \quad \mathbf{e}_y = \begin{pmatrix} 0 \\ 1 \\ u_y \end{pmatrix}, \text{ and } \quad \mathbf{n} = \frac{1}{\sqrt{1 + \left(\nabla_{\parallel}\, u\right)^2}} \begin{pmatrix} -u_x \\ -u_y \\ 1 \end{pmatrix}, \tag{2.18}$$

respectively, where $\nabla_{\parallel} = (\partial_x,\, \partial_y)^{\mathsf{T}}$ is the two-dimensional gradient operator, and the

subscript notation for partial derivatives is used, namely $u_x = \partial_x u$ and $u_y = \partial_y u$.

Thus, the metric tensor, or the first fundamental form, written in a matrix form is found to be

$$\mathbf{G}\,(x,y) = \begin{pmatrix} 1+u_x^2 & u_x\,u_y \\ u_x\,u_y & 1+u_y^2 \end{pmatrix}, \tag{2.19}$$

and its corresponding determinant is given by $g := \det \mathbf{G} = 1 + \big(\nabla_{\!\parallel}\, u\big)^2$. As a result, the infinitesimal area element in the Monge representation is $\mathrm{d}S = \sqrt{g}\;\mathrm{d}x\mathrm{d}y$.

Using the form of basis vectors (2.18), the extrinsic curvature tensor can be written in the matrix form as follows:

$$\mathbf{C}\,(x,y) = \frac{1}{\sqrt{g}} \begin{pmatrix} u_{xx}\left(1+u_y^2\right) - u_{xy}u_x u_y & u_{xy}\left(1+u_x^2\right) - u_{xx}u_x u_y \\ u_{xy}\left(1+u_y^2\right) - u_{yy}u_x u_y & u_{yy}\left(1+u_x^2\right) - u_{xy}u_x u_y \end{pmatrix}, \tag{2.20}$$

where $u_{xx} = \partial_{xx}u$, $u_{yy} = \partial_{yy}u$, and $u_{xy} = \partial_{xy}u$. Consequently, this allows us to find the expressions for the mean and Gaussian curvature through (2.15), namely

$$H = -\frac{1}{2}\,\nabla_{\!\parallel} \cdot \left(\frac{\nabla_{\!\parallel}\, u}{\sqrt{1+\big(\nabla_{\!\parallel}\, u\big)^2}} \right), \quad \text{and} \quad K = \frac{1}{g^2}\left(u_{xx}u_{yy} - u_{xy}^2\right), \tag{2.21}$$

respectively. An interesting case occurs when the surface gradients u_x and u_y are assumed to be small, that is, the absolute magnitude $|\nabla_{\!\parallel}\, u| \ll 1$. In this limiting case, the mean and Gaussian curvature simplify to

$$H = -\frac{1}{2}\left(u_{xx} + u_{yy}\right) \;+\; \mathcal{O}\Big(|\nabla_{\!\parallel}\, u|^2\Big) = -\frac{1}{2}\,\nabla_{\!\parallel}^2\, u \;+\; \mathcal{O}\Big(|\nabla_{\!\parallel}\, u|^2\Big), \tag{2.22}$$

and

$$K = u_{xx}u_{yy} - u_{xy}^2 \;+\; \mathcal{O}\Big(|\nabla_{\!\parallel}\, u|^2\Big) \tag{2.23}$$

where $\nabla_{\!\parallel}^2 := \nabla_{\!\parallel} \cdot \nabla_{\!\parallel}$ is the two-dimensional version the Laplacian operator. Also, the area element $\mathrm{d}S$ reduces to

$$\mathrm{d}S = \left[1 + \frac{1}{2}\left(\nabla_{\!\parallel}\, u\right)^2\right] \mathrm{d}x\mathrm{d}y \;+\; \mathcal{O}\Big(|\nabla_{\!\parallel}\, u|^3\Big). \tag{2.24}$$

This approximation is employed in Chapter 3 to study the weak deformations in the shape and composition of membrane due to the trans-membrane inclusion of a rigid object (e.g. integral proteins, or protein coats).

2.2 Canham–Helfrinch Theory

In this section, we apply the geometric concepts presented previously to describe the energetics of a fluid membrane at large scales. We introduce the modern quantitative description of biological and biomimetic membranes, which began in the 1970s with the pioneering studies of Canham [50], Helfrich [51], and Evans [52].

2.2.1 Free-energy Functional

As described in Chapter 1, biomembranes are large aggregates of lipid molecules with many degrees of freedom, and there are various ways to physically characterise their local behaviour within the bilayer. However, due to the separation of scales, the description of membranes on scales larger than its thickness is, to a great extent, insensitive to their detailed microscopic physics and chemistry (even though their actual existence and stability on macroscopic scales is a result of the latter). As a result, we can usually construct a large-scale theory of membranes through an effective energy functional that depends solely on the macroscopic observables [16]. This gives rise to a number of phenomenological constants which cannot be predicted *a priori* at that scale. Namely, they are considered as fixed material parameters, and their values can be estimated only through experiments (see Section 2.3) or molecular dynamics simulations [16].

In order to construct such a continuum theory for fluid membranes, we need to firstly identify the relevant local parameters that couple to the macroscopic observables. The fast lateral diffusion of lipids in the fluid phase (see Chapter 1) guarantees that a membrane cannot support long-lived in-plane shear stresses or deformations [14]. Moreover, this positional fluidity implies that the memory time of any previous conformational changes is extremely short, and as a result the effective energy functional depends only on its current two-dimensional geometry [16]. Thus, the related free-energy is a purely geometrical quantity, which can be build as an expansion in its surface invariants, such as the area $\int \mathrm{d}S$, the mean curvature H, the Gaussian curvature K, and other higher order derivatives that define an independent surface scalar [53]. This free-energy expansion is usually truncated to second order [16], that is,

$$\mathcal{F} = \int \mathrm{d}S \, \Big[\mathcal{C}_0 + \mathcal{C}_1 \, H + \mathcal{C}_2 \, H^2 + \mathcal{C}_3 \, K \Big], \tag{2.25}$$

which is primarily motivated by the smallness of the membrane curvature in comparison to its inverse thickness. The phenomenological constants $\mathcal{C}_0$, $\mathcal{C}_1$, $\mathcal{C}_2$, and $\mathcal{C}_3$

are commonly written as

$$\mathcal{C}_0 = \sigma + 2\kappa H_0^2, \quad \mathcal{C}_1 = -2\kappa H_0, \quad \mathcal{C}_2 = 2\kappa, \quad \text{and} \quad \mathcal{C}_3 = \bar{\kappa}, \tag{2.26}$$

which allows us to recast the free-energy (2.25) in its standard form that is usually found in the membrane literature [14, 15], namely

$$\mathcal{F} = \int \mathrm{d}S \left[\sigma + 2\kappa \left(H - H_0 \right)^2 + \bar{\kappa} K \right], \tag{2.27}$$

where σ is the surface tension, H_0 is the spontaneous curvature, and the curvature parameters κ and $\bar{\kappa}$ are the bending and Gaussian moduli, respectively. The physical meaning of these phenomenological constants is discussed in the next section. This free-energy functional represents the key ingredient of the Canham–Helfrinch theory, describing a fluid membrane as a two-dimensional surface embedded in $\mathbb{R}^3$.

A few other examples of microscopic parameters that may also contribute to the large-scale theory of fluid membranes include the tilt angle of lipids, and whether the membrane is a simply a monolayer or a bilayer [16]. The latter leads to a global conserved quantity given by the area difference between the two monolayers, provided that the exchange of lipids between the two leaflets occurs very slowly. This area difference of monolayers can be included in (2.27) through a Lagrange multiplier, yielding important physical implications that have been extensively investigated [54–57]. However, on larger scales than the membrane thickness, the exact form of (2.27) remains unchanged regardedless of whether the membrane is seen as a bilayer or a monolayer, with the corresponding parameters (2.26) being only renormalised (as described in Section 2.2.3). On the other hand, the local tilt of lipids can be included as a vector-field that lives on the curved surface, coupling therefore to the geometry of the membrane [58–61]. Since these two aspects are secondary to our work, they are not discussed hereinafter and the reader is referred to [14, 15] for a fuller account.

2.2.2 Phenomenological Parameters

The first parameter in the free-energy (2.27) is the surface tension σ, which reflects the energy cost of creating an interface. The area energy associated with this constant, $\mathcal{F}_{\mathcal{A}} = \sigma \int \mathrm{d}S$, can be interpreted in two ways: either σ is regarded as a Lagrange multiplier conjugate to the total area, or it is viewed as an independent thermodynamic variable that is linear in the membrane area [14, 16]. Moreover, in the latter case, if we assume that the membrane is incompressible (that is, the

area-per-lipid is fixed), then the total area of the membrane is proportional to the total number of lipids. Thus, the surface tension can also be considered (in a grand canonical ensemble) as an analogue of the chemical potential of the external lipid reservoir [14]. As a consequence, in this scenario, if we pull in N times the lipid area from some reservoir of lipids, we need to pay N times the energetic cost [16]. It is worth noting that this energetic contribution is somewhat different to the deformation energy due to stretching the membrane, where the area-per-lipid is actually varied. Finally, it is also important to mention that the surface tension σ does not represent a material parameter of the bilayer, since it usually depends on the mechanical constraints to which the membrane is exposed, e.g. an osmotic pressure difference in case of a lipid vesicle [16].

The second term in (2.27) is the curvature energy that measures the local elastic response of the mean curvature H from the spontaneous curvature H_0[‡]. Since the latter arises from the linear order terms in the expansion (2.25), then a non-zero value of H_0 corresponds to a membrane with a broken up-down symmetry, reflecting therefore the possibility of a physical asymmetry between the two lipid layers of the membrane. For example, one of the leaflets can be enriched by a certain lipid, or the aqueous environment is different on the two sides of the membrane [16, 36]. Conversely, for membranes where both leaflets cannot be distinguished, we require that $H_0 = 0$. This is due to the up-down symmetry, which means that the energy must be invariant under a sign change of the normal unit vector $\mathbf{n}$, implying that linear terms in H are not permissible – see equation (2.16).

If we assume that the membrane is up-down symmetric, then the two curvature moduli κ and $\bar{\kappa}$ (which are known as the bending rigidity, or bending modulus, and Gaussian curvature modulus, respectively) couple only to two independent quadratic surface scalars H^2 and K, respectively. Although H^2 is always positive, the Gaussian curvature K has no definitive sign. However, the energy-per-unit-area due to curvature alone needs to be positive at quadratic order[§], namely

$$2\kappa H^2 + \bar{\kappa} K = \frac{1}{2} \begin{pmatrix} k_1 \\ k_2 \end{pmatrix}^{\mathsf{T}} \begin{pmatrix} \kappa & \kappa + \bar{\kappa} \\ \kappa + \bar{\kappa} & \kappa \end{pmatrix} \begin{pmatrix} k_1 \\ k_2 \end{pmatrix} \geq 0, \tag{2.28}$$

where k_1 and k_2 are the principal curvatures. In order to satisfy the above inequality, the eigenvalues of the matrix in (2.28) are required to be non-negative, which leads

[‡] H_0 is usually known as the mean spontaneous curvature. Note that a spontaneous Gaussian curvature is also possible, but this term comes in only at quartic order in the expansion [16].

[§] This condition can be violated but the system is then unstable to lowest order.

to the following condition between the curvature moduli:

$$0 \leq (-\bar{\kappa}) \leq 2\kappa, \tag{2.29}$$

showing that the bending modulus κ is always positive, whilst the Gaussian curvature modulus $\bar{\kappa}$ is negative but larger than -2κ [16]. Despite that κ and $|\bar{\kappa}|$ are usually comparable in magnitude [62–65], the associated energy to the the Gaussian term contributes to the overall energy only through changes in the topology of the membrane and the geodesic curvature of its boundaries [14]. This result is commonly known as the *Gauss–Bonnet theorem* [48], and it implies that no smooth deformations can lead to a change in the energy $\bar{\kappa} \int \mathrm{d}S\ K$. As a result, the shape of membranes and the mechanical stresses carried through them are usually insensitive to $\bar{\kappa}$, which makes it extremely difficult to estimate its value in both experiments and simulations [16]. Nevertheless, there are many biological processes where the Gaussian modulus may play an important role, such as the membrane fusion and fission which are ubiquitous in the biomembranes of cells [2].

Thus, for many applications the Gaussian modulus can be neglected and we adopt that approximation in what follows. If the bending rigidity κ is also negligibly small, then the membrane is described by the surface tension term $\mathcal{F}_{\mathcal{A}}$ alone (soup films are a common example of such a system). On the other hand, without the surface tension σ, the membrane is purely characterized by the bending term, namely $\mathcal{F}_H = 2\kappa \int \mathrm{d}S\ H^2$ (ignoring the spontaneous curvature). However, if both energetic contributions are relatively important, then the problem becomes slightly more interesting, where the pure-tension and pure-bending limits are typically recovered at length scales larger and smaller, respectively, than a typical crossover length λ, which on dimensional grounds is found to be

$$\lambda = \sqrt{\frac{\kappa}{\sigma}}. \tag{2.30}$$

In other words, on length scales larger than λ the energy associated with the bending deformation mode becomes negligible in comparison to the tension term, whereas on length scales smaller than λ the bending contribution dominates throughout.

Interestingly, the typical value of the surface tension for biomembranes is about $\sigma \sim 10^{-5}$ N/m [66], and $\kappa \sim 10\ k_B T$ [67], which yields $\lambda \sim 70$ nm. This suggests that the bending terms are significant on the length scales at which the cellular processes such as budding, endocytosis, or exocytosis, occur (i.e. on the order of 50 nm [2]), but on larger scales than λ (say, the size of the cell, a few μm) the biomembrane physics is mainly dominated by the surface tension.

2.2.3 Bilayer-monolayer Renormalisation

By treating each monolayer as an individual structure, we can apply the same reasoning, as in Section 2.2.1, in order to construct an effective free-energy functional of a lipid monolayer, namely

$$\mathcal{F}_{\mathrm{m}} = \int \mathrm{d}S_{\mathrm{m}} \Big[\sigma_{\mathrm{m}} + 2\,\kappa_{\mathrm{m}} \left(H_{\mathrm{m}} - H_{\mathrm{m},0}\right)^2 + \bar{\kappa}_{\mathrm{m}}\, K_{\mathrm{m}} \Big], \tag{2.31}$$

which is identical to equation (2.27) apart from the superscript that indicates that each quantity corresponds now to a single monolayer rather than a bilayer. Notice that the monolayer spontaneous curvature $H_{\mathrm{m},0}$ is closely related to the effective molecular shape of a lipid (that is, its packing parameter P discussed in Section 1.3), which in monolayer assemblies results in an intrinsic tendency to relax into a state of finite curvature if the shape of the lipid constituents are non-cylindrical ($P \neq 1$). As a consequence, the parameter $H_{\mathrm{m},0}$ is usually referred to as the lipid curvature, with the sign convention as positive if the lipid has a larger hydrophilic head group compared to the shape of its hydrophobic tails, that is, $P < 1$ [16].

In order to find the relationship between the monolayer free-energy (2.31) and its bilayer counterpart (2.27), we need to firstly understand how a membrane slab of finite thickness is idealised to a mathematical surface. In the case of a bilayer, the common choice is to adopt the mid-plane between the two leaflets as the two-dimensional surface, say $\mathcal{M}$. However, in the case of a monolayer, there is no obvious choice on symmetry grounds, and the usual method (in the elastic theory) is to consider a surface where neither stretching nor compression occurs upon bending, which is known as the pivotal plane [16], and it is denoted here by $\mathcal{M}_{\mathrm{m}}$. Hence, if we assume a constant distance z_0 between the mid-plane of the bilayer and the pivotal plane of one of its monolayers, then we have that

$$\mathcal{M}_{\mathrm{m}}(q^1, q^2) = \mathcal{M}(q^1, q^2) + z_0\, \mathbf{n}(q^1, q^2) \tag{2.32}$$

where $\mathbf{n}$ is the normal unit vector of the surface $\mathcal{M}$ (as well as $\mathcal{M}_{\mathrm{m}}$ as the surfaces are assumed to be parallel), and the variables q^1 and q^2 parametrise these two surfaces. The exact relationships between their area elements, mean, and Gaussian curvatures are given by following expressions [46]:

$$\mathrm{d}S_{\mathrm{m}} = \left(1 + 2\,z_0 H + z_0^2 K\right) \mathrm{d}S, \tag{2.33}$$

$$H_{\mathrm{m}} = \frac{H + z_0 K}{1 + 2\,z_0 H + z_0^2 K}, \quad \text{and} \quad K_{\mathrm{m}} = \frac{K}{1 + 2\,z_0 H + z_0^2 K}, \tag{2.34}$$

respectively. Therefore, using the above identities, we can re-write $\mathcal{F}_{\mathrm{m}}$ in terms of the geometric scalars of the bilayer, which to first order in z_0 yields

$$\mathcal{F}_{\mathrm{m}} = \int \mathrm{d}S \Big\{ \left(\sigma_{\mathrm{m}} + 2\kappa_{\mathrm{m}} H_{\mathrm{m},0}^2\right) + 2H \left[\left(\sigma_{\mathrm{m}} + 2\kappa_{\mathrm{m}} H_{\mathrm{m},0}^2\right) z_0 - 2\kappa_{\mathrm{m}} H_{\mathrm{m},0}\right] + 2\kappa_{\mathrm{m}} H^2 + K\left(\bar{\kappa}_{\mathrm{m}} - 4\, z_0\, \kappa_{\mathrm{m}} H_{\mathrm{m},0}\right) \Big\} \; + \; \mathcal{O}\big(z_0^2\big). \tag{2.35}$$

Since a bilayer consists of two monolayers, then the total effective free-energy is given by $\mathcal{F}_{\mathrm{b}} = \mathcal{F}_{\mathrm{m}} + \mathcal{F}_{\mathrm{m}'}$, where $\mathcal{F}_{\mathrm{m}'}$ is the energy contribution due to the other monolayer with the pivotal surface $\mathcal{M}_{\mathrm{m}'}(q^1, q^2) = \mathcal{M}(q^1, q^2) - z_0\, \mathbf{n}(q^1, q^2)$. Thus, if we assume that both monolayers are identical, then by comparing the resulting terms in $\mathcal{F}_{\mathrm{b}}$ with the coefficients of (2.27), we have that $H_0 = 0$, as expected, and

$$\sigma = 2\left(\sigma_{\mathrm{m}} + 2\kappa_{\mathrm{m}} H_{\mathrm{m},0}^2\right), \quad \kappa = 2\kappa_{\mathrm{m}}, \quad \text{and} \quad \bar{\kappa} = 2\left(\bar{\kappa}_{\mathrm{m}} - 4\, z_0\, \kappa_{\mathrm{m}} H_{\mathrm{m},0}\right). \tag{2.36}$$

This shows that the large-scale theory of either monolayers or bilayers reduces to the same physics, with the phenomenological coefficients of the membrane being renormalised. Namely, the bending rigidity of the bilayer is twice the monolayer bending modulus (or, in general, it is the sum of the bending rigidities of each monolayer). On the other hand, the membrane surface tension is twice the monolayer surface tension, as anticipated, but with an additional term that reflects the internal stress generated by the non-zero intrinsic curvatures of each lipid monolayer [16] (this term is usually known as the *spontaneous tension* [68, 69]). Finally, the Gaussian curvature modulus acquires, as well, a small correction due to the monolayer spontaneous curvature, which interestingly it can increase or decrease its value depending on the sign of the lipid curvature $H_{\mathrm{m},0}$.

2.3 Model Membrane Systems and Experiments

As detailed in Section 2.2.2, the membrane surface tension σ is not a material dependent parameter, the spontaneous curvature H_0 vanishes, in general, for symmetry arguments, and the Gaussian curvature modulus $\bar{\kappa}$ is mostly limited to topological effects [14]. As a result, the bending rigidity κ is essentially the most fundamental phenomenological constant in the Canham–Helfrinch theory, controlling and characterising the shape and the mechanical properties of fluid membranes on large scales. The bending modulus is an intrinsic property of the membrane, which primarily depends on its lipid composition, such as the degree of saturation and the length of the fatty acid chains [70–72]. For fluid membranes, its estimated value ranges from

about 10 k_BT (or 4×10^{-20} J) to rather less than 100 k_BT (or 4×10^{-19} J), with k_BT the thermal energy at room temperature [70]. In this section, we briefly review some of the different techniques which have been used to experimentally verify the Canham–Helfrinch theory and to estimate the value of the bending modulus.

2.3.1 Spherical and Planar Geometries as Model Systems

To investigate the mechanics of biological membranes and to study the theoretical model presented in Section 2.2, various minimal model systems of lipid membranes have been developed, which can accommodate both a single lipid species or a mixture of many types of lipids (see [70] for a detailed review). In addition, these model systems can also be used to mimic a plethora of different biological processes that involve lipid membranes [73]. In particular, the effect of proteins on membranes can be examined by reconstituting a number of transmembrane proteins [74], or by binding proteins to membranes through their receptors [75]. Typically, these model systems can be classified in terms of the geometries employed in the experimental methods, predominantly consisting of spherical and planar lipid assemblies [70].

Lipid membranes of spherical geometry, such as lipid vesicles or liposomes, as shown in Figure 1.7 (b), are widely used in experiments [70]. Their size usually ranges a from about 50 nm (e.g. small unilamellar vesicles, or SUVs) to a few 10 μm (e.g. giant unilamellar vesicles, or GUVs). Because of the relatively large sizes of the GUVs, they can be studied under an optical microscope, being a suitable system to observe membrane deformations. The GUVs represent the simplest model of a cell membrane, and they are extensively used to analyse the mechanical properties of membranes, the demixing phenomena of lipid mixtures, and the interaction with membrane proteins or peptides [70, 73, 76]. This is one of the most common methods to estimate the bending rigidity of membranes, and the different experimental techniques of extracting κ is discussed in the next section.

However, for a large number of other experimental methods (such as X-ray or neutron techniques), the spherical vesicles are not the most appropriate model systems, and membranes of planar geometries are used instead. They generally consist of a single bilayer supported on a solid substrate, which may incorporate, as before, many types of lipids and a multitude of different reconstituted proteins [77–79]. However, the mechanical and chemical properties of membranes are dramatically affected by the rather short distance between the solid substrate and the bilayer, which is typically around 2 nm [70]. As a consequence, the bilayer is usually anchored to the substrate through polymer chains or it is rested on a polymer cushion [80–82]. Another way to resolve this technical issue is to consider a stack of various bilayers,

as illustrated in Figure 1.7 (a), which are arranged parallel to the substrate [83–85].

These planar systems are widely used in X-ray or neutron experiments to investigate the membrane structure and the lipid organisation within the membrane (which goes beyond the spatial resolution provided by optical microscopy), and moreover to measure their fluctuation spectrum [86–88]. The latter allows us to obtain mechanical information about membranes, particularly yielding an estimate of the bending modulus [88–90]. For more details, the reader is referred to [70] and [88].

2.3.2 Techniques to Estimate the Bending Modulus

The model systems discussed in Section 2.3.1 have been widely used to measure the membrane elastic constants in the framework of the Canham–Helfrich theory [70]. In particular, the bending rigidity has been estimated through numerous techniques, which are mainly based on the membrane response to thermal fluctuations or applied external stresses. Although a comprehensive list of its measured values for different lipid compositions can be found in [67,72,87], hereinafter, we discuss only the experimental methods that are in realm of optical microscopy: by measuring the shape fluctuations, micropipette aspiration techniques, by pulling membrane nanotubes, and by weakly deforming the shape of GUVs through external fields [70].

Flickering spectroscopy

Since fluid membranes are exceptionally soft materials, with a small value of the bending modulus, on the order of few k_BT, the membrane shape exhibits fluctuations, or undulations, induced by the thermal agitation [14]. It is important to note that the effective free-energy of the Canham–Helfrinch theory already includes, in a way, various thermal fluctuations in the internal degrees of freedom of the bilayer. However, they are coarse-grained out on large scales, and therefore the phenomenological parameters (2.26) are functions of the ambient temperature. Consequently, the shape undulations mentioned above are, in fact, fluctuations of the membrane geometry, and not of its underlying microscopic components [14]. This compelling notion was firstly explored, in 1975, by F. Brochard and J. F. Lennon, in order to explain the flickering phenomenon observed in red blood cells [91]. The mean squared amplitude of these undulation modes was later computed in a planar geometry [92], yielding the following simple expression for the *fluctuation spectrum* or the static structure factor of a membrane:

$$\left\langle |u_{\mathbf{q}}|^2 \right\rangle = \frac{k_B T}{\mathcal{A}\,(\sigma\, q^2 + \kappa\, q^4)}, \tag{2.37}$$

where $\mathcal{A}$ is the area of a membrane patch, $u(\mathbf{r})$ is the local deviation of this membrane from its average position along the normal direction, with $u_{\mathbf{q}}$ as its Fourier transform. Here, q is the magnitude of the Fourier wave vector $\mathbf{q}$ associated to $\mathbf{r} = (x, y)^{\mathsf{T}}$, that is, the position vector in the mean-plane of the membrane. This shows that a simple analysis of the mode structure of the membrane thermal fluctuations can be used to measure the bending rigidity κ, but also its surface tension σ.

The method is usually referred to as *flicker spectroscopy*, and its been widely used in video-microscopy experiments to estimate κ of red blood cells [93, 94] and GUVs of various lipid compositions [95–107]. The common theoretical framework includes, as well, the dynamical effects due to the camera integration time [103] and other dissipative processes [108], but also the specific geometry used in the experiments, which usually involves a quasi-spherical approximation of GUVs [97]. The measured values of the bending rigidity determined by this method tend to be significantly and systematically larger than those obtained through X-ray scattering and micromechanical manipulation techniques [67] (which are presented next).

This methodology is discussed in more details in Chapter 4, where we investigate the effect due to the projection of quasi-spherical modes onto the focal plane of the microscope on the estimates of the elastic constants. The primary motivation of this work is the unresolved *puzzle* in the literature where the flicker experiments give κ too high compare to the other methods. By taking into account this correction due to the projection of thermal fluctuations, we find that the estimated values of κ by means of flicker spectroscopy are now in good agreement with the other methods.

Micropipette aspiration technique

This method was originally used by E. Evans to measure the mechanical properties of red blood cells and GUVs [109–111]. By partially aspirating (or sucking) a vesicle into a small pipette with a diameter of about 10 μm or smaller, the pressure difference Δp between the interior of the vesicle and its surrounding medium can controlled experimentally. If we assume a Young-Laplace relation across both spherical caps found inside and outside of the micropipette, with a radius R_{in} and R_{out}, respectively, then the membrane tension σ is given by

$$\Delta p = 2\sigma \left(\frac{1}{R_{\text{in}}} - \frac{1}{R_{\text{out}}} \right), \tag{2.38}$$

and, therefore, it can be obtained through simple geometric measurements [16]. Moreover, the difference between the actual membrane area (i.e. given by the total number of lipids in the vesicle) and the observed area of the membrane outside the

micropipette is known as the *excess area*, and it is usually denoted by α [111]. By assuming that volume enclosed by the vesicle remains constant, the excess area α can be determined by measuring the projected length of the vesicle that is partially aspirated into the micropipette [111]. The variation of the excess area as the membrane surface tension is changed from σ_0 to σ is found to be [70, 111]:

$$\Delta\alpha = \frac{k_B T}{8\pi\kappa} \ln\left(\frac{\sigma}{\sigma_0}\right). \tag{2.39}$$

At low membrane tensions, the excess area α arises mainly from the shape undulations of the vesicle, and a crossover transition is therefore observed between an enthalpic regime, where the membrane is only stretched elastically, and an entropic regime, which is primarily dominated by thermal fluctuations in the shape [70]. By restricting to membrane surface tensions below this crossover transition (lower than 10^{-5} N/m), then (2.39) provides a viable method to extract the bending modulus κ and to study other mechanical properties of lipid membranes [71, 111–114].

Membrane pulling

Another method that allows us to deduce the bending rigidity involves the direct measurement of a point-force that is required to extract a long thin tether (namely, a membrane nanotube) out of the membranes of GUVs [70]. There is a large number of experimental techniques that can be used to achieve the membrane tube-pulling, for example, through hydrodynamic flows [115], electroporation [116], or using an optically trapped bead [117–121]. The extraction of a cylindrical membrane tube leads to an energy cost that is given by

$$\mathcal{F}_{\text{tube}} = \int \mathrm{d}S \, \left(\sigma + 2\kappa H^2\right) - fL \, = \, 2\pi RL \left(\sigma + \frac{\kappa}{2R^2}\right) - fL \tag{2.40}$$

where f is the applied point-force, L is the displacement of that point, which corresponds to the length of the membrane tube, and R represents its radius [122, 123]. Interestingly, the equation (2.40) exhibits an energetic competition between two effects: the bending energy term favours a larger tube radius, whilst the surface tension term tends to reduce it, preferring smaller tubes. Thus, the equilibrium radius R_0 for a given applied force f_0 can be determined by minimising (2.40), namely

$$R_0 = \sqrt{\frac{\kappa}{2\sigma}} \quad \text{and} \quad f_0 = 2\pi\sqrt{2\kappa\sigma}, \tag{2.41}$$

respectively. Since f_0 only depends on the elastic constants of the membrane, this reveals that a measurement of the applied force necessary for pulling a tether from a membrane can be used to estimate κ [115–121], provided that surface tension is known, e.g. through a micropipette aspiration technique [111].

External fields

Lastly, the mechanical response of a lipid vesicle to an external field (either an electric or a magnetic field) have been used to measure the bending modulus for different lipid compositions [70]. By exposing a lipid vesicle to an alternative electric field, the induced transmembrane potential yields an effective electric tension, which in turn deforms its spherical shape into an ellipsoid. The total lateral tension can be computed from the Maxwell stress tensor and the eccentricity of this ellipsoid, see [124] for more details. By measuring the apparent variation of membrane area as a function of the lateral tension, which is due to a flattening of thermal fluctuations, it allows us, through a relation similar to equation (2.39), to compute the bending rigidity of the membrane [124–128]. An analogous procedure can be performed by using a magnetic field instead if the GUVs are filled with a ferrofluid [129].

2.4 Summary

Fluid membranes are incredibly soft materials characterised a very small value of the bending rigidity. One of the most remarkable aspects of fluid membranes is the separation of scales due to the large aspect ratio between the thickness of the bilayer and its lateral dimension. Thus, a fluid membrane can be regarded on large scales as an incompressible elastic sheet, controlled primarily by the bending rigidity but also by its surface tension. The appropriate language to mathematically describe these objects is the beautiful subject of differential geometry and statistical mechanics, which forms the basis of the Canham-Helfrich theory. This was proposed independently by Canham, Helfrich and Evans in the early 1970s.

Since their pioneering works, a tremendous effort has been devoted to study both theoretically and experimentally [16, 45, 70] many of the problems ingrained in this model. Through various model systems, many *in vitro* membrane processes can be experimentally studied to a great extent, and numerous theoretical predictions can be tested against the experimental data. The success of this theory to prescribe a theoretical foundation of biomembranes and their associated properties highlights its physical and biological importance, representing a marvellous example where physics can shed light on the understanding of biological systems.

Chapter 3

Compositional Variation near Membrane Inclusions

Biological membranes possess a considerably complicated architecture, including a large number of heterogeneities in their composition, such as a myriad of different membrane proteins which can be either absorbed on the surface or embedded in the membrane [26,27]. These proteins act as active constituents and contribute to a variety of biological functions, including cellular transport, signal transduction and cell adhesion [1]. Moreover, various experimental studies have shown that the interaction with the neighbouring lipid molecules can regulate the function of many membrane proteins [130–133]. Although this regulation may depend on specific chemical interactions, a large number of transmembrane proteins are modulated by non-specific lipid-protein interactions that arise solely from the coupling of their hydrophobic regions (namely, between the hydrophobic core of the membrane and the hydrophobic belt of the protein) [134–137]. This indicates that, in many circumstances, the dominant effects are purely mechanical and caused by protein-induced perturbations of the surrounding lipid structure, which incur an energetic cost [138–140]. In this chapter, the mechanical deformations of the lipid environment in the vicinity of a rigid membrane inclusion is analysed by modelling the membrane as a continuous elastic medium, based on the Canham-Helfrich theory introduced in Chapter 2.

3.1 Introduction

The basic structure of biomembranes comprises of a large number of discrete lipid molecules, which move laterally in the plane of the membrane, with a diffusion constant, $D_{\text{lipids}} \sim 10^{-8}$ cm^2/s, that is larger by nearly two orders of magnitude than

the diffusion of transmembrane proteins, namely $D_{\text{proteins}} \sim 10^{-10}$ cm^2/s [141–143]. As a consequence, during the time that a membrane protein diffuses an average distance of one lipid diameter, many lipid molecules will interchange places near the protein, coarse-graining out the lipidic discreteness of the membrane. Moreover, the typical transition time for conformational changes of the protein (about 5 μs) is much slower than the characteristic diffusion time of the lipids. This gives us a strong indication that a lipid bilayer can be effectively approximated as a continuous medium in the vicinity of a membrane protein (see Section 2.2.2). In addition, the transmembrane proteins can be regarded as rigid inclusions and embedded into the bilayer, such that their hydrophobic and hydrophilic parts match with those of the adjacent lipids. This fitting usually disturbs the equilibrium configuration of the protein-free membrane and changes the free energy of the lipid bilayer [139].

As a result, the mechanical deformations of the lipid environment in the vicinity of a transmembrane protein can be quantitatively described by local field variables, such as the height and/or the thickness of the bilayer [31–35, 144–154]. These examples of structural variables correspond to the two main classes of deformations induced by transmembrane proteins, namely the mid-plane bending and the hydrophobic mismatch, respectively [139,148]. The free-energy cost associated with these deformation modes are completely decoupled on symmetry grounds and they can be independently analysed provided that the perturbations are small [146–148]. Furthermore, the deformation fields of neighbouring proteins can overlap and induce membrane-mediated interactions between the proteins, which may be either attractive or repulsive depending on their shape and orientation [31–35, 144–154]. The characteristic length scale of the mid-plane bending interactions is generally longer than the length scale of the deformations in the membrane thickness, but the interaction strength of the former deformation mode is typically much weaker than the latter [147,148]. Consequently, many theoretical studies have been devoted to understand how membrane-mediated interactions may affect the spatial organization of proteins, and their ability to respond and communicate conformational changes to each other [34, 151–157].

Here, we consider an additional deformation mode that results from the enrichment of curvature sensitive inclusions in the vicinity of a membrane protein, such as non-lamellar-forming lipids or any kind of molecules smaller than the typical size of a protein. The addition of these molecular particles is usually characterized by a spontaneous curvature. This is a thermodynamic property of lipid monolayers that is operationally defined as their preferred mean curvature in the absence of external mechanical stresses [36, 42]. As discussed in Section 2.2.3, two opposed

monolayers that have the same lipid curvature will always form a planar bilayer, even though the monolayers may have a non-zero intrinsic curvature [138, 140]. Hence, in the context of bilayers, it is more appropriate to consider a composite spontaneous curvature given by the difference between the monolayer spontaneous curvature of each leaflet [51]. This suggests that asymmetrically doped bilayers generate a non-zero mean curvature by bending the membrane away from one of the aqueous surroundings. As a result, the spontaneous curvature can be used to quantitatively describe the asymmetry in the distribution of molecular inclusions between the two lipid layers of the membrane [138, 140].

Irrespective of its microscopic origin, the spontaneous curvature is normally treated as a well-defined global property, where a uniform distribution is assumed across the different leaflets of the bilayer. However, this assumption is not generally valid and consequently a local description is needed to account for non-homogeneous regions of membranes. This is particularly the case for the environment around transmembrane proteins, where the membrane-induced deformation fields provide the possibility of selection and enrichment of certain lipids, or surfactants, near the protein faces. As an illustrative example, cone-shaped molecules (such as lysophospholipids) can laterally and transversely diffuse within the bilayer, and localise to energetically favourable regions near proteins, where the membrane has complementary curvature [36, 158]. Because of their curvature preference, this leads to a local compositional asymmetry in the vicinity of the membrane protein, which subsequently generates a local spontaneous curvature, as shown in Figure 3.1. The main purpose of this study is to investigate such situations within a continuum theory of membranes, where the transmembrane proteins are treated as rigid inclusions.

In the next section, an analytic methodology is described which can be used for estimating the membrane energy, their shape, and the local phase behaviour, near a transmembrane protein. Subsequently, in Section 3.3, we apply this model to a number of biologically relevant problems. In particular, in Section 3.3.1, we examine the regime in which the membrane can become unstable and how this may be used to estimate the unknown parameters in our framework. In Section 3.3.2, the methodology is applied to a simple model of transmembrane proteins which display an asymmetrical shape. Lastly, in the final sections, we show how this model can be used to extend the gating-by-tilt mechanism for mechanosensitive channels of large conductance [159], and, furthermore, we investigate the effect due to the membrane compositional asymmetry on the early stages of protein coat assembly [160].

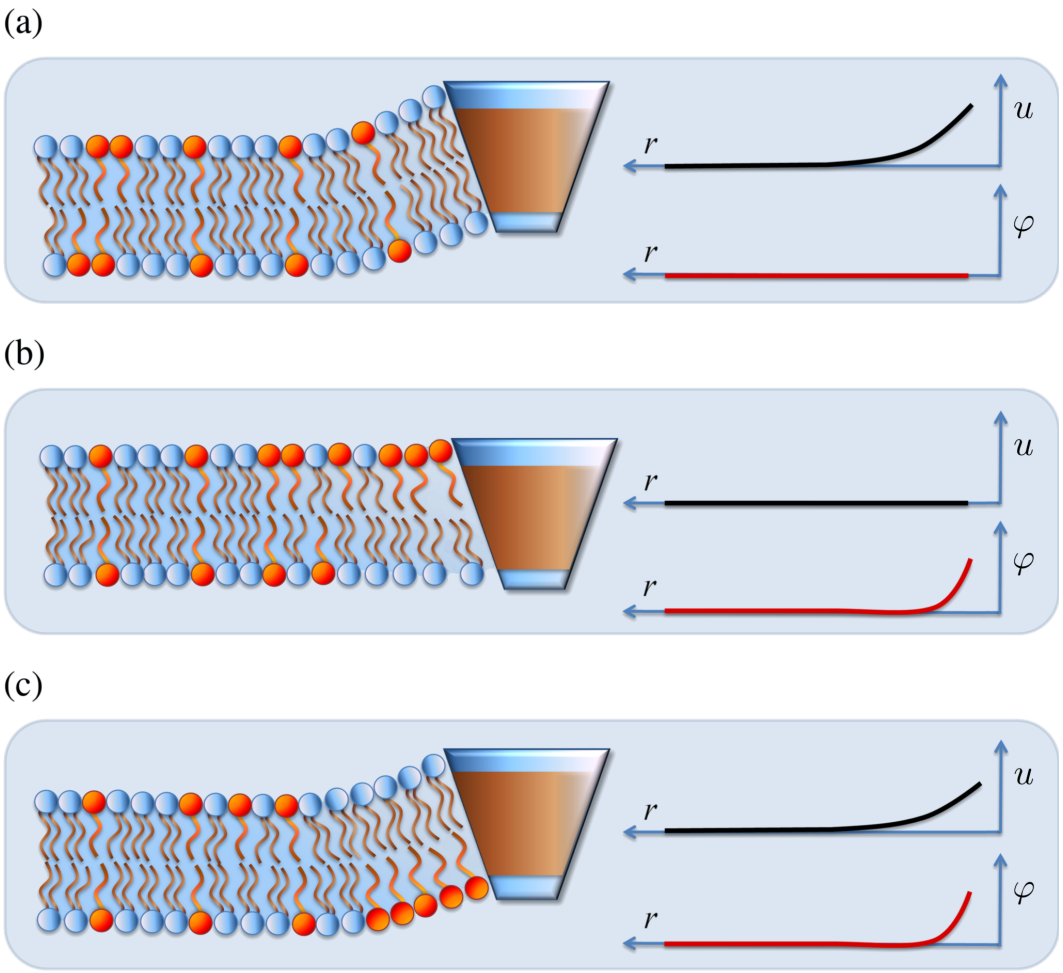

Figure 3.1: Schematic diagrams of a single transmembrane protein embedded into a two-component fluid membrane composed by lysophospholipids (red) and bilayer-forming lipids (blue). By assuming no hydrophobic mismatch, the deformation is characterised by the functions $u(r)$ and $\varphi(r)$, which are the deviation from flatness of the mid-plane of the bilayer, and its local leaflet asymmetry, respectively. The radial distance r is measured from the centre of the protein. Here, (a) depicts one extreme possibility, where the cone-shaped protein induces a mid-plane bending of the bilayer without any changes in the compositional asymmetry between the leaflets. (b) shows another extreme possibility, where the membrane only locally demixes to accommodate the membrane protein, leading to a non-zero φ near the inclusion (namely, a local spontaneous curvature). In practice, the membrane is expected to partially bend and partially demix, as illustrated in (c).

3.2 Theoretical Model

The bilayer in the vicinity of a membrane inclusion may be treated as a continuous elastic medium (as described in Section 2.2). By including a rigid object into the membrane, such as a transmembrane protein, this results in mechanical perturbations about its free equilibrium configuration [139]. In order to analytically compute the deformation energy due to a single membrane protein, we consider an asymptotically flat membrane (see Section 2.1.3). Hence, the Monge parametrisation can be used to describe the mid-plane of the bilayer as a small deviation from flatness of magnitude $u(\mathbf{r})$, where $\mathbf{r}$ is a position vector that lies within a plane normal to the membrane displacement, as illustrated in Figure 3.2.

Thus, in the framework of the Canham–Helfrich theory, the free-energy cost associated with this deformation mode can be written in the linearised Monge representation [14] by employing results derived in (2.22) and (2.24), which gives

$$\mathcal{F}_u = \frac{1}{2} \int_{\mathcal{M}} \left[\sigma \left(\nabla_{\parallel} u \right)^2 + \kappa \left(\nabla_{\parallel}^2 u \right)^2 \right] \mathrm{d}^2\mathbf{r}, \tag{3.1}$$

where κ is the bending rigidity of the membrane, σ is the surface tension, and $\mathcal{M}$ is the region of integration, namely a Cartesian plane without the cross-sectional area of the inclusion. Also, the operators $\nabla_{\parallel}$ and $\nabla_{\parallel}^2$ are defined by the two-dimensional versions of the usual gradient and Laplacian operator, respectively, see Section 2.1.3. Furthermore, the energetic contribution due to the Gaussian bending modulus is neglected throughout this study. Nevertheless, its associated energy contributes, in general, to the overall deformation energy through the topology of the membrane and the geodesic curvature of its boundaries [147, 161].

The addition of curvature sensitive inclusions can lead to a local compositional asymmetry around a transmembrane protein due to their affinity for specific curvature signs (see Figure 3.1). In order to model this, we restrict for simplicity to a two-component fluid membrane given by a mixture of two types of lipids, which has a vanishing composite spontaneous curvature far away from the inclusion. As shown in Figure 3.1, this can be viewed as a mixture of cylindrical and cone-shaped lipids (with zero and non-zero intrinsic monolayer curvature, respectively) in the uniformly mixed phase. The membrane is assumed to have an internal degree of freedom, an order parameter $\varphi(\mathbf{r})$, which is a scalar field defined on $\mathcal{M}$ that quantifies the difference in compositions between the two leaflets (e.g. the local relative concentration of the two types of amphiphiles). By considering small compositional variations, then an effective free-energy for the in-plane ordering can be written as

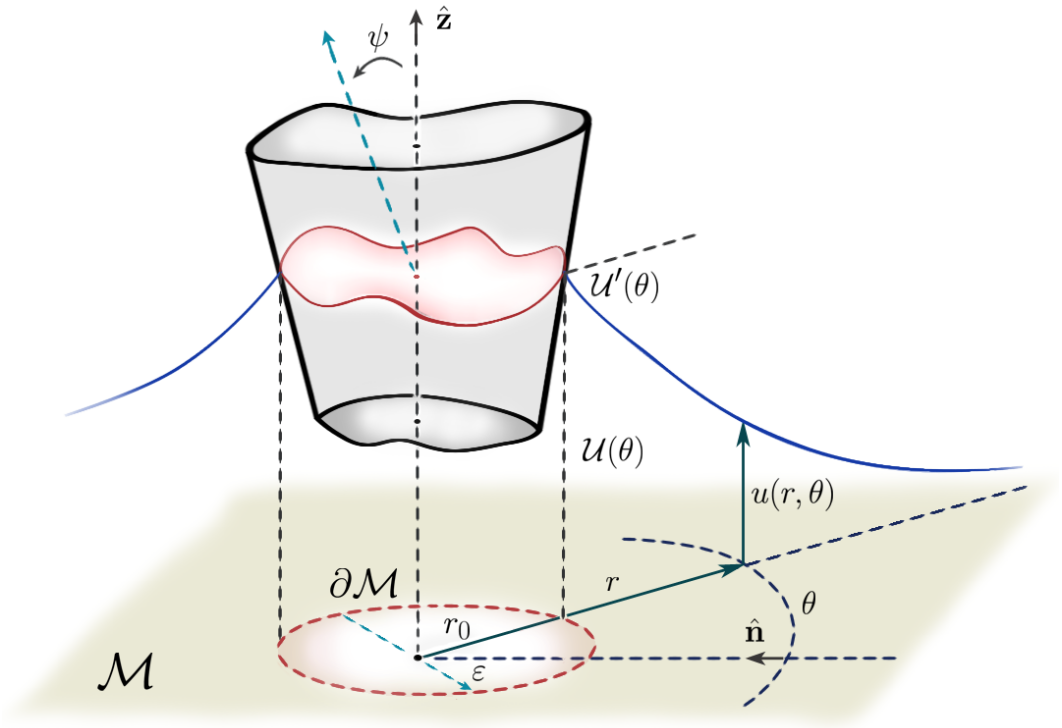

Figure 3.2: The surface of the membrane (blue line) is described in the Monge parametrisation by $u(r,\theta)$, where r is the radial distance from the center of the protein, and θ is the azimuthal angle. Although the protein inclusion is illustrated here as a three-dimensional object, its surface variation along $\hat{\mathbf{z}}$ direction is coarse-grained out, so that its geometry is described by only three parameters, namely the radius r_0, the height $\mathcal{U}(\theta)$, and the contact angle $\mathcal{U}'(\theta)$. These functions parameterize the interface between the inclusion and the mid-plane of the bilayer (red curved line), and define the boundary conditions in this model, i.e. $u(r_0,\theta) = \mathcal{U}(\theta)$ and $\hat{\mathbf{n}} \cdot \nabla u(r_0,\theta) = \mathcal{U}'(\theta)$, with $\hat{\mathbf{n}}$ as the inward unit normal vector. Besides the invariance under the vertical translations, the membrane energy at equilibrium is also required to be invariant under a small tilt angle ψ, where the rotation axis is specified by ε, such that the net torque on the inclusion is zero.

a Landau-Ginzburg expansion, namely

$$\mathcal{F}_\varphi = \frac{1}{2}\int_{\mathcal{M}} \Big[\, a\,\varphi^2 + b\,\big(\nabla_\parallel \varphi\big)^2 + 2\,c\,\varphi\,\big(\nabla_\parallel^2 u\big)\,\Big]\,\mathrm{d}^2\mathbf{r}, \tag{3.2}$$

where only the lowest-order terms are retained, with a, b, and c phenomenological coefficients [162]. The first term in the integrand is assumed to be positive, which tends to keep φ at its equilibrium value, the well-mixed state $\varphi = 0$, whereas the gradient term captures the energy cost for changes in the compositional variation. The last term linearly couples the local compositional difference to the mean curvature of the membrane. This interaction term has initially been proposed in the seminal work of S. Leibler [163] and it is a generalization of the spontaneous curvature energy [164–166]. Therefore, the total free-energy functional that defines our model is given by $\mathcal{F} = \mathcal{F}_u + \mathcal{F}_\varphi$, which is essentially the lowest order expansion in both scalar fields u and φ that is allowed by the symmetries of the system*.

3.2.1 Euler-Lagrange Equations

By rescaling the local compositional asymmetry as $\phi(\mathbf{r}) = (b/c)\,\varphi(\mathbf{r})$ and, moreover, by setting $\alpha^2 = \sigma/\kappa$, $\beta^2 = a/b$ and $\gamma^2 = c^2/\kappa b$, the total free-energy $\mathcal{F}$ can be rewritten as a dimensionless quantity, namely

$$\hat{\mathcal{F}} = \frac{1}{2\pi}\int_{\mathcal{M}} \mathrm{d}^2\mathbf{r}\,\Big\{\,\alpha^2\,(\nabla_\parallel u)^2 + (\nabla_\parallel^2 u)^2 + \gamma^2\,\Big[\beta^2\,\phi^2 + (\nabla_\parallel \phi)^2 + 2\,\phi\,(\nabla_\parallel^2 u)\Big]\Big\}, \tag{3.3}$$

where $\hat{\mathcal{F}} = \mathcal{F}/\,(\pi\,\kappa)$. Here, the free parameters α, β and γ have dimensions of inverse length and they represent the characteristic length scales within our model.

In order to determine the Euler-Lagrange equations for $u(\mathbf{r})$ and $\phi(\mathbf{r})$, we consider the one-parameter family of maps

$$u(\mathbf{r}) \to u_\star(\mathbf{r}) \equiv u(\mathbf{r}) + \epsilon_u\,\delta u(\mathbf{r}) \quad \text{and} \quad \phi(\mathbf{r}) \to \phi_\star(\mathbf{r}) \equiv \phi(\mathbf{r}) + \epsilon_\phi\,\delta\phi(\mathbf{r}), \tag{3.4}$$

where $\delta u(\mathbf{r})$ and $\delta\phi(\mathbf{r})$ are test functions, which are completely arbitrary on $\mathcal{M}$, but fixed on the boundaries of the domain $\partial\mathcal{M}$. Thus, a new functional can be constructed by applying these transformations, say $\hat{\mathcal{F}}_\star(\epsilon_u, \epsilon_\phi)$. Without any loss of generality, by setting $\epsilon_u = \epsilon_\phi = 0$ to be the point in the $\epsilon_u\epsilon_\phi$-space that labels the corresponding minimised functions of (3.3), then $\hat{\mathcal{F}}_\star$ is required to be a minimum

*$\mathcal{F}$ is invariant under the simultaneous transformations $u \mapsto -u$ and $\varphi \mapsto -\varphi$ as required by simple symmetry arguments: if the membrane is inverted, no change in energy should occur.

with respect to both ϵ_u and ϵ_ϕ at this point, that is,

$$\lim_{\epsilon_u \to 0} \lim_{\epsilon_\phi \to 0} \frac{\hat{\mathcal{F}}_\star(\epsilon_u, \epsilon_\phi) - \hat{\mathcal{F}}}{\epsilon_u} = \lim_{\epsilon_u \to 0} \lim_{\epsilon_\phi \to 0} \frac{\hat{\mathcal{F}}_\star(\epsilon_u, \epsilon_\phi) - \hat{\mathcal{F}}}{\epsilon_\phi} = 0. \tag{3.5}$$

Since the explicit form of $\hat{\mathcal{F}}_\star$ to lowest order in ϵ_u and ϵ_ϕ is found to be

$$\begin{aligned}\hat{\mathcal{F}}_\star(\epsilon_u, \epsilon_\phi) = \hat{\mathcal{F}} + \frac{\epsilon_u}{\pi} \int_{\mathcal{M}} \mathrm{d}^2\mathbf{r} \left(\nabla_\parallel^2 u \; \nabla_\parallel^2 \delta u + \alpha^2 \; \nabla_\parallel u \cdot \nabla_\parallel \delta u + \gamma^2 \, \phi \; \nabla_\parallel^2 \delta u \right) + \mathcal{O}(\epsilon_u^2) \\ + \frac{\epsilon_\phi}{\pi} \int_{\mathcal{M}} \mathrm{d}^2\mathbf{r} \; \gamma^2 \left(\beta^2 \phi \, \delta\phi + \nabla_\parallel \phi \cdot \nabla_\parallel \delta\phi + \delta\phi \; \nabla_\parallel^2 u \right) + \mathcal{O}(\epsilon_\phi^2),\end{aligned} \tag{3.6}$$

then equation (3.5) yields that both integrals shown in (3.6) must vanish. Hence, by employing the divergence theorem and the method of integration by parts [49], these integrals can be reduced to

$$\oint_{\partial\mathcal{M}} \delta\phi(\mathbf{r}) \, \frac{\partial \phi}{\partial n} - \int_{\mathcal{M}} \mathrm{d}^2\mathbf{r} \, \left[(\nabla_\parallel^2 - \beta^2)\phi - \nabla_\parallel^2 u \right] \delta\phi(\mathbf{r}) = 0 \tag{3.7}$$

and

$$\begin{aligned}\oint_{\partial\mathcal{M}} \delta u(\mathbf{r}) \, \frac{\partial}{\partial n} \left(\alpha^2 \, u - \gamma^2 \, \phi - \nabla_\parallel^2 u \right) + \left(\nabla_\parallel^2 u + \gamma^2 \, \phi \right) \frac{\partial}{\partial n} \delta u(\mathbf{r}) \\ + \int_{\mathcal{M}} \mathrm{d}^2\mathbf{r} \, \left[\nabla_\parallel^2 \, (\nabla_\parallel^2 - \alpha^2) u + \gamma^2 \; \nabla_\parallel^2 \, \phi \right] \delta u(\mathbf{r}) = 0,\end{aligned} \tag{3.8}$$

where we assume that $u(\mathbf{r})$ and $\phi(\mathbf{r})$ vanish in the far-field limit, and $\frac{\partial}{\partial n} := \hat{\mathbf{n}} \cdot \nabla_\parallel$ denotes the normal derivative, with $\hat{\mathbf{n}}$ as the unit vector normal to the boundary of the domain $\partial\mathcal{M}$, pointing toward the centre of the inclusion (see Figure 3.2).

To obtain the Euler-Lagrange equations, the boundary terms in both (3.7) and (3.8) are required to cancel out [167]. In the latter case, this can be achieved by demanding that both δu and the normal component of its gradient, $\frac{\partial}{\partial n}\delta u$, vanish everywhere on $\partial\mathcal{M}$. However, from (3.4), this is equivalent to fixing the field $u(\mathbf{r})$ and its normal derivative on the boundary. In the same way, the vanishing of the boundary terms in (3.7) can be obtained by setting the normal derivative $\frac{\partial}{\partial n}\phi = 0$ everywhere on $\partial\mathcal{M}$ (Neumann condition), or by requiring that $\delta\phi = 0$, namely the compositional asymmetry field ϕ is fixed on the boundary (Dirichlet condition).

As a consequence, the requirements of vanishing boundary terms provide the appropriate choices of boundary conditions at the protein-membrane interface $\partial\mathcal{M}$.

Hereinafter, we choose the following boundary conditions:

$$u(\mathbf{r})\Big|_{\partial\mathcal{M}} = \mathcal{U}, \qquad \text{and} \qquad \hat{\mathbf{n}}\cdot\nabla_{\parallel}\, u\Big|_{\partial\mathcal{M}} = \mathcal{U}', \tag{3.9}$$

where the functions $\mathcal{U}$ and $\mathcal{U}'$ describe the height and the contact angle at which the mid-plane of the membrane meets the rigid inclusion, respectively, as illustrated in Figure 3.2, which may be obtained from the protein crystallographic data (appropriately coarse-grained). This choice of boundary conditions is motivated by the strong coupling between the transmembrane domain of the rigid inclusion and the hydrophobic core of the membrane [162]. Since $\delta u(\mathbf{r})$ and $\delta\phi(\mathbf{r})$ are (by definition) completely arbitrary in the bulk, then (3.7) and (3.8) can be reduced to

$$\nabla_{\parallel}^2\, u = (\nabla_{\parallel}^2 - \beta^2)\phi \quad \text{and} \quad \nabla_{\parallel}^2(\nabla_{\parallel}^2 - \alpha^2)\, u \,+\, \gamma^2\, \nabla_{\parallel}^2\, \phi = 0, \tag{3.10}$$

respectively, which are obtained regardless of the choice of boundary conditions on the compositional asymmetry $\phi(\mathbf{r})$. These are the Euler-Lagrange equations that both scalar fields $u(\mathbf{r})$ and $\phi(\mathbf{r})$ must satisfy in the lowest energy state of the system.

3.2.2 General Solutions

The Euler-Lagrange equations (3.10) can be combined to obtain a fourth order differential equation in terms of $\phi(\mathbf{r})$ only, that is,

$$\left(\nabla_{\parallel}{}^2 - k_+^2\right)\left(\nabla_{\parallel}{}^2 - k_-^2\right)\phi = 0, \tag{3.11}$$

where $k_{\pm}^2$ depends solely on α, β and γ, namely

$$k_{\pm}^2 = \frac{1}{2}\left(\alpha^2 + \beta^2 - \gamma^2\right) \pm \frac{1}{2}\sqrt{\left(\alpha^2 + \beta^2 - \gamma^2\right)^2 - 4\alpha^2\beta^2}\,. \tag{3.12}$$

It can be shown that $k_{\pm}^2 > 0$ if and only if $\gamma \leq |\alpha - \beta|$ and that $k_{\pm}^2 < 0$ if and only if $\gamma \geq \alpha + \beta$, where γ is strictly positive[†] Furthermore, they become complex if the coupling constant $\gamma \in (\,|\alpha - \beta|,\, |\alpha + \beta|\,)$, as illustrated in Figure 3.3. The physical significance of these complex (and purely imaginary) solutions for $k_{\pm}$ is discussed in Section 3.3.1. We restrict for now to the case when the coupling term $\gamma < |\alpha - \beta|$, which implies that the values of $k_{\pm}$ are strictly positive and $k_- \neq k_+$. Accordingly, a solution of the partial differential equation (3.11) that vanishes in the far-field can

[†]Although both scalar fields u and ϕ are invariant under $\gamma \mapsto -\gamma$, the sign choice of γ is purely a convention of whether we refer to the enrichment of a membrane leaflet that couples to positive curvature, or the depletion of one that couples to negative curvature.

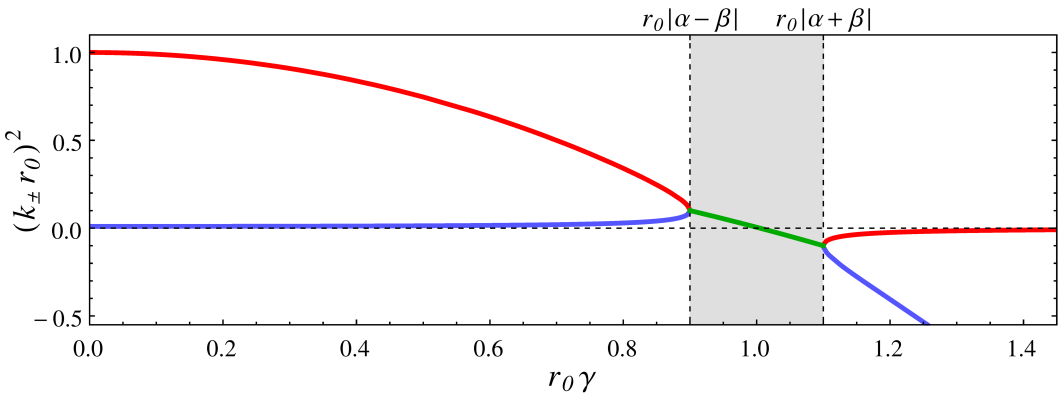

Figure 3.3: Plot of $k_\pm^2$ against the coupling constant γ, with $\alpha\, r_0 = 0.1$ and $\beta\, r_0 = 1.0$, where r_0 is the radius of the protein. This shows that both k_+ (red line) and k_- (blue line) are real for $\gamma < |\alpha - \beta|$, and purely imaginary for $\gamma > \alpha + \beta$. The grey shaded area illustrates the region where $k_\pm^2$ are complex, while the green line is the projection of these solutions onto the real space.

be expressed in the following form:

$$\phi(r,\theta) = \phi_+(r,\theta) + \phi_-(r,\theta), \tag{3.13}$$

where r and θ are the polar coordinates, with the origin chosen in the centre of the membrane inclusion, and the functions $\phi_\pm$ are defined by

$$\phi_\pm(r,\theta) = \frac{k_\pm^2}{k_\pm^2 - \beta^2} \sum_{n=0}^{\infty} \mathcal{V}_n^\pm(\theta)\, K_n(k_\pm r), \tag{3.14}$$

where $\mathcal{V}_n^\pm(\theta) = \mathcal{A}_n^\pm \cos(n\theta) + \mathcal{B}_n^\pm \sin(n\theta)$, with $\mathcal{A}_n^\pm$ and $\mathcal{B}_n^\pm$ as arbitrary constants, and K_n are the modified Bessel functions of the second kind of integer order n.

As a result, this solution can now be used to find the membrane shape $u(r,\,\theta)$ by direct substitution into the first Euler-Lagrange equation in (3.10), which yields

$$u(r,\theta) = u_+(r,\theta) + u_-(r,\theta) + u_h(r,\theta), \tag{3.15}$$

where u_h is the associated homogeneous solution that solves the two-dimensional version of the Laplace equation, $\nabla_\parallel^2\, u_h = 0$, namely

$$u_h(r,\theta) = \sum_{n=0}^{\infty} \mathcal{W}_n(\theta)\, r^{-n}, \tag{3.16}$$

in which $\mathcal{W}_n(\theta) = \mathcal{X}_n \cos(n\theta) + \mathcal{Y}_n \sin(n\theta)$, with $\mathcal{X}_n$ and $\mathcal{Y}_n$ as arbitrary constants.

This expression is obtained by excluding the solutions that diverge at infinity, i.e. u must remain finite far way from the membrane inclusion. The other two functions in (3.15) are the corresponding inhomogeneous solutions, which are found to be

$$u_{\pm}(r,\theta) = \sum_{n=0}^{\infty} \mathcal{V}_n^{\pm}(\theta)\, K_n(k_{\pm} r). \tag{3.17}$$

Therefore, the deformation profile $u(r,\theta)$ contains six arbitrary constants for each Bessel-Fourier mode, which can be determined by employing the boundary conditions at the interface between the inclusion and the membrane. Here, we consider rigid inclusions with radial symmetry along a central axis $\hat{\mathbf{z}}$ normal to the surface $\mathcal{M}$, as depicted in Figure 3.2. This constraints the shape $\partial\mathcal{M}$ of the membrane inclusion to be at a fixed radius r_0, which allows us to express the boundary conditions in cylindrical coordinates, as presented in the next section.

3.2.3 Neumann Boundary Condition

By choosing a Neumann condition for the local compositional asymmetry $\phi(\mathbf{r})$ on the boundary $\partial\mathcal{M}$ (later, the Dirichlet condition will be examined as well), the unknown functions $\mathcal{V}_n^{\pm}$ and $\mathcal{W}_n$ can be determined from the boundary conditions

$$\hat{\mathbf{n}} \cdot \nabla_{\parallel}\, \phi\,(r_0,\theta) = 0, \tag{3.18}$$

$$u\,(r_0,\theta) = \mathcal{U}(\theta) := z_0 + \sum_{n=1}^{\infty} z_n \cos(n\theta - \xi_n), \tag{3.19}$$

and

$$\hat{\mathbf{n}} \cdot \nabla_{\parallel}\, u\,(r_0,\theta) = \mathcal{U}'(\theta) := \delta_0 + \sum_{n=1}^{\infty} \delta_n \cos(n\theta - \chi_n), \tag{3.20}$$

where the functions $\mathcal{U}(\theta)$ and $\mathcal{U}'(\theta)$ are written in terms of a Fourier series [49], so that each $\mathcal{V}_n^{\pm}(\theta)$ and $\mathcal{W}_n(\theta)$ can be evaluated (individually) at every order in the series. Moreover, these conditions can be re-written in a matrix form as follows:

$$\begin{pmatrix} K_n(k_+r_0) & K_n(k_-r_0) & 1 \\ \mathcal{L}_n^{+} K_n(k_+r_0) & \mathcal{L}_n^{-} K_n(k_-r_0) & n \\ f_+ K_n(k_+r_0) & f_- K_n(k_-r_0) & 0 \end{pmatrix} \begin{pmatrix} \mathcal{V}_n^{+}(\theta) \\ \mathcal{V}_n^{-}(\theta) \\ \mathcal{W}(\theta)\, r_0^{-n} \end{pmatrix} = \begin{pmatrix} z_n \cos(n\theta - \xi_n) \\ r_0\, \delta_n \cos(n\theta - \chi_n) \\ 0 \end{pmatrix}, \tag{3.21}$$

with the phases $\chi_0 = \xi_0 = 0$, the coefficients $f_{\pm} = k_{\pm}^2 \,/\, \left(k_{\pm}^2 - \beta^2\right)$, and

$$\mathcal{L}_n^{\pm} = -\frac{k_{\pm} r_0\, K_n'(k_{\pm} r_0)}{K_n(k_{\pm} r_0)} = n + \frac{k_{\pm} r_0\, K_{n-1}(k_{\pm} r_0)}{K_n(k_{\pm} r_0)}, \tag{3.22}$$

where the last step is found by using a recurrence relation of the modified Bessel functions of the second kind [168, 169]:

$$K_n'(x) = -K_{n-1}(x) - \frac{n}{x} K_n(x), \tag{3.23}$$

for any real number x, where the prime symbol denotes here a derivative with respect to the argument of the function. To find $\mathcal{V}_n^{\pm}(\theta)$ and $\mathcal{W}_n(\theta)$, the matrix in equation (3.21), say $\mathbf{M}$, must be invertible, namely its determinant is required to be non-zero [49]. This implies that

$$\mathcal{N}_n := f_- \mathcal{L}_n^-(n - \mathcal{L}_n^+) - f_+ \mathcal{L}_n^+(n - \mathcal{L}_n^-) \neq 0, \tag{3.24}$$

which allows us to obtain a unique solution. By multiplying (3.21) by the inverse matrix of $\mathbf{M}$, this gives

$$\mathcal{V}_n^{\pm}(\theta) = \pm \frac{f_{\mp} \mathcal{L}_n^{\mp}}{\mathcal{N}_n \, K_n(k_{\pm} r_0)} \left[n z_n \cos(n\theta - \xi_n) - r_0 \delta_n \cos(n\theta - \chi_n) \right], \tag{3.25}$$

and

$$\begin{aligned} \mathcal{W}_n(\theta) = \frac{1}{r_0^{-n} \mathcal{N}_n} \big[& \mathcal{L}_n^+ \mathcal{L}_n^- \, (f_+ - f_-) \, z_n \cos(n\theta - \xi_n) \\ & - \left(f_+ \mathcal{L}_n^+ - f_- \mathcal{L}_n^- \right) r_0 \delta_n \cos(n\theta - \chi_n) \big]. \end{aligned} \tag{3.26}$$

As a result, the height profile of the membrane $u(r, \theta)$, and its compositional asymmetry $\phi(r, \theta)$ are completely determined by the boundary conditions (3.18 – 3.20). However, $\mathcal{U}(\theta)$ and $\mathcal{U}'(\theta)$ are not entirely arbitrary, as the height z_0 is set by the minimisation of the free-energy (3.3), which gives the balance of normal forces on any infinitesimal patch of the membrane. Thus, using the explicit form of (3.15), (3.25) and (3.26), and the requirement that $u(r, \theta)$ vanishes in the far-field, we obtain

$$z_0 = r_0 \, \delta_0 \, \frac{f_+ \mathcal{L}_0^+ - f_- \mathcal{L}_0^-}{\mathcal{L}_0^+ \mathcal{L}_0^- \, (f_+ - f_-)}. \tag{3.27}$$

Also, since the membrane inclusion is assumed to be free to tilt about the central axis $\hat{\mathbf{z}}$, another equilibrium condition that the system must fulfil is the balance of torques on the rigid inclusion, which is detailed in the next section.

3.2.4 Torque Balance and Deformation Energy

The system must satisfy the equilibrium requirements of zero net torques and vanishing normal forces on the membrane inclusion. The latter yields the condition

given by (3.27). On the other hand, the torque balance requires the effective free-energy (3.3) to be invariant under the transformations

$$\mathcal{U}(\theta) \mapsto \mathcal{U}(\theta) - r_0 \psi \cos(\theta - \varepsilon) \quad \text{and} \quad \mathcal{U}'(\theta) \mapsto \mathcal{U}'(\theta) + \psi \cos(\theta - \varepsilon), \tag{3.28}$$

where ψ is a small tilt angle about the central axis $\hat{\mathbf{z}}$, and the azimuthal angle ε specifies the orientation of this tilt (see Figure 3.2). The small angle approximation on ψ is enforced so that the projected area enclosed by $\partial\mathcal{M}$ remains circular under such transformations. It is noteworthy to mention that the transformations in (3.28) only affect the corresponding first-order Fourier modes of $\mathcal{U}(\theta)$ and $\mathcal{U}'(\theta)$. To find the effect due to this tilt balance, we need to first compute the deformation energy.

Interestingly, the free-energy functional (3.3) can be reduced to a line integral over the boundary at the inclusion-membrane interface $\partial\mathcal{M}$. Using the divergence theorem and the vector identity $\nabla_\parallel \mathcal{A} \cdot \nabla_\parallel \mathcal{B} = \nabla_\parallel \cdot \big(\mathcal{A} \nabla_\parallel \mathcal{B}\big) - \mathcal{A} \nabla_\parallel^2 \mathcal{B}$, with $\mathcal{A}$ and $\mathcal{B}$ as scalar fields, then

$$\int_{\mathcal{M}} \mathrm{d}^2\mathbf{r} \; (\nabla_\parallel u)^2 = \oint_{\partial\mathcal{M}} u \, \frac{\partial u}{\partial n} - \int_{\mathcal{M}} \mathrm{d}^2\mathbf{r} \; \Big(u \, \nabla_\parallel^2 u \Big), \tag{3.29}$$

where $\frac{\partial}{\partial n} = \hat{\mathbf{n}} \cdot \nabla_\parallel$ denotes the normal derivative. Similarly, an identical expression can be found for $\phi(\mathbf{r})$. Thus, the free-energy (3.3) can be written as

$$\hat{\mathcal{F}} = \frac{1}{2\pi} \oint_{\partial\mathcal{M}} \left(\alpha^2 u \, \frac{\partial u}{\partial n} + \gamma^2 \phi \, \frac{\partial \phi}{\partial n} \right) + \frac{1}{2\pi} \int_{\mathcal{M}} \mathrm{d}^2\mathbf{r} \; (\nabla_\parallel^2 u) \Big[(\nabla_\parallel^2 - \alpha^2) \, u \, + \, \gamma^2 \phi \Big], \tag{3.30}$$

where the last term is simplified to this form by using the first Euler-Lagrange equation in (3.10). Furthermore, by denoting the term in square brackets by w and using the identity $\nabla_\parallel \big(w \, \nabla_\parallel u - u \, \nabla_\parallel w \big) = w \, \nabla_\parallel^2 u - u \, \nabla_\parallel^2 w$, we find

$$\hat{\mathcal{F}} = \frac{1}{2\pi} \oint_{\partial\mathcal{M}} \left(\alpha^2 u \, \frac{\partial u}{\partial n} + \gamma^2 \phi \, \frac{\partial \phi}{\partial n} + w \, \frac{\partial u}{\partial n} - u \, \frac{\partial w}{\partial n} \right), \tag{3.31}$$

where the second Euler-Lagrange equation (that is, $\nabla_\parallel^2 w = 0$) is used to remove the bulk terms and rewrite the total free-energy as a line integral over $\partial\mathcal{M}$.

Also, since the solutions u_h and $u_\pm$ satisfy $\nabla_\parallel^2 u_h = 0$ and $(\nabla_\parallel^2 - k_\pm^2) \, u_\pm = 0$, respectively, w is found to be

$$w(r, \theta) = -\alpha^2 u_h(r, \theta) = -\alpha^2 \sum_{n=0}^{\infty} \mathcal{W}_n(\theta) \, r^{-n}, \tag{3.32}$$

where the final step is derived by using the explicit form of $u_h(r, \theta)$. As a result,

this gives that

$$\hat{\mathcal{F}} = \frac{\alpha^2}{2\pi} \oint_{\partial\mathcal{M}} \left(u\,\frac{\partial u}{\partial n} + u\,\frac{\partial u_h}{\partial n} - u_h\,\frac{\partial u}{\partial n} \right) + \frac{\gamma^2}{2\pi} \oint_{\partial\mathcal{M}} \phi\,\frac{\partial \phi}{\partial n}, \tag{3.33}$$

which can be simplified further, by employing the boundary conditions (3.18 – 3.20),

$$\hat{\mathcal{F}} = \frac{\alpha^2}{2\pi} \int_0^{2\pi} \mathrm{d}\theta \left[r_0\,\mathcal{U}'(\theta)\,\mathcal{U}(\theta) + \sum_{n=0}^{\infty} \mathcal{W}_n(\theta)\, r_0^{-n} \Big(n\,\mathcal{U}(\theta) - r_0\,\mathcal{U}'(\theta) \Big) \right]. \tag{3.34}$$

In this form, we can easily apply the transformations (3.28), which couple only to the first Fourier modes of (3.19) and (3.20). By using the orthogonality relationships of the Fourier modes, the membrane deformation energy, in terms of the series (3.19) and (3.20), becomes $\hat{\mathcal{F}} = \sum_{n=0}^{\infty} \hat{\mathcal{F}}_n + \hat{\mathcal{F}}_{\mathrm{tilt}}$, where $\hat{\mathcal{F}}_n$ is defined by

$$\begin{aligned} \hat{\mathcal{F}}_n = \frac{\alpha^2}{\mathcal{N}_n\,\vartheta_n} \Big[& \left(f_+ \mathcal{L}_n^+ - f_- \mathcal{L}_n^- \right) r_0^2 \delta_n^2 - 2\,n\,z_n\,r_0\,\delta_n \left(f_+ \mathcal{L}_n^+ - f_- \mathcal{L}_n^- \right) \cos(\xi_n - \chi_n) \\ & + \; n\,\mathcal{L}_n^+ \mathcal{L}_n^- \left(f_+ - f_- \right) z_n^2 \Big], \end{aligned} \tag{3.35}$$

with $\vartheta_0 = 1$ and $\vartheta_n = 2$ for any $n > 0$. This term represents the energy associated to each Fourier-Bessel mode, whereas the term given by $\hat{\mathcal{F}}_{\mathrm{tilt}}$ is the energy contribution that accounts for the torque balance, namely

$$\hat{\mathcal{F}}_{\mathrm{tilt}} = \frac{\alpha^2 \left(z_{\mathrm{tilt}}^2 - 2\,z_{\mathrm{tilt}}\,r_0 \delta_{\mathrm{tilt}} \cos(\xi_1 - \chi_1) + r_0^2 \delta_{\mathrm{tilt}}^2 \right)}{2\,\mathcal{N}_1 \left[f_- \mathcal{L}_1^- (3 + \mathcal{L}_1^+) - f_+ \mathcal{L}_1^+ (3 + \mathcal{L}_1^-) \right]^{-1}}, \tag{3.36}$$

which is found by minimising the total deformation energy of the membrane with respect to ψ and ε, where their minimum values obey the simultaneous equations:

$$\begin{cases} r_0 \psi \cos(\varepsilon) & = z_{\mathrm{tilt}} \cos\xi_1 + r_0 \delta_{\mathrm{tilt}} \cos\chi_1 \\ r_0 \psi \sin(\varepsilon) & = z_{\mathrm{tilt}} \sin\xi_1 + r_0 \delta_{\mathrm{tilt}} \sin\chi_1. \end{cases} \tag{3.37}$$

Here, the tilt coefficients δ_{tilt} and z_{tilt} are defined by

$$\delta_{\mathrm{tilt}} = \delta_1\,\frac{2\left(f_+ \mathcal{L}_1^+ - f_- \mathcal{L}_1^- \right)}{f_+ \mathcal{L}_1^+ \left(3 + \mathcal{L}_1^- \right) - f_- \mathcal{L}_1^- \left(3 + \mathcal{L}_1^+ \right)}, \tag{3.38}$$

and

$$z_{\mathrm{tilt}} = z_1\,\frac{f_+ \mathcal{L}_1^+ \left(1 + \mathcal{L}_1^- \right) - f_- \mathcal{L}_1^- \left(1 + \mathcal{L}_1^+ \right)}{f_+ \mathcal{L}_1^+ \left(3 + \mathcal{L}_1^- \right) - f_- \mathcal{L}_1^- \left(3 + \mathcal{L}_1^+ \right)}. \tag{3.39}$$

Hence, the contributions to $u(\mathbf{r})$ and $\phi(\mathbf{r})$ due to the torque balance can be found as well by applying (3.28) to the matrix equation (3.21), namely

$$u_{\text{tilt}}(r,\theta) = \mathcal{V}^{+}_{\text{tilt}}(\theta)\, K_1(k_+ r) + \mathcal{V}^{-}_{\text{tilt}}(\theta)\, K_1(k_- r) + \mathcal{W}_{\text{tilt}}(\theta)\, r^{-1} \tag{3.40}$$

and

$$\phi_{\text{tilt}}(r,\theta) = f_+ \mathcal{V}^{+}_{\text{tilt}}(\theta)\, K_1(k_+ r) + f_- \mathcal{V}^{-}_{\text{tilt}}(\theta)\, K_1(k_- r), \tag{3.41}$$

respectively, where the azimuthal functions $\mathcal{V}^{\pm}_{\text{tilt}}(\theta)$ and $\mathcal{W}_{\text{tilt}}(\theta)$ are given by

$$\mathcal{V}^{\pm}_{\text{tilt}}(\theta) = \mp \frac{2\, f_{\mp} \mathcal{L}^{\mp}_1}{\mathcal{N}_1\, K_1\,(k_\pm r_0)} \big[z_{\text{tilt}} \cos(\theta - \xi_1) - r_0 \delta_{\text{tilt}} \cos(\theta - \chi_1) \big], \tag{3.42}$$

and

$$\mathcal{W}_{\text{tilt}}(\theta) = \frac{z_{\text{tilt}} \cos(\theta - \xi_1) - r_0 \delta_{\text{tilt}} \cos(\theta - \chi_1)}{r_0^{-1} \mathcal{N}_1 \left[f_- \mathcal{L}^{-}_1 \left(1 + \mathcal{L}^{+}_1\right) - f_+ \mathcal{L}^{+}_1 \left(1 + \mathcal{L}^{-}_1\right) \right]^{-1}}. \tag{3.43}$$

As a result, the general solutions of the membrane profile $u(r,\theta)$ and its associated compositional variation $\phi(r,\theta)$ that satisfy the boundary conditions (3.18 – 3.20), together with the requirements of vanishing normal forces and zero net torques, are given by

$$u(r,\theta) = u_{\text{tilt}}(r,\theta) + \sum_{n=0}^{\infty} \mathcal{V}^{+}_n(\theta)\, K_n(k_+ r) + \mathcal{V}^{-}_n(\theta)\, K_n(k_- r) + \mathcal{W}_n(\theta)\, r^{-n}, \tag{3.44}$$

and

$$\phi(r,\theta) = \phi_{\text{tilt}}(r,\theta) + \sum_{n=0}^{\infty} f_+ \mathcal{V}^{+}_n(\theta)\, K_n(k_+ r) + f_- \mathcal{V}^{-}_n(\theta)\, K_n(k_- r), \tag{3.45}$$

respectively, where u_{tilt} and ϕ_{tilt} are the contributions due to the torque balance, as given in (3.40) and (3.41), and $\mathcal{V}^{\pm}_n(\theta)$ and $\mathcal{W}_n(\theta)$ are prescribed by (3.25) and (3.26).

3.2.5 Dirichlet Boundary Condition

Herein, we consider the same boundary conditions on the membrane height $u(\mathbf{r})$ as before, but a Dirichlet boundary condition is used for $\phi(\mathbf{r})$ on $\partial\mathcal{M}$, namely

$$\phi(r_0,\theta) = \Phi(\theta) \equiv \sum_{n=0}^{\infty} \varphi_n \cos(n\theta - \nu_n), \tag{3.46}$$

where $\nu_0 = 0$. The function $\Phi(\theta)$ gives the compositional asymmetry field at the interface between the membrane and the rigid inclusion (of radius r_0), which together

with the other boundary conditions completely determine $\mathcal{V}_n^{\pm}(\theta)$ and $\mathcal{W}_n(\theta)$ in (3.15) and (3.13). As before, these conditions can written as a matrix equation:

$$\begin{pmatrix} K_n(k_+r_0) & K_n(k_-r_0) & 1 \\ \mathcal{L}_n^+ K_n(k_+r_0) & \mathcal{L}_n^- K_n(k_-r_0) & n \\ f_+ K_n(k_+r_0) & f_- K_n(k_-r_0) & 0 \end{pmatrix} \begin{pmatrix} \mathcal{V}_n^+(\theta) \\ \mathcal{V}_n^-(\theta) \\ \mathcal{W}(\theta)\, r_0^{-n} \end{pmatrix} = \begin{pmatrix} z_n \cos(n\theta - \xi_n) \\ r_0\, \delta_n \cos(n\theta - \chi_n) \\ \varphi_n \cos(n\theta - \nu_n) \end{pmatrix}, \quad (3.47)$$

with $n \geq 0$ and $\mathcal{L}_n^{\pm}$ as defined by equation (3.22). By assuming that the square matrix in equation (3.47) is nonsingular, that is,

$$\mathcal{P}_n := f_-(n - \mathcal{L}_n^+) - f_+(n - \mathcal{L}_n^-) \neq 0, \quad (3.48)$$

this allows us to find the azimuthal functions as follows:

$$\mathcal{V}_n^{\pm}(\theta) = \pm \frac{f_{\mp}\mathcal{L}_n^{\mp}\left[n z_n \cos(n\theta - \xi_n) - r_0 \delta_n \cos(n\theta - \chi_n)\right] - (n - \mathcal{L}_n^{\mp})\, \varphi_n \cos(n\theta - \nu_n)}{\mathcal{P}_n\, K_n(k_{\pm} r_0)} \quad (3.49)$$

and

$$\mathcal{W}_n(\theta) = \frac{1}{r_0^{-n}\, \mathcal{P}_n} \big[z_n \left(f_+\mathcal{L}_n^- - f_-\mathcal{L}_n^+\right) \cos(n\theta - \xi_n) - (f_+ - f_-)\, r_0\, \delta_n \cos(n\theta - \chi_n) + \left(\mathcal{L}_n^+ - \mathcal{L}_n^-\right) \varphi_n \cos(n\theta - \nu_n) \big]. \quad (3.50)$$

Moreover, as the membrane profile $u(r, \theta)$ must vanishes in the far-field limit, then the height z_0 is found to be

$$z_0 = \frac{(f_+ - f_-)\, r_0\, \delta_0 - \left(\mathcal{L}_0^+ - \mathcal{L}_0^-\right) \varphi_0}{f_+\mathcal{L}_0^- - f_-\mathcal{L}_0^+}. \quad (3.51)$$

Through the functions $u(r, \theta)$ and $\phi(r, \theta)$, the total deformation energy of the membrane, as given in equation (3.34), can be now computed as a Fourier series, $\hat{\mathcal{F}} = \sum_{n=0}^{\infty} \hat{\mathcal{F}}_n + \hat{\mathcal{F}}_{\text{tilt}}$, where $\hat{\mathcal{F}}_n$ is the energy associated to each Fourier-Bessel mode:

$$\hat{\mathcal{F}}_n = \frac{\gamma^2 \varphi_n^2}{\mathcal{P}_n\, \vartheta_n} \left[f_-\mathcal{L}_n^-(n - \mathcal{L}_n^+) - f_+\mathcal{L}_n^+(n - \mathcal{L}_n^-) \right] + \frac{\alpha^2}{\mathcal{P}_n\, \vartheta_n} \Big\{ n\, z_n^2 \left(f_+\mathcal{L}_n^- - f_-\mathcal{L}_n^+\right) + (f_+ - f_-)\, r_0^2 \delta_n^2 - 2\, n\, z_n r_0 \delta_n\, (f_+ - f_-) \cos(\xi_n - \chi_n) + 2\, \varphi_n \left(\mathcal{L}_n^+ - \mathcal{L}_n^-\right) \left[n z_n \cos(\nu_n - \xi_n) - r_0 \delta_n \cos(\nu_n - \chi_n) \right] \Big\}, \quad (3.52)$$

with $\vartheta_0 = 1$ and $\vartheta_n = 2$ for any $n > 0$. The second term is the additional energetic contribution due to the balance of torques on the rigid inclusion, which requires

that the total energy to be invariant under a tilt transformation of the form (3.28). Thus, the explicit expression of $\hat{\mathcal{F}}_{\rm tilt}$ can be determined as follows:

$$\hat{\mathcal{F}}_{\rm tilt} = \frac{\alpha^2}{2\,\mathcal{P}_1}\left[f_-\mathcal{L}_1^-(3+\mathcal{L}_1^+) - f_+\mathcal{L}_1^+(3+\mathcal{L}_1^-)\right]\left[z_{\rm tilt}^2 - 2\,z_{\rm tilt}\,r_0\delta_{\rm tilt}\cos(\xi_1-\chi_1)\right.$$
$$\left. + r_0^2\delta_{\rm tilt}^2 - 2\,\varphi_{\rm tilt}\,r_0\delta_{\rm tilt}\cos(\nu_1-\chi_1) + 2\,z_{\rm tilt}\,\varphi_{\rm tilt}\cos(\xi_1-\nu_1) + \varphi_{\rm tilt}^2\right], \quad (3.53)$$

where the tilt coefficients $z_{\rm tilt}$, $\delta_{\rm tilt}$ and $\varphi_{\rm tilt}$ are given by

$$\delta_{\rm tilt} = \frac{2\delta_1\,(f_+ - f_-)}{f_+\left(3+\mathcal{L}_1^-\right) - f_-\left(3+\mathcal{L}_1^+\right)}, \quad z_{\rm tilt} = z_1\,\frac{f_+\left(1+\mathcal{L}_1^-\right) - f_-\left(1+\mathcal{L}_1^+\right)}{f_+\left(3+\mathcal{L}_1^-\right) - f_-\left(3+\mathcal{L}_1^+\right)}, \quad (3.54)$$

and

$$\varphi_{\rm tilt} = \frac{2\,\varphi_1\left(\mathcal{L}_1^+ - \mathcal{L}_1^-\right)}{f_+\left(3+\mathcal{L}_1^-\right) - f_-\left(3+\mathcal{L}_1^+\right)}, \quad (3.55)$$

respectively. Moreover, this leads to the additional fields $u_{\rm tilt}(r,\theta)$ and $\phi_{\rm tilt}(r,\theta)$, which yield the corresponding contributions to $u(r,\theta)$ and $\phi(r,\theta)$ that allow for a vanishing net torque. They can also be written in terms of the functions $\mathcal{V}_{\rm tilt}^{\pm}(\theta)$ and $\mathcal{W}_{\rm tilt}(\theta)$, which are found to be

$$\mathcal{V}_{\rm tilt}^{\pm}(\theta) = \mp\,\frac{f_\mp\left[z_1\cos(\theta-\xi_1) + r_0\delta_1\cos(\theta-\chi_1)\right] + \left(3+\mathcal{L}_1^\mp\right)\varphi_1\cos(\theta-\nu_1)}{\left[f_+\,(3+\mathcal{L}_1^-) - f_-\,(3+\mathcal{L}_1^+)\right]K_1(k_\pm r_0)}, \quad (3.56)$$

and

$$\mathcal{W}_{\rm tilt}(\theta) = \frac{(f_+ - f_-)\left[z_1\cos(\theta-\xi_1) + r_0\delta_1\cos(\theta-\chi_1)\right] - \left(\mathcal{L}_1^+ - \mathcal{L}_1^-\right)\varphi_1\cos(\theta-\nu_1)}{\left[f_+\,(3+\mathcal{L}_1^-) - f_-\,(3+\mathcal{L}_1^+)\right]r_0^{-1}}. \quad (3.57)$$

Interestingly, if the total deformation energy is minimised with respect to φ_n and ν_n, then we retrieve the same solutions as found for the Neumann boundary case. Thus, in the absence of any constrains on ϕ at the inclusion-membrane interface, the Neumann boundary condition gives the most energetically favourable states.

3.3 Applications and Specific Solutions

In this section, we apply this methodology to a number of specific problems of biological relevance. In particular, we discuss the consequences of curvature instability, which notably gives rise to a crossover transition between an overdamped to an underdamped regime of the membrane and composition profiles. Furthermore, we use this model to study the effects of asymmetric membrane inclusions, the role of composition in channel gating, and lastly the deformations due to a protein coat.

3.3.1 Curvature Instability

Although the equilibrium solutions (derived in Section 3.2) were restricted to the parameter space given by $k_\pm^2 > 0$, as shown in Figure 3.3, the expressions of u and ϕ are still valid in the region where the coefficients $k_\pm^2$ are complex, namely when the coupling constant $\gamma \in \mathbb{I} := [\,|\alpha - \beta|,\, \alpha + \beta\,)$. The equation (3.12) can be used to derive that

$$k_\pm = \frac{1}{2}\left[\sqrt{(\alpha+\beta)^2 - \gamma^2} \pm \sqrt{(\alpha-\beta)^2 - \gamma^2}\right], \tag{3.58}$$

which shows that k_- and k_+ are complex conjugates of each other in $\mathbb{I}$. This guarantees that (3.13) and (3.15) are still real solutions within this parameter region.

In order to understand the physical significance of these complex terms, a specific model of a membrane inclusion is chosen. Here, we describe the rigid inclusion as a highly wedge-shaped protein, where the height $\mathcal{U}(\theta)$ and the contact angle $\mathcal{U}'(\theta)$ are taken to be some constants z_0 and δ_0, respectively. As described in Section 3.2, the value of z_0 is not entirely arbitrary, being set by the balance of normal forces on the membrane. On the other hand, δ_0 is chosen to be a typical angle found from crystal structures of integral membrane proteins that display a conical shape, such as the transmembrane domain of a voltage-dependent potassium channel [170], or, of a nicotinic acetylcholine receptor [171]. Hereinafter, a contact angle $\delta_0 = 15^\circ$ is used as the characteristic value of such membrane proteins.

Therefore, using these boundary conditions, the mid-plane of the bilayer $u(r)$ and the compositional asymmetry field $\phi(r)$ are found to be[‡]

$$u(r) = \frac{r_0\,\delta_0}{f_+ - f_-}\left[\frac{f_+\,K_0(k_- r)}{k_- r_0\,K_1(k_- r_0)} - \frac{f_-\,K_0(k_+ r)}{k_+ r_0\,K_1(k_+ r_0)}\right], \tag{3.59}$$

and

$$\phi(r) = r_0\,\delta_0\,\frac{f_+ f_-}{f_+ - f_-}\left[\frac{K_0(k_- r)}{k_- r_0\,K_1(k_- r_0)} - \frac{K_0(k_+ r)}{k_+ r_0\,K_1(k_+ r_0)}\right], \tag{3.60}$$

respectively. By approximating the modified Bessel functions by $K_n(\rho) \sim e^{-\rho}\sqrt{\frac{2}{\pi\rho}}$ for some $\rho \gg n$ [168], and by rewriting $k_\pm = Q \pm i\omega$, with

$$Q = \frac{1}{2}\sqrt{(\alpha+\beta)^2 - \gamma^2} \quad \text{and} \quad \omega = \frac{1}{2}\sqrt{\gamma^2 - (\alpha-\beta)^2}, \tag{3.61}$$

[‡]Notice that the tilt contributions (3.40) and (3.41), which guarantee the overall torque balance, are identically zero, which is due to the symmetry of the rigid inclusion.

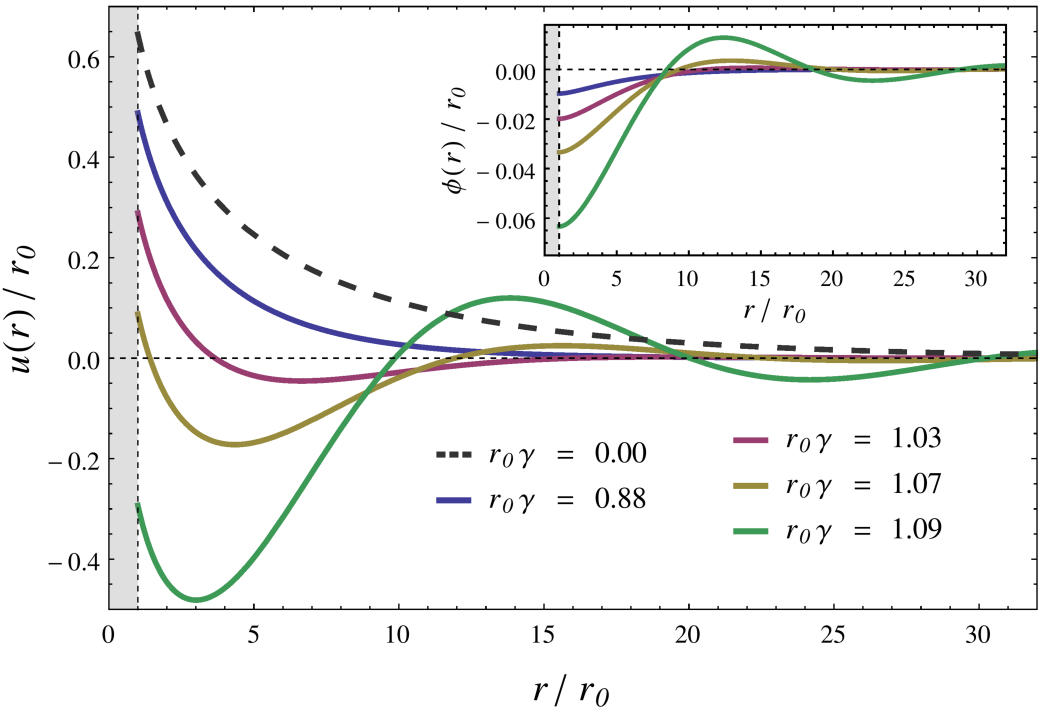

Figure 3.4: Radial profiles of the the mid-plane of the bilayer $u(r)$ and the compositional asymmetry $\phi(r)$ for several values of the coupling term γ, where $\alpha\, r_0 = 0.1$ and $\beta\, r_0 = 1.0$. The membrane deformation profiles are induced by a conical rigid inclusion of radius r_0 (depicted here as the grey region) and a small contact angle $\delta_0 = 15°$. For values of $\gamma > |\alpha - \beta|$ the both radial profiles display an underdamped behaviour.

then the asymptotic form of (3.59) and (3.60) when $\gamma \in \mathbb{I}$ can be written as

$$u(r) \simeq \frac{\gamma\, \mathfrak{C}_0\, e^{-Q(r-r_0)}}{\sqrt{r/r_0}} \cos\left[\,\omega\,(r - r_0) + \vartheta\,\right], \tag{3.62}$$

and

$$\phi(r) \simeq \frac{\alpha\, \mathfrak{C}_0\, e^{-Q(r-r_0)}}{\sqrt{r/r_0}} \cos\left[\,\omega\,(r - r_0) + \zeta\,\right], \tag{3.63}$$

respectively, with $\mathfrak{C}_0 = \frac{\delta_0}{2\,\omega\,Q}\sqrt{\alpha/\beta}$, and the phase angles ϑ and ζ are given by

$$\vartheta = \arctan\left[\frac{Q\left(\beta\,(\alpha-\beta)+\gamma^2\right)}{\omega\left(\beta\,(\alpha+\beta)-\gamma^2\right)}\right], \quad \text{and} \quad \zeta = \pi - \arctan\left(Q/\omega\right). \tag{3.64}$$

The radial profiles of (3.59) and (3.60) as function of the coupling term γ are shown in Figure 3.4. For values of γ less than $\gamma_d = |\alpha - \beta|$, the solutions

are found to be monotonically decreasing. However, as γ is increased above this value, the solutions show an underdamped behaviour, with the amplitude of the radial profile gradually decreasing to zero [162]. Moreover, the decay length of these amplitudes, namely $1/Q$, becomes very large as γ approaches $\gamma_c = \alpha + \beta$, which suggests the presence of an instability [162]. In fact, the parameter space restricted to $\gamma > \gamma_c$ corresponds to the region given by Leibler's criterion for curvature-induced instabilities in the bulk of membranes [163,164]. On the other hand, the point given by $\gamma = \gamma_d$ coincides to a critically damped system (that is, $\omega = 0$), where the profile of the membrane decays to zero as fast as possible without any undulations.

Although $\alpha = \sqrt{\sigma/\kappa}$ can be measured using various experimental techniques, as described in Section 2.3, the values of the phenomenological parameters β and γ are more elusive. However, by controlling the surface tension σ, the system can be tuned near the instability point $\sigma_c = \kappa\,(\gamma - \beta)^2$, where the amplitude of the membrane undulations are large and long-ranged. This suggests that the decay constant and frequency of these shape undulations may be experimentally accessible. Thus, if this may be the case, then the values of β and γ can be experimentally estimated by using the expressions of Q and ω in (3.61), with α as an independently determined variable, e.g. measured by a micropipette aspiration technique [111]. This illustrates the predictive power of our model, which allows us to estimate biological parameters that are otherwise hard to measure.

3.3.2 Asymmetric Membrane Inclusions

Using the methodology developed in Section 3.2, the lowest order estimates to the membrane configuration, its compositional asymmetry, and the total deformation energy can be found, given a model for the shape of the transmembrane protein, through $\mathcal{U}(\theta)$ and $\mathcal{U}'(\theta)$. These functions characterise the geometry of the protein inclusion, namely the surface of its hydrophobic transmembrane domain.

Here, for the sake of simplicity, but also to study the effect due to the asymmetries in the structure of a membrane inclusion, the height $\mathcal{U}(\theta)$ is chosen to be a constant, whereas the contact angle is given by

$$\mathcal{U}'(\theta) = \delta_0 \left[H\left(\theta - \zeta + \frac{w}{2}\right) - H\left(\theta - \zeta - \frac{w}{2}\right) \right]. \tag{3.65}$$

where the Heaviside function $H(x) = 1$ if $x \geq 0$ and vanishing otherwise. The parameter w measures the width of an angular interval centred around the phase angle $\theta = \zeta$, where the magnitude of the contact angle is non-zero and given by δ_0. This corresponds to a membrane protein that induces a local deformation only within

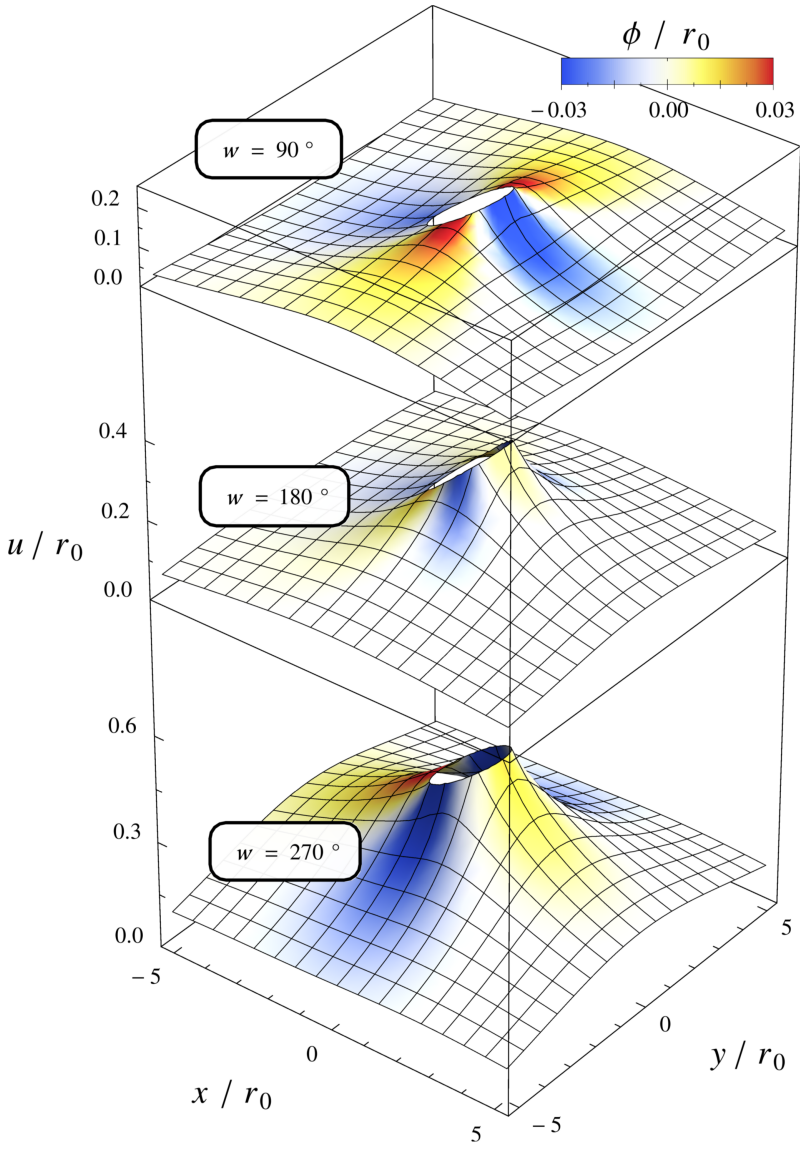

Figure 3.5: Membrane deformation profiles induced by an asymmetrical inclusion (e.g. LeuT). The surface heights represent the mid-plane of the bilayer for different values of the width w, which gives the asymmetry in the contact angle at the protein-membrane interface, namely $\mathcal{U}'(\theta) = \delta_0 \left[H\left(\theta - \zeta + w/2\right) - H\left(\theta - \zeta - w/2\right)\right]$, with $\zeta = 0$ and $\delta_0 = 15°$. Here, the parameters $\alpha\, r_0 = 0.1$, $\beta\, r_0 = 1.0$ and $\gamma\, r_0 = 0.5$, where r_0 is the radius of the membrane inclusion (which is depicted by the excluded region in these plots). Also, the compositional asymmetry field $\phi(r)$ is shown by the colour function of these surface plots. This displays a rich variability as the width w is varied between 0 and 2π, that is, the extreme points associated to an inclusion with a cylindrical and conical shape, respectively.

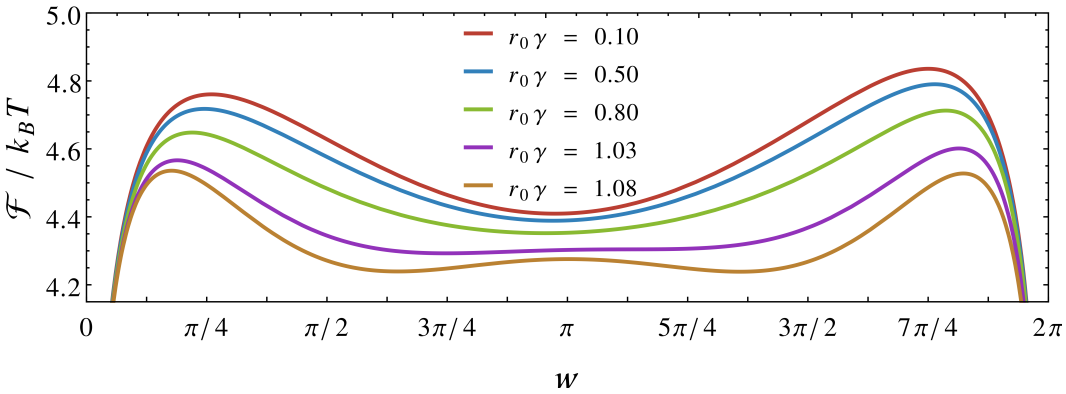

Figure 3.6: Total membrane deformation energy, for various values of the coupling term γ, against the width w, where the phase $\zeta = 0$ and the magnitude of the contact angle is set to be $\delta_0 = 15°$. Also, $\alpha\, r_0 = 0.1$ and $\beta\, r_0 = 1.0$, with r_0 as the radius of the inclusion, and the bending rigidity is chosen to be $\kappa = 20\ k_BT$.

a specific region along its hydrophobic surface, with the remaining part preferring a flat mid-plane. This is biologically of great relevance, e.g. the Connolly surface of a leucine transporter (LeuT) – a common protein model for human neurotransmitter transporters – exhibits such features [172, 173]. Therefore, the unknown boundary terms in (3.19) and (3.20) can be obtained by expressing (3.65) in its Fourier series, namely

$$\mathcal{U}'(\theta) = \frac{w\,\delta_0}{2\pi} + \sum_{n=1}^{\infty} \frac{2\,\delta_0}{n\pi} \sin\left(\frac{nw}{2}\right) \cos(n\theta - n\zeta). \tag{3.66}$$

For some fixed values of α, β, γ, and δ_0, this allows us to determine the membrane profile and its corresponding compositional asymmetry field as a function of w. A typical example is shown in Figure 3.5, where $\phi(r, \theta)$ is given by the colour-maps of the three-dimensional plots of $u(r, \theta)$. For $w < \pi$, the local compositional asymmetry is found to be negative within the non-zero range of the contact angle, whereas in the regions near the discontinuity jumps it is positive. However, as the width approaches $w = \pi$, the picture changes dramatically, with the compositional asymmetry field exhibiting a three-fold symmetry. For angular widths $w > \pi$, the field ϕ displays a similar pattern as in the case of $w < \pi$, but with its sign switched everywhere. Moreover, the magnitude of the induced deviations from flatness, u, is found to be increasing with w, as shown in Figure 3.5.

This methodology also allows us to compute the total energy (3.34), which vanishes for $w = 0$ and retrieves the case of conical inclusions when $w = 2\pi$ (if $\gamma = 0$ as well, then we recover the energy found in the previous works [146, 149, 159]). For intermediate values, the dependence of energy on w and γ is shown in Figure 3.6.

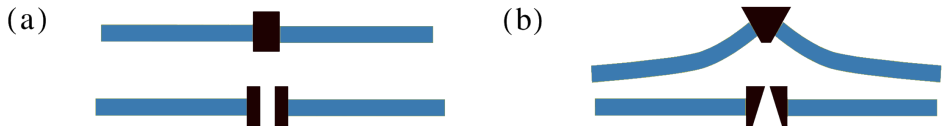

Figure 3.7: Diagrams of two idealised gating schemes for mechanosensitive channels, namely (a) the dilational gating model, and (b) the gating-by-tilt model. The bilayer is depicted here by the blue thick line. Under both schemes the tension does work by increasing the projected area of the membrane-channel system.

3.3.3 Mechanosensitive Membrane Channels

Mechanically-gated membrane channels are a widely examined class of transmembrane proteins, which provide a vital mechanism in living cells to withstand any rapid changes in the physical and chemical properties of their surrounding environment [4–6, 174]. Through protein conformational changes, from a closed state to an open state that allows the passage of solvent through the membrane, they can equilibrate an osmotic imbalance between the interior and exterior of the cell [4]. Although many examples of mechanosensitive channels are found in nature, the bacterial mechanosensitive channel of large conductance (MscL) and of small conductance (MscS) are typically used as the prototype of such proteins, for which various experimental studies have been performed, revealing their strong membrane tension dependence on the channel opening probability [174–179].

One simple mechanism proposes that the channel simply dilates at high tension giving rise to an open pore, as shown in Figure 3.7 (a). Another possibility is a gating-by-tilt mechanism [159], where the transition between the closed to open state is entirely driven by changes in slope at the protein-membrane interface (say, δ_0), as illustrated in Figure 3.7 (b).

In a two-component membrane, this couples to the lipid asymmetry field ϕ, which contributes to the change in the conformational energy of the channel-membrane system. Herein, the effect due to this mechanism is investigated by comparing the membrane deformation energy $\mathcal{F}$ (only the lowest order term $n = 0$ in the free-energy (3.34) is considered) to the experimentally measured energy for channel opening in the absence of tension, which is inferred by assuming a pore opening through the dilation mechanism [177, 178].

Interestingly, Figure 3.8 shows that the even small changes in the tilt angle at the channel-membrane interface can lead to a significant thermodynamic energy change under gating-by-tilt [162]. Furthermore, we find a regime in which the membrane can act to *close*, rather than open, the membrane channel, where the total energy $\mathcal{F}$ is negative and thus less than the conformational energy of the open state.

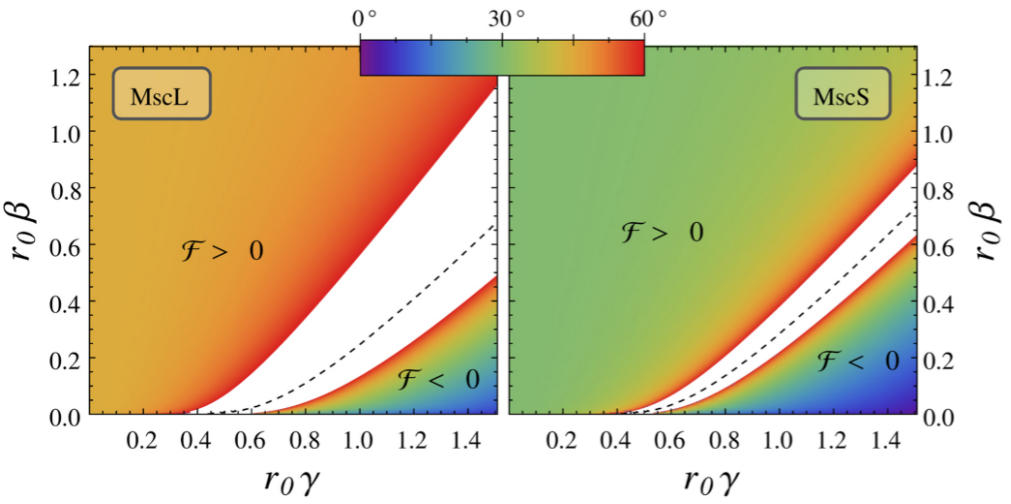

Figure 3.8: The estimated angle for the gating-by tilt that accounts for the total conformational energy change, say $\mathcal{F}$, as measured for MscL and MscS [177,178]. The dashed line represents $\mathcal{F} = 0$ dividing the phase space into two domains where the membrane acts to open ($\mathcal{F} > 0$), or close ($\mathcal{F} < 0$), the channel. The uncoloured region corresponds to angles greater than 60°, which are likely unphysical and where our small-angle approximation is therefore inadequate.

As a result, this reveals that local composition variation, and its coupling to membrane curvature, might have an important role in modulating the function of mechanosensitive channels, in particular, the MscS and MscL proteins.

3.3.4 Protein Coat Deformations

Another interesting application of our model is the study of protein coat formation in its early stages [160]. Such protein coats play an important role in the regulation of biomembranes (e.g. membrane trafficking using clathrin coats), or in cell infection, where viral coats assemble at the plasma membrane [1].

Herein, a protein coat is described as a spherical rigid object that adheres to the lipid bilayer, inducing membrane deformations (see Figure 3.9). The membrane shape on which the protein coat adheres is assumed to be commensurate with the conformation of the coat, which has a constant intrinsic curvature $1/\mathcal{R}_c$. In the early stages of growth, the formation of this spherical cap (say, of radius r_0) only weakly perturbs the membrane outside the coat, with a contact angle given by $\delta_0 \approx r_0/\mathcal{R}_c$.

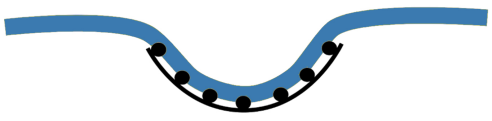

Figure 3.9: Sketch of a biomembrane (the blue thick line) deformed by the assembly of a protein coat.

Consequently, the outer membrane can be described using the methodology developed in Section 3.2, where the membrane region that covers the protein coat acts as a cone-shaped rigid inclusion (denoted here by $\mathcal{M}_{\rm c}$). However, the local compositional asymmetry is no longer free at the boundary, and consequently the Dirichlet condition is enforced instead, namely $\phi(r_0) = \varphi_0$. Thus, the outer membrane profile $u(\mathbf{r})$ and its associated local compositional field $\phi(\mathbf{r})$ are found to be

$$u(r) = r_0\,\delta_0\left[\frac{f_+\mathcal{L}_0^+ K_0(k_- r)}{\mathcal{P}_0\,K_0(k_- r_0)} - \frac{f_-\mathcal{L}_0^- K_0(k_+ r)}{\mathcal{P}_0\,K_0(k_+ r_0)}\right] - \varphi_0\left[\frac{\mathcal{L}_0^+ K_0(k_- r)}{\mathcal{P}_0\,K_0(k_- r_0)} - \frac{\mathcal{L}_0^- K_0(k_+ r)}{\mathcal{P}_0\,K_0(k_+ r_0)}\right], \tag{3.67}$$

and

$$\phi(r) = r_0\,\delta_0\left[\frac{f_-f_+\mathcal{L}_0^+ K_0(k_- r)}{\mathcal{P}_0\,K_0(k_- r_0)} - \frac{f_-f_+\mathcal{L}_0^- K_0(k_+ r)}{\mathcal{P}_0\,K_0(k_+ r_0)}\right] - \varphi_0\left[\frac{f_-\mathcal{L}_0^+ K_0(k_- r)}{\mathcal{P}_0\,K_0(k_- r_0)} - \frac{f_+\mathcal{L}_0^- K_0(k_+ r)}{\mathcal{P}_0\,K_0(k_+ r_0)}\right], \tag{3.68}$$

respectively, where the radial distance $r \geq r_0$. However, φ_0 is not arbitrary, being set by the value which minimises the total membrane energy inside and outside of the protein coat. The deformation energy of the outer membrane can be derived through (3.52), namely

$$\hat{\mathcal{F}}_{\rm out} = \frac{\alpha^2\left[(f_+ - f_-)\,r_0^2\,\delta_0^2 - 2\,\varphi_0\left(\mathcal{L}_0^+ - \mathcal{L}_0^-\right)r_0\,\delta_0\right] - \mathcal{L}_0^-\mathcal{L}_0^+\left(k_+^2 - k_-^2\right)\varphi_0^2}{f_+\mathcal{L}_0^- - f_-\mathcal{L}_0^+}. \tag{3.69}$$

Analogous to equation (3.3), the nondimensionalised free-energy functional of the membrane within the region $\mathcal{M}_{\rm c}$ can be written as [162]:

$$\hat{\mathcal{F}}_{\rm in} = 4\,(1-\cos\delta_0) + \alpha^2\,\mathcal{R}_{\rm c}^2\,(1-\cos\delta_0)^2 + \frac{\gamma^2}{2\pi}\int_{\mathcal{M}_{\rm c}}\left(\beta^2\phi^2 + (\nabla\phi)^2 + \frac{4\,\phi}{\mathcal{R}_{\rm c}}\right), \tag{3.70}$$

where the first and second term represent the free-energy associated to bending and stretching the membrane from a flat state to a spherical cap shape. This functional admits the following Euler-Lagrange equation:

$$\left(\nabla^2 - \beta^2\right)\phi - 2/\mathcal{R}_{\rm c} = 0. \tag{3.71}$$

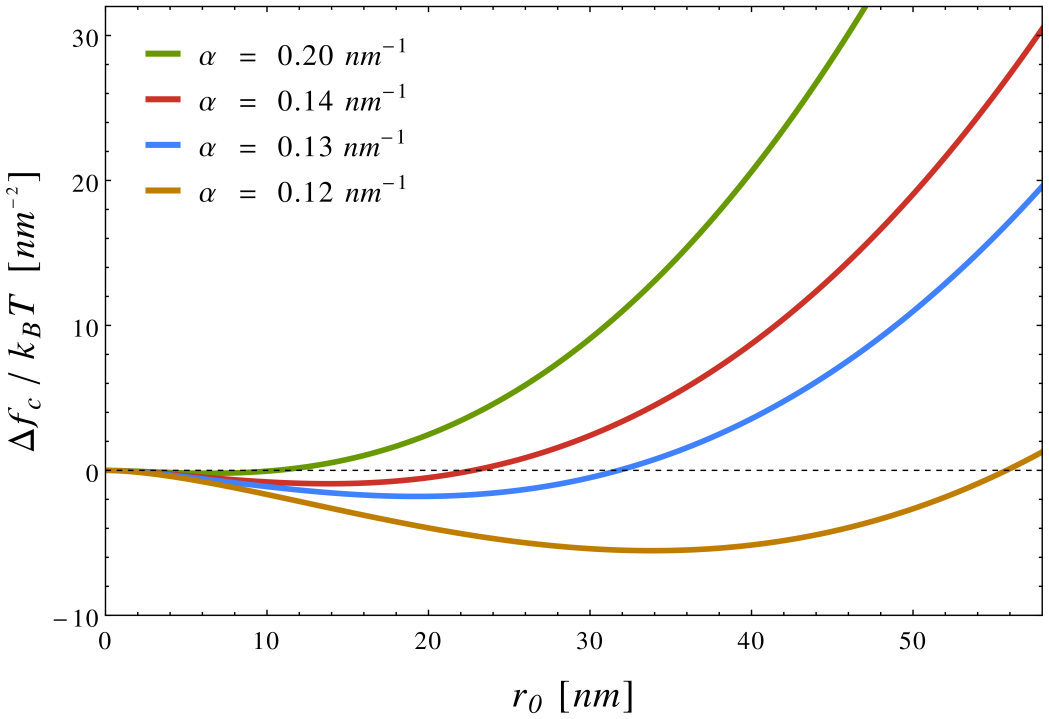

Figure 3.10: The free-energy per unit area of coat monomers $\Delta f_{\rm c}$ (that is purely due to the curvature coupling to the compositional variations) as a function of the radius of the projected coat area, r_0, and various values of α in the underdamped regime. The intrinsic curvature radius of the protein coat is chosen to be $\mathcal{R}_{\rm c} = 50$ nm, and the parameters $\beta = 1.0$ nm^{-1} and $\gamma = 1.1$ nm^{-1}. The energy $\Delta f_{\rm c}$ displays an initial decrease and a local minimum as r_0 is varied.

By assuming that the local compositional field ϕ remains finite everywhere in $\mathcal{M}_{\rm c}$ and using the same Dirichlet boundary condition, $\phi(r_0) = \varphi_0$, (3.71) yields

$$\phi(r) = -\frac{2}{\beta^2 \mathcal{R}_{\rm c}} + \left(\varphi_0 + \frac{2}{\beta^2 \mathcal{R}_{\rm c}}\right) \frac{I_0(\beta\, r)}{I_0(\beta\, r_0)}, \tag{3.72}$$

where $r \leq r_0$ and I_0 is the modified Bessel function of the first kind of order zero. As a result, the energy (3.70) to lowest order in δ_0 becomes

$$\hat{\mathcal{F}}_{\rm in} = 2\,\delta_0^2 \left(1 - \frac{\gamma^2}{\beta^2}\right) + \frac{r_0\, \gamma^2 \left(2 + \varphi_0\, \beta^2\, \mathcal{R}_{\rm c}\right)^2 I_1(\beta\, r_0)}{\beta^3\, \mathcal{R}_{\rm c}^2\, I_0(\beta\, r_0)}, \tag{3.73}$$

where I_1 is the first order modified Bessel function of the first kind. Hence, φ_0 can be determined by minimising the total deformation energy $\hat{\mathcal{F}}_{\rm total} = \hat{\mathcal{F}}_{\rm in} + \hat{\mathcal{F}}_{\rm out}$,

which gives that

$$\varphi_0 = r_0\,\delta_0 \frac{f_- f_+ \left(\mathcal{L}_0^+ - \mathcal{L}_0^-\right)\beta\, r_0\, I_0\left(\beta\, r_0\right) + 2\left(f_- \mathcal{L}_0^+ - f_+ \mathcal{L}_0^-\right) I_1\left(\beta\, r_0\right)}{\beta\, r_0\left[\mathcal{L}_0^- \mathcal{L}_0^+ (f_+ - f_-) I_0\left(\beta\, r_0\right) + \left(f_+ \mathcal{L}_0^- - f_- \mathcal{L}_0^+\right)\beta\, r_0\, I_1\left(\beta\, r_0\right)\right]}, \quad (3.74)$$

where $r_0 = \delta_0 \mathcal{R}_\mathrm{c}$ is used to simplify the expression. This allows us to compute the total deformation energy $\hat{\mathcal{F}}_\mathrm{total}$ due to a protein coat in its early stages of growth as a function of the inclusion radius r_0. Furthermore, the membrane energy change due to coupling to ϕ alone, and scaled by the projected coat area, namely

$$\Delta f_\mathrm{c} = \frac{1}{\pi r_0^2}\left(\hat{\mathcal{F}}_\mathrm{total} - \lim_{\gamma \to 0} \hat{\mathcal{F}}_\mathrm{total}\right), \quad (3.75)$$

can be computed to second order in the angle δ_0 (by carefully noting that r_0 and δ_0 are not independent variables). This energy-per-area renormalises the chemical potential for binding of early coat monomers to the membrane and yields a measure of the energy landscape purely induced by ϕ and its coupling to the membrane curvature. Figure 3.10 shows the variation of Δf_c with the coat radius r_0, which displays an initial energetic decrease with r_0 in the underdamped regime. This suggests that the deformation of the membrane (with its corresponding compositional variation) is energetically favourable in that case. As a result, this can be used as a mechanism for controlling, or driving, coat formation in biomembranes [162].

3.4 Summary

An analytic model based on the Canham–Helfrich theory is presented in Section 3.2, which describes the response of a fluid membrane to the insertion of a single rigid inclusion, when the mean curvature of the membrane is phenomenologically coupled to its local compositional variations. The ground state solutions to the membrane profile and its corresponding compositional asymmetry are derived in the Monge representation, and their associated deformation energy is determined. In Section 3.3, we show how the model can be used to calculate properties of biological relevance, such as the membrane shape and its composition near a protein of non-trivial structure, and the regulation of channel gating by protein tilt or composition asymmetry. A particularly interesting finding is the possibility to promote protein coat formation towards budding by compositional variations. Moreover, when the curvature-composition coupling is strong enough, the membrane undergoes a transition from an overdamped to an underdamped regime, which can be used to estimate the free phenomenological parameters in our model, illustrating its predictive power.

Chapter 4

Optical Projection of Thermal Shape Fluctuations

The optical spectroscopy of thermally induced shape fluctuations of vesicles has been widely used as a method to extract mechanical information about fluid membranes, particularly yielding an estimate of the bending modulus [97–106]. As discussed in Section 2.3.2, this method is commonly known as flicker spectroscopy, and involves a comparison of the experimental data to the predicted statistics of the thermal shape undulations [70]. The appropriate language to discuss the latter is the subject of statistical field theory [180], which typically requires a calculation of the partition function $\mathcal{Z}$ over all possible configurations of the membrane geometry. However, $\mathcal{Z}$ is highly non-trivial to compute in general, and it is usually evaluated by restricting to quadratic fluctuations about the equilibrium state of the fluid membrane [14]. This framework is used to describe the statistics of the shape undulations of giant unilamellar vesicles (GUVs) induced by thermal agitation.

4.1 Introduction

In this section, we review the theoretical framework discussed above, which allows us to determine the fluctuation spectrum of vesicle shape undulations. By using the latter, the elastic constants of fluid membranes can be estimated if this spectrum is compared with experimental data. Subsequently, we discuss some of the limitations encountered in this methodology and also how they may affect the inferred measurements of the bending modulus. In particular, we emphasise that optical microscopy of GUVs can only provide partial information in the sense that it only gives a two-dimensional projection of a three-dimensional fluctuating surface. As a result, the

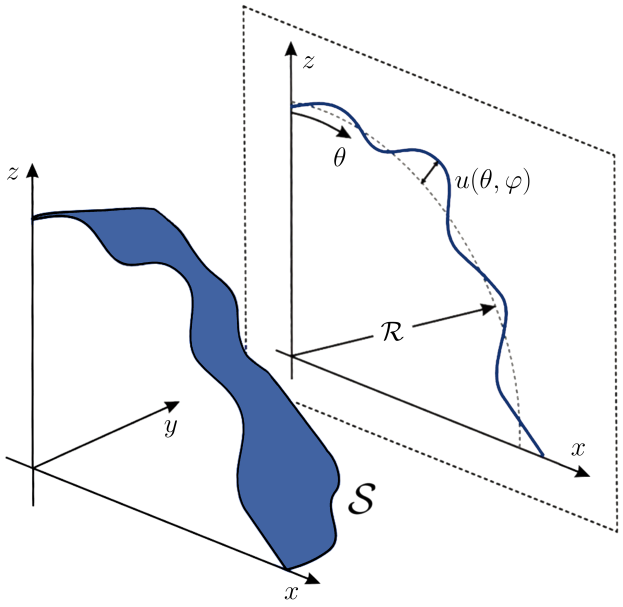

Figure 4.1: Schematic diagram of a three-dimensional membrane patch of a quasi-spherical lipid vesicle (depicted here by the blue region), and a two-dimensional cross-section along the xz-plane. The latter illustrates the shape fluctuations of the vesicle about a fixed radius $\mathcal{R}$, which are given by $u(\theta, \varphi)$, with $\varphi = 0$ in this case.

experimental data has typically been compared to the predicted statistics on the intersection of the vesicle with the focal plane of the microscope, ignoring the effect due to fluctuations out of this plane. Later in this chapter (see Section 4.2), we develop an analytical model that includes the projection of shape fluctuations within the focal depth of the microscope. Moreover, the consequences of this theoretical amendment is studied against experimental data* in Section 4.3, and the results of the analysis suggest that the current methodology used in flicker spectroscopy experiments may overestimate the value of the bending modulus by a significant factor. The results are now found to be in good agreement with the values obtained through other techniques, such as X-ray scattering and micromechanical manipulation methods, which have previously been estimated to be systematically larger [67].

4.1.1 Thermal Undulations of Quasi-spherical Vesicles

The usual theoretical description of GUVs is treated within a quasi-spherical approximation, where the membrane surface, say $\mathcal{S}$, is parametrised by the spherical

*The experimental data (unpublished) has been provided by our experimental collaborators, Dr. Pietro Cicuta, from the University of Cambridge, and Dr. Davide Orsi, from the University of Parma. See Section 4.3 for more details.

angular coordinates (θ, φ), with the surface positional vector given by

$$\mathbf{R}\,(\theta, \varphi) = \mathcal{R}\,[1 + u(\theta, \varphi)]\,\mathbf{e}_r(\theta, \varphi)\,, \tag{4.1}$$

where $u(\theta, \varphi)$ is a local deviation about a reference sphere of radius $\mathcal{R}$ in a Monge-type representation (as shown Figure 4.1), and $\mathbf{e}_r(\theta, \varphi)$ is the radial unit vector normal to this sphere. The volume V_0 enclosed by the membrane of GUVs is considered to be constant, which in turn defines the radius $\mathcal{R} := (3V_0/4\pi)^{1/3}$. Furthermore, the fluctuations about the reference sphere are assumed to be small and slowly varying (that is, the magnitude $|u(\theta, \varphi)| \ll 1$ and the gradient $|\nabla u(\theta, \varphi)| \ll 1$), so that the free-energy in the Canham–Helfrinch theory (2.27) can be written as a quadratic expansion in $u(\theta, \varphi)$. To obtain this expansion, we follow the works of [97] and [108], where the area of the vesicle $\mathcal{A} := \int_{\mathcal{S}} \mathrm{d}S$, its volume $V := \frac{1}{3}\int_{\mathcal{S}} \mathrm{d}S\ (\mathbf{n} \cdot \mathbf{R})$, with $\mathbf{n}$ as its surface normal, the integrated mean-curvature term $\mathcal{Q}_1 := \int_{\mathcal{S}} \mathrm{d}S\, H$, and also the bending term $\mathcal{Q}_2 := \int_{\mathcal{S}} \mathrm{d}S\, H^2$ can be approximated by a second-order Taylor expansion in u as follows:

$$\mathcal{A} = 4\pi\mathcal{R}^2 + \mathcal{R}^2 \int_0^{\pi}\int_0^{2\pi} \left[2\,u + u^2 + \frac{1}{2}\,(\nabla u)^2\right] \sin(\theta)\,\mathrm{d}\theta\,\mathrm{d}\varphi, \tag{4.2}$$

$$V = V_0 + \mathcal{R}^3 \int_0^{\pi}\int_0^{2\pi} \left(u + u^2\right) \sin(\theta)\,\mathrm{d}\theta\,\mathrm{d}\varphi, \tag{4.3}$$

$$\mathcal{Q}_1 = 4\pi\mathcal{R} + \mathcal{R} \int_0^{\pi}\int_0^{2\pi} \left[u + \frac{1}{2}\,(\nabla u)^2 - \frac{1}{2}\left(\nabla^2 u\right)\right] \sin(\theta)\,\mathrm{d}\theta\,\mathrm{d}\varphi, \tag{4.4}$$

and

$$\mathcal{Q}_2 = 4\pi + \int_0^{\pi}\int_0^{2\pi} \left[u\left(\nabla^2 u\right) - \left(\nabla^2 u\right) + \frac{1}{2}\,(\nabla u)^2 + \frac{1}{4}\left(\nabla^2 u\right)^2\right] \sin(\theta)\,\mathrm{d}\theta\,\mathrm{d}\varphi, \tag{4.5}$$

respectively, where the differential operators ∇ and ∇^2 are defined with respect to the metric of a unit sphere [49], that is,

$$\nabla := \mathbf{e}_\theta \frac{\partial}{\partial\theta} + \frac{\mathbf{e}_\varphi}{\sin(\theta)} \frac{\partial}{\partial\varphi}, \quad \text{and} \quad \nabla^2 := \frac{1}{\sin(\theta)} \frac{\partial}{\partial\varphi}\left[\sin(\theta) \frac{\partial}{\partial\varphi}\right] + \frac{1}{\sin^2(\theta)} \frac{\partial^2}{\partial\varphi^2}, \tag{4.6}$$

with $\mathbf{e}_\theta$ and $\mathbf{e}_\varphi$ as the unit vectors associated to the spherical angular coordinates.

Therefore, by ignoring the Gaussian curvature term in (2.25) due to the constrained topology of GUVs, the effective free-energy of the fluid membrane $\mathcal{S}$ is given by $\mathcal{F} = \mathcal{C}_0\,\mathcal{A} + \mathcal{C}_1\,\mathcal{Q}_1 + \mathcal{C}_2\,\mathcal{Q}_2$, where $\mathcal{C}_0$, $\mathcal{C}_1$, and $\mathcal{C}_2$ are defined in (2.26). Also,

by expressing $u(\theta, \varphi)$ in the basis of spherical harmonics Y_n^m [168], namely

$$u(\theta, \varphi) = \sum_{n=0}^{n_\infty} \sum_{m=-n}^{n} \mathcal{U}_{n,m} Y_n^m(\theta, \varphi), \tag{4.7}$$

where $\mathcal{U}_{n,m}$ is the amplitude associated to each spherical harmonic mode (n, m), with n_∞ as an ultraviolet cutoff[†], then the effective free-energy $\mathcal{F}$ can be written in the following diagonalised form (a full derivation can be found in [108]):

$$\mathcal{F} = 4\pi\kappa\,(2 + \bar{\sigma}) + \frac{1}{2} \sum_{n=2}^{n_\infty} H(n) \sum_{m=-n}^{n} |\mathcal{U}_{n,m}|^2, \tag{4.8}$$

where $|\mathcal{U}_{n,m}|$ is the complex modulus of the harmonic amplitude $\mathcal{U}_{n,m}$, the function $H(n)$ is defined by

$$H(n) = \kappa\,(n-1)(n+2)\,[\,\bar{\sigma} + n(n+1)\,], \tag{4.9}$$

and $\bar{\sigma}$ is the reduced surface tension, namely

$$\bar{\sigma} = \frac{\sigma \mathcal{R}^2}{\kappa} - 2\,H_0 \mathcal{R} + 2\,H_0^2 \mathcal{R}^2. \tag{4.10}$$

The zeroth order coefficient $\mathcal{U}_{0,0}$ in equation (4.7) can be fixed by employing the constraint that the volume V of the GUVs remains unchanged under a small local deformation $u(\theta, \varphi)$, that is, $V = V_0$ in (4.3). This implies the following condition:

$$\mathcal{U}_0^0 = -\frac{1}{\sqrt{4\pi}} \sum_{n=0}^{n_\infty} \sum_{m=-n}^{n} |\mathcal{U}_{n,m}|^2\,, \tag{4.11}$$

which essentially corresponds to a rescaling of the frame radius [97]. Thus, its contribution to the free-energy (4.8) can be omitted without loss of generality. It is noteworthy to mention that the three spherical harmonic modes given by $n = 1$ do not affect the area $\mathcal{A}$ and the effective free-energy $\mathcal{F}$, as they correspond to pure translations of the vesicle, which incur no energetic cost since $H(n = 1) = 0$. As a result, the summation in equation (4.8) can be restricted solely to modes $n \geq 2$ [108].

By introducing a fictitious external field in the effective free-energy (4.8), as a *vector* $\mathbf{J} := \{\mathcal{J}_{n,m}\}$, that linearly couples to the amplitude vector $\mathbf{U} := \{\mathcal{U}_{n,m}\}$, where the integers $n \geq 2$ and $|m| \leq n$, then equation (4.8) can be concisely rewritten

[†]The upper mode cutoff $n_\infty \simeq \mathcal{R}/\xi$, where ξ is on the order of the membrane thickness. Thus, using a typical radius of GUVs, say $\mathcal{R} \sim 25$ μm, and a value of $\xi \sim 5$ nm, then $n_\infty \sim 5 \times 10^3$.

in terms of the following functional form:

$$\mathcal{F}\,[\mathbf{J},\mathbf{U}] = 4\pi\kappa\,(2+\bar{\sigma}) + \frac{1}{2}\,\mathbf{U}^{\mathsf{T}}\mathbf{H}\,\mathbf{U}^{*} - \mathbf{J}^{\mathsf{T}}\mathbf{U}, \tag{4.12}$$

where $\mathbf{H}$ is a diagonal *matrix* whose components are given by $H(n)$, and the symbols $*$ and T denote a complex conjugate and a transpose, respectively. As a consequence, the thermodynamic properties of the model can be obtained from the partition function [180]:

$$\mathcal{Z}[\mathbf{J}] = \int \mathcal{D}\mathbf{U}\,\exp\left(-\frac{\mathcal{F}\,[\mathbf{J},\mathbf{U}]}{k_B T}\right), \tag{4.13}$$

where the integration measure $\mathcal{D}\mathbf{U} := \prod_{n=2}^{n_\infty}\{\prod_{m=0}^{n}\mathrm{d}\,\Re[\mathcal{U}_{n,m}]\}\{\prod_{m=1}^{n}\mathrm{d}\,\Im[\mathcal{U}_{n,m}]\}$, with $\Re\,[\mathcal{U}_{n,m}]$ and $\Im\,[\mathcal{U}_{n,m}]$ being the real and imaginary parts of $\mathcal{U}_{n,m}$.

Due to the quadratic nature of (4.12), the partition function in (4.13) can be analytically computed, up to an unimportant prefactor, as follows [14, 180]:

$$\mathcal{Z}[\mathbf{J}] \propto \exp\left(\frac{\mathbf{J}^{\mathsf{T}}\mathbf{H}^{-1}\mathbf{J}^{*}}{2\,k_B T}\right), \tag{4.14}$$

where $\mathbf{H}^{-1}$ is the inverse matrix of $\mathbf{H}$. Hence, the thermodynamic average of the flickering amplitudes $\mathcal{U}_{n,m}$ and their correlation functions can be determined by using the derivatives of $\ln\mathcal{Z}$ with respect to the fictitious external fields $\mathcal{J}_{n,m}$ [180], namely

$$\langle\,\mathcal{U}_{n,m}\rangle = \frac{\partial}{\partial\mathcal{J}_{n,m}}\Big(k_B T\ln\mathcal{Z}[\mathbf{J}]\Big)\bigg|_{\mathbf{J}\,=\,0} = 0 \tag{4.15}$$

and

$$\big\langle\,\mathcal{U}_{n,m}\,\mathcal{U}^{*}_{k,\ell}\big\rangle = \frac{\partial^2}{\partial\mathcal{J}_{n,m}\,\partial\mathcal{J}^{*}_{k,\ell}}\Big(k_B T\ln\mathcal{Z}[\mathbf{J}]\Big)\bigg|_{\mathbf{J}\,=\,0} = \frac{k_B T}{H(n)}\,\delta_{nk}\,\delta_{m\ell}, \tag{4.16}$$

where δ_{nm} is the Kronecker delta function, which equals one if $n = m$ and vanishing otherwise. Hence, the equation (4.16) shows that the harmonic amplitudes are completely uncorrelated if the spherical modes $n \neq k$, and the mean-squared deviations $\big\langle\,|\mathcal{U}_{n,m}|^2\big\rangle$ are independent of m and also a function of the membrane elastic constants, i.e. the bending modulus κ and the reduced surface tension $\bar{\sigma}$. Thus, they can be experimentally measured if the local variations in the three-dimensional shape of the GUVs can be observed and recorded over a sufficiently long time span.

4.1.2 Comparing the Model to Experiments

A lipid vesicle observed using light microscopy yields only a two-dimensional projection of its membrane onto the focal plane of the microscope. As a result, the contact between the experimentally measured contours (which are determined by an edge-detection algorithm, as discussed in [103], where the membrane position is usually assigned to be the extremum of the observed intensity profile) and the three-dimensional model of the membrane surface, as given by (4.16), has typically been established by focussing on the two-dimensional contours obtained through the intersection of the vesicle with the focal plane of the objective.

This cross-sectional plane is usually chosen to be at the equator of the lipid vesicle ($\theta = \pi/2$), where the diameter of the contours is found to be the largest, and also where the contrast is typically maximal[‡]. Thus, the radial position of the membrane in the equatorial plane of the vesicle, $\rho_0(\varphi, t) := \|\mathbf{R}(\theta = \pi/2,\, \varphi,\, t)\|$, can be used as an experimental observable, which has now an explicit time t dependence. The time-average of the squared deviations in $\rho_0(\varphi, t)$ about the mean radius $\mathcal{R}$ can be related to (4.16) by assuming the ergodic hypothesis (namely, a long time-average of a macroscopic variable is equivalent to its thermal average [180]). In other words, the Fourier transform of the variations in $\rho_0(\varphi, t)$ about its mean value, that is,

$$u_q(t) := \frac{1}{2\pi} \int_{-\pi}^{+\pi} \mathrm{d}\varphi \; e^{-iq\varphi} \; u\Big(\theta = \frac{\pi}{2},\, \varphi\Big), \tag{4.17}$$

which is non-dimensionalised by $\mathcal{R}$, can be used to obtain a fluctuation spectrum in terms of the integer Fourier modes q, which is defined by the following autocorrelation function:

$$\big\langle u_q(t)\, u_q^*(t) \big\rangle_t = \sum_{n \geq q} \mathcal{E}_{n,q}^2 \, \big\langle \, |\mathcal{U}_{n,q}|^2 \, \big\rangle, \tag{4.18}$$

where the coefficients $\mathcal{E}_{n,q} = Y_n^q \, (\theta = \pi/2,\, \varphi = 0)$, and $\langle \cdot \rangle_t$ denotes a time-average over the total duration of the experiment (which is identical to the thermal average as the system is ergodic). The result in (4.18) can be derived by employing the equations (4.7) and (4.16), together with the orthogonality of the spherical harmonic

[‡]In the case of lipid vesicles which enclose a fluid that has the same density as the bulk solvent, the maximum contrast and the largest diameter of the contours are indeed found at $\theta = \pi/2$. However, the interior fluid is typically of a different density to ensure sedimentation of the vesicles to a substrate. In this case, the shape of vesicles is perturbed due to gravitational effects [181], which means that the position of the plane with the maximum diameter is no longer located at the equator of GUVs. However, such gravity effects are negligible if $\Delta\rho\, g\, \mathcal{R}^4 \lesssim \kappa\,(12 + \bar{\sigma})$, as calculated in [181], where $g = 9.81$ m/s^2 and $\Delta\rho$ is the density difference between the inside and the outside of the vesicle. Typically, this condition is readily satisfied in flicker spectroscopy experiments [103] and thus the gravitational effects are ignored throughout this study.

functions Y_n^m, and the summation identity $\sum_{k=0}^{\infty}\sum_{k=-\ell}^{+\ell}\mathcal{B}_{k,\ell}=\sum_{\ell=-\infty}^{\infty}\sum_{k=\ell}^{\infty}\mathcal{B}_{k,\ell}$.

Another experimental issue, which further complicates the comparison of the experimental data with the fluctuation spectrum (4.18), is that the observed two-dimensional contours are, in practice, averaged over the integration time τ of the camera [99]. This introduces an experimental limitation that results in significant averaging effects of the shape fluctuations when their characteristic life-times are shorter than the acquisition time of the camera. Hence, its consequences on the fluctuation spectrum have been widely studied [103]. To quantitatively account for this averaging, the relaxation times $\tau_{n,m}$ associated to each spherical harmonic mode needs to be adequately determined. By using a simple viscoelastic theory of a spherical vesicle, as derived in [108], we find that $\mathcal{U}_{n,m}(t)=\mathcal{U}_{n,m}(0)\,e^{-t/\tau_{n,m}}$, where the mono-exponential decay time of each mode are found to be

$$\tau_{n,m}=\frac{\mathcal{R}^3}{H(n)}\left[\eta_{\text{in}}\,\frac{(n+2)(2n-1)}{n+1}+\eta_{\text{out}}\,\frac{(n-1)(2n+3)}{n}\right], \tag{4.19}$$

with η_{in} and η_{out} as the viscosities of the surrounding fluid found in the inside and the outside of the vesicle, respectively. As a result, due to the finite acquisition time τ of the camera (which is usually on the order of microseconds), the time correlation function of the equatorial fluctuations in (4.18) becomes [108]:

$$\left\langle \bar{u}_q(t)\,\bar{u}_q^*(t)\right\rangle_t=\sum_{n\,\geq\,q}\mathcal{E}_{n,q}^2\left\langle\,|\mathcal{U}_{n,q}|^2\,\right\rangle\frac{\tau_{n,q}^2}{\tau^2}\left(1-e^{-\tau/\tau_{n,q}}\right)^2, \tag{4.20}$$

where we define $\bar{u}_q(t):=\tau^{-1}\int_0^\tau \mathrm{d}t'\;u_q(t+t')$. Thus, the methodology involves relating (4.20) to the spectrum computed from the experimentally observed contours[§], which allows us to estimate the membrane bending modulus and its surface tension.

Although this approach of projecting the fluctuations onto the equatorial plane may appear to be a reasonable approximation, we maintain that the equatorial plane of the GUVs is not what is actually observed under an optical microscope. Strictly speaking, the equator of the vesicle contains a vanishing area in projection, and it is therefore invisible to the usual video-microscopy techniques. Thus, we assume that what is observed is a projection over a strip of membrane material within a small region in the vicinity of the equator, as shown in Figure 4.2. This

[§]The fluctuation spectrum of a flat membrane patch is numerically found to be very close to the spectrum given by (4.20) for high q modes [103]. As a result, the planar spectrum in (2.37) is usually preferred for its simplicity and it is used instead of (4.20) by discarding a few of the lower modes and also including the average over the acquisition time. This excellent agreement for higher q modes suggests that the statistics of membrane fluctuations are not affected by the radius of curvature of the vesicle if their wavelengths are much shorter than length scale of the system.

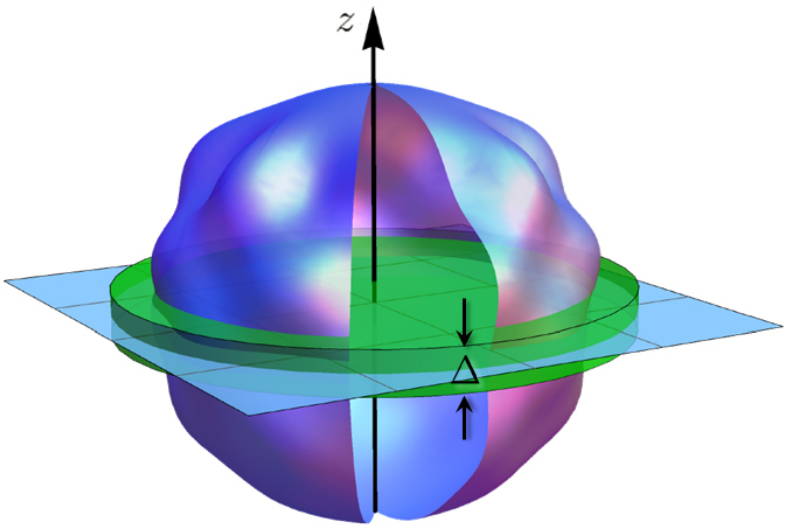

Figure 4.2: Schematic diagram of a fluctuating vesicle, where the light-blue plane illustrates the focal plane of the microscope, whilst the green slab depicts the region within the focal depth Δ of the objective, where the surface modes of the vesicle are averaged out in projection.

strip can support a spectrum of surface modes, which are averaged out in projection. As a consequence, this effect may be expected to be particularly strong when the focal depth of the microscope is much larger than the membrane correlation length $\lambda = \sqrt{\kappa/\sigma}$, namely

$$\Delta \gtrsim \frac{\lambda}{\mathcal{R}} = \frac{1}{\sqrt{\bar{\sigma}}}, \tag{4.21}$$

where Δ is the ratio of the focal depth to $\mathcal{R}$, and the final equality holds if the mean spontaneous curvature $H_0 = 0$ in the equation (4.10). On a heuristic level, the criterion (4.21) is justified by the fact that one is then measuring an average over a strip of many correlation lengths in size and thus one would expect a reduced average membrane displacement as a result. Also, the characteristic values of Δ are found to be between $0.01 - 0.2$ in the flicker spectroscopy experiments, which are comparable to the typical values of $\lambda/\mathcal{R}$. Thus, the estimation of the parameters κ and $\bar{\sigma}$ is expected to be notably sensitive to this projection, since a large number of fluctuation modes are averaged out within the focal depth of the microscope.

4.2 Projection of Surface Fluctuations

In order to examine the effect due to the projection of the shape undulations onto the focal plane of the microscope, we need to understand how the averaging of

fluctuations out of this plane affects the light intensity entering the camera. However, since the latter usually depends on the specific imaging technique used in the experiments and various other optical considerations, the full analysis is a highly non-trivial task. Thus, in this section, we introduce an approach, which allows us to construct an intensity field that mimics closely some of the features of its experimental counterpart.

4.2.1 Intensity of Quasi-spherical Vesicles

Firstly, we consider that light arriving from a point on the membrane surface that is located at a height z above, or below, the focal plane (or equivalently, the equatorial plane of the vesicle, as discussed in Section 4.1.2) has an intensity which is scaled by a Gaussian kernel $\mathcal{G}(z)$, namely

$$\mathcal{G}(z) = \exp\left[-\frac{1}{2\Delta^2}\left(\frac{z}{\mathcal{R}}\right)^2\right], \tag{4.22}$$

where $\mathcal{R}$ is the mean radius of the vesicle, and Δ is a dimensionless parameter that characterises the focal depth of the microscope, as shown in Figure 4.2.

Secondly, we assume that the vesicle radiates light isotropically (e.g. its membrane is uniformly fluorescent), and furthermore there is no refraction or absorption, which implies that the infinitesimal radiant power $\mathrm{d}\mathfrak{A}$ emanated by a small membrane patch $\mathrm{d}\mathcal{A}$ is given by $\mathrm{d}\mathfrak{A} = \hat{\mathcal{I}}_0\,\mathrm{d}\mathcal{A}$, where $\hat{\mathcal{I}}_0$ is the intensity detected at $z = 0$. As a result, the observed intensity field in the focal plane, say $\hat{\mathcal{I}}(r,\varphi)$, is proportional to the projected mass density of membrane, since $\mathrm{d}\mathfrak{A} = \mathcal{I}_0\,\mathrm{d}\mathcal{A} = \hat{\mathcal{I}}(r,\varphi)\,\mathrm{d}\mathcal{A}_\mathrm{p}$, where $\mathcal{A}_\mathrm{p}$ is the surface element given by the projection of the membrane patch $\mathrm{d}\mathcal{A}$ onto the focal plane. This means that $\hat{\mathcal{I}}(r,\varphi)$ is purely a geometrical object that only depends on the three-dimensional configuration of the vesicle.

By taking into account the Gaussian scaling in (4.22), we can construct an intensity field of the light entering the camera, analogous to $\hat{\mathcal{I}}(r,\varphi)$, as follows:

$$\begin{aligned}\mathcal{I}(r,\varphi) \propto \iiint \mathrm{d}\Omega\ \ \mathcal{G}\big(r'\cos\theta'\big)\,\delta\big(r - r'\sin\theta'\big) \\ \delta\big(r'\varphi'\sin\theta' - r\varphi\big)\ \delta\big(r' - \big\|\mathbf{R}(\theta',\varphi')\big\|\big)\,,\end{aligned} \tag{4.23}$$

where the volume integral $\iiint \mathrm{d}\Omega := \int_0^\infty \mathrm{d}r'\, r'^2 \int_0^\pi \mathrm{d}\theta' \sin\theta' \int_0^{2\pi} \mathrm{d}\varphi'$, δ represents a Dirac delta function, and the position vector $\mathbf{R}(\theta',\varphi')$ is defined by equation (4.1). Here, r' measures the radial distance from the centre of the vesicle, and (θ',φ') are the usual spherical angular coordinates, with $\theta' = 0$ (or π) indicating the normal direction of a point above (or below) the focal plane of the objective. On the other

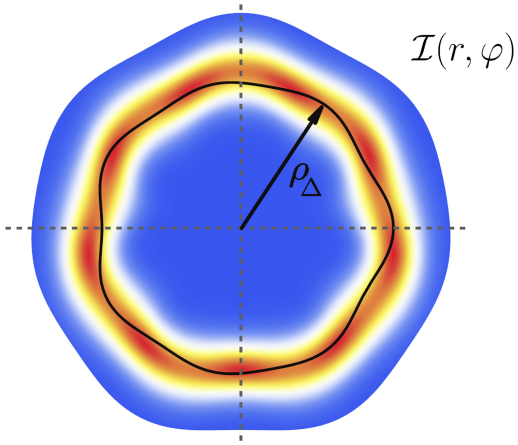

Figure 4.3: Schematic diagram of the intensity field $\mathcal{I}(r,\varphi)$ at the focal plane, which corresponds to the projected membrane surface within the focal depth of the objective (red indicates high intensity, while blue is low). The solid black line represents the first radial moment of the intensity, namely $\rho_\Delta(\varphi) \propto \int_0^\infty r\,\mathcal{I}(r,\varphi)\,\mathrm{d}r$.

hand, the variables r and φ are the polar coordinates in the equatorial plane, with the origin chosen to be at the centre of the vesicle. Moreover, the first delta function in (4.23) gives the projection of radial distances onto the focal plane, the second one specifies that the azimuthal angles are equivalent in both three-dimensional and two-dimensional reference frames, and the third one is a constraint that locates the position of the membrane surface relative to the centre of the vesicle. Thus, by using a quasi-spherical representation, as described in Section 4.1.1, the volume integral over these Dirac delta functions yields the projected shape of the vesicle for a given realisation of the local field $u(\theta',\varphi')$, as illustrated in Figure 4.3.

4.2.2 Lowest-order Radial Moment

Although the intensity field in (4.23) is strictly not a direct experimental observable, its statistical moments are in principle measurable quantities. Thus, the simplest way of extracting information from (4.23) is to analyse the first radial moment of the intensity field (see Figure 4.3), which is defined by

$$\rho_\Delta(\varphi) = \frac{\int_0^\infty r\,\mathcal{I}(r,\varphi)\,\mathrm{d}r}{\int_0^\infty \mathcal{I}(r,\varphi)\,\mathrm{d}r}. \tag{4.24}$$

Reassuringly, this object recovers in the limit of $\Delta \to 0$ the experimental observable $\rho_0(\varphi)$, namely the radial position of the membrane in the equatorial plane of

the vesicle, which is used in Section 4.1.2 to describe the shape fluctuations.

By integrating over the angular variables θ' and φ' in (4.23), the intensity field $\mathcal{I}(r,\varphi)$ can be reduced to a single integral, namely

$$\mathcal{I} \propto \int_r^\infty \mathrm{d}r' \, \frac{\mathcal{G}(r'\cos\Theta)}{\mathcal{R}\cos\Theta} \left\{ \delta\Big[\frac{r'}{\mathcal{R}} - 1 - u(\Theta,\varphi)\Big] + \delta\Big[\frac{r'}{\mathcal{R}} - 1 - u(\pi-\Theta,\varphi)\Big] \right\}, \quad (4.25)$$

where $\Theta = \arcsin(r/r')$ is introduced as a shorthand notation for the sake of clarity. Hence, using the substitutions $r = \xi\mathcal{R}$ and $r' = \xi\mathcal{R}\cosh(\psi)$ in the equation (4.25), then the expression of the first moment (4.24) is given by

$$\rho_{\scriptscriptstyle\Delta}(\varphi) = \frac{\mathcal{R}\int_0^\infty \xi \mathrm{d}\xi \int_0^\infty \mathrm{d}\psi \; \xi\cosh(\psi)\left[\mathfrak{D}(\psi,\xi,\Theta) + \mathfrak{D}(\psi,\xi,\pi-\Theta)\right] e^{-\frac{\xi^2\sinh^2\psi}{2\,\Delta^2}}}{\int_0^\infty \mathrm{d}\xi \int_0^\infty \mathrm{d}\psi \; \xi\cosh(\psi)\left[\mathfrak{D}(\psi,\xi,\Theta) + \mathfrak{D}(\psi,\xi,\pi-\Theta)\right] e^{-\frac{\xi^2\sinh^2\psi}{2\,\Delta^2}}}, \quad (4.26)$$

where the function $\mathfrak{D}$ is defined by

$$\mathfrak{D}(\psi,\xi,\hat{\Theta}) := \delta\Big[\xi\cosh\psi - 1 - u(\hat{\Theta},\varphi)\Big]. \quad (4.27)$$

Moreover, the delta functions in (4.26) can be eliminated by changing the order of integration and then evaluating the integrals over the variable ξ, which yields

$$\mu(\varphi) = \frac{\int_0^1 \mathrm{d}\omega \, (1+u_{\scriptscriptstyle\mathrm{N}})^2 \, \exp\Big(-\frac{(1+u_{\scriptscriptstyle\mathrm{N}})^2}{2\,\Delta^2}\omega^2\Big) + (1+u_{\scriptscriptstyle\mathrm{S}})^2 \, \exp\Big(-\frac{(1+u_{\scriptscriptstyle\mathrm{S}})^2}{2\,\Delta^2}\omega^2\Big)}{\int_0^1 \mathrm{d}\omega \, \frac{(1+u_{\scriptscriptstyle\mathrm{N}})}{\sqrt{1-\omega^2}} \, \exp\Big(-\frac{(1+u_{\scriptscriptstyle\mathrm{N}})^2}{2\,\Delta^2}\omega^2\Big) + \frac{(1+u_{\scriptscriptstyle\mathrm{S}})}{\sqrt{1-\omega^2}} \, \exp\Big(-\frac{(1+u_{\scriptscriptstyle\mathrm{S}})^2}{2\,\Delta^2}\omega^2\Big)}, \quad (4.28)$$

where we define $\mu(\varphi) := \rho_{\scriptscriptstyle\Delta}(\varphi)/\mathcal{R}$, $u_{\scriptscriptstyle\mathrm{N}} := u(\Theta,\varphi)$ and $u_{\scriptscriptstyle\mathrm{S}} := u(\pi-\Theta,\varphi)$, and a change of variables $\omega = \tanh(\psi)$ is used to further simplify the expression.

Since the shape undulations are assumed to be small compared to the mean radius of the quasi-sphere, namely $|u| \ll 1$, the equation (4.28) can be expanded to first order in $u_{\scriptscriptstyle\mathrm{N}}$ and $u_{\scriptscriptstyle\mathrm{S}}$, and found to be a function of only $\tilde{u} := u_{\scriptscriptstyle\mathrm{N}} + u_{\scriptscriptstyle\mathrm{S}}$, as follows:

$$\mu(\varphi) = \mu_0 + \frac{\int_0^1 \mathrm{d}\omega \left(\frac{2\Delta^2+\omega^2}{\Delta^2} - \mu_0\frac{\Delta^2+\omega^2}{\Delta^2\sqrt{1-\omega^2}}\right)\tilde{u}(\omega,\varphi)\, e^{-\frac{\omega^2}{2\,\Delta^2}}}{2\int_0^1 \frac{\mathrm{d}\omega}{\sqrt{1-\omega^2}}\, e^{-\frac{\omega^2}{2\,\Delta^2}}} + \mathcal{O}\big(\tilde{u}^2\big), \quad (4.29)$$

where the coefficient μ_0 is the zeroth order term in the expansion of $\mu(\varphi)$, which is

given by

$$\mu_0 = \frac{\int_0^1 \mathrm{d}\omega\, e^{-\frac{\omega^2}{2\Delta^2}}}{\int_0^1 \frac{\mathrm{d}\omega}{\sqrt{1-\omega^2}}\, e^{-\frac{\omega^2}{2\Delta^2}}} = \frac{\frac{\Delta\sqrt{\pi}}{\sqrt{2}}\,\mathrm{erf}\left(\frac{1}{\Delta\sqrt{2}}\right)}{\frac{\pi}{2}\,I_0\left(\frac{1}{4\Delta^2}\right)e^{-\frac{1}{4\Delta^2}}} \overset{\Delta\to 0}{=} 1, \tag{4.30}$$

with erf as the error function and I_0 as the modified Bessel function of the first kind of order zero [168]. Thus, equation (4.29) gives the first order perturbation about the spherical configuration, $\hat{\mu}(\varphi) := \mu(\varphi) - \mu_0$, namely

$$\hat{\mu}(\varphi) = \frac{\exp\left(\frac{1}{4\Delta^2}\right)}{\pi I_0\left(\frac{1}{4\Delta^2}\right)} \int_0^1 \mathrm{d}\omega \left(\frac{2\Delta^2+\omega^2}{\Delta^2} - \mu_0 \frac{\Delta^2+\omega^2}{\Delta^2\sqrt{1-\omega^2}}\right) \tilde{u}(\omega,\varphi)\, e^{-\frac{\omega^2}{2\Delta^2}}. \tag{4.31}$$

Analogous to the calculation of the equatorial fluctuations in Section 4.1.2, this azimuthal function can now be used to obtain a fluctuation spectrum by Fourier transforming it in the angle φ, yielding $\hat{\mu}_q$, and subsequently by computing the thermal ensemble average of $|\hat{\mu}_q|^2$. As mentioned before, in the limit of $\Delta \to 0$, this mode spectrum is identically equivalent to (4.18). However, for finite Δ, this contains a correction due to the finite size of the focal depth. As a result, the effect induced by the projection of shape fluctuations out of the focal plane can be studied within this simple model, where the details are given in the next section. In Section 4.3, this is further analysed and compared to experimental data and its consequences on the inferred values of the membrane elastic constants is discussed.

4.2.3 Calculation of the Fourier Spectrum

By Fourier transforming equation (4.31) with respect to the angle φ, this yields

$$\hat{\mu}_q := \frac{1}{2\pi} \int_{-\pi}^{+\pi} \mathrm{d}\varphi\, \hat{\mu}(\varphi)\, e^{iq\varphi} = \int_0^1 \mathrm{d}\omega\, \mathcal{N}(\omega,\Delta)\, \tilde{u}_q(\omega), \tag{4.32}$$

where in the last step we use the explicit form of (4.31) and then interchange the order of integration. Hence, by defining the Fourier transform of $\tilde{u}(\omega,\varphi)$ as $\tilde{u}_q(\omega)$, and also by absorbing the other remaining terms in a new function $\mathcal{N}(\omega,\Delta)$, then the final result in equation (4.32) can be obtained.

By using the basis representation in (4.7) and by rewriting the spherical harmonics as $Y_n^m(\theta,\varphi) = e^{im\varphi}\,\mathcal{P}_n^m(\cos\theta)$, where

$$\mathcal{P}_n^m(\cos\theta') = \sqrt{\frac{2n+1}{4\pi}\frac{(n-m)!}{(n+m)!}}\, P_n^m(\cos\theta'), \tag{4.33}$$

with P_n^m being the associated Legendre polynomials [168], then the Fourier trans-

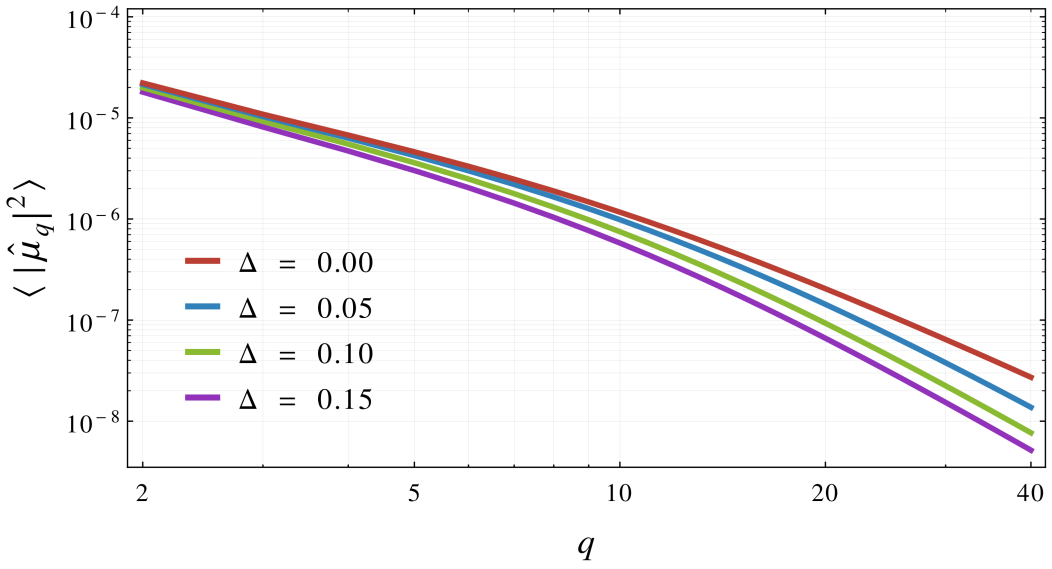

Figure 4.4: Log-log plot of the mean squared amplitudes $\langle |\hat{\mu}_q|^2 \rangle$ as a function of the azimuthal mode number q for some values of the focal depth Δ. Here, $\kappa = 20\ k_B T$ and $\bar{\sigma} = 100$, and a straight line interpolation is used between the points.

form of $\tilde{u}(\omega, \varphi)$ is found to be

$$\tilde{u}_q(\omega) = \sum_{n \geq q} \mathcal{U}_{n,q} \left[\mathcal{P}_n^q(\omega) + \mathcal{P}_n^q(-\omega) \right] = \sum_{n \geq q} \mathcal{U}_{n,q}\, \mathcal{P}_n^q(\omega) \left[1 + (-1)^{n+q} \right], \tag{4.34}$$

where the identity $\mathcal{P}_n^q(-\omega) = (-1)^{n+q}\, \mathcal{P}_n^q(\omega)$ is used in the last step [49]. As a result, using (4.32), the mean squared amplitude of each Fourier mode can be determined as follows (see Figure 4.4):

$$\langle |\hat{\mu}_q|^2 \rangle = \sum_{n \geq q} \langle |\mathcal{U}_{n,q}|^2 \rangle \left\{ \left[1 + (-1)^{n+q} \right] \int_0^1 \mathrm{d}\omega\, \mathcal{N}(\omega, \Delta)\, \mathcal{P}_n^q(\omega) \right\}^2, \tag{4.35}$$

where the orthogonality of the flickering amplitudes in (4.16) is employed. Moreover, using the explicit form of $\mathcal{N}(\omega, \Delta)$, the term in the curly brackets, say $\mathcal{L}_{n,q}$, can be written as

$$\mathcal{L}_{n,q} = \frac{1 + (-1)^{n+q}}{\pi\, I_0\left(\frac{1}{4\Delta^2}\right) e^{-\frac{1}{4\Delta^2}}} \int_0^1 \mathrm{d}\omega\, \mathcal{P}_n^q(\omega) \left[\frac{2\Delta^2 + \omega^2}{\Delta^2} - \frac{\mu_0\left(\Delta^2 + \omega^2\right)}{\Delta^2 \sqrt{1 - \omega^2}} \right] e^{-\frac{\omega^2}{2\,\Delta^2}}, \tag{4.36}$$

which recovers the coefficients $\mathcal{E}_{n,q}$ of (4.18) in the limit of $\Delta \to 0$ as expected. This can be shown by a method of steepest descent. Namely, when Δ goes to zero, the exponential term within the integrand of (4.36) vanishes unless $\omega = 0$. Therefore,

the term in the square brackets of (4.36) tends to unity, and the integral reduces to

$$\lim_{\Delta\to 0}\mathcal{L}_{n,q} = \lim_{\Delta\to 0}\frac{1+(-1)^{n+q}}{\pi\, I_0\left(\frac{1}{4\Delta^2}\right) e^{-\frac{1}{4\Delta^2}}}\int_0^1 \mathrm{d}\omega\; \mathcal{P}_n^q(0)\, e^{-\frac{\omega^2}{2\,\Delta^2}} \tag{4.37}$$

$$= \lim_{\Delta\to 0}\frac{\mu_0}{2}\left[1+(-1)^{n+q}\right]\mathcal{P}_n^q(0), \tag{4.38}$$

which indeed leads to $\mathcal{E}_{n,q}$ by using (4.33), (4.30), and the property that $\mathcal{P}_n^m(0) = 0$ when $n+m$ is an odd integer number [49].

Although it is possible to find a closed form expression for $\mathcal{L}_{n,q}$ by performing the integral exactly, the general result involves two finite sums over four confluent hypergeometric functions of the first kind [168], and thus it is not any more enlightening than the result given in equation (4.36). However, this means that on a practical level $\mathcal{L}_{n,q}$ can be tabulated for some fixed values of n and q, instead of numerically evaluating the integral (see Table 4.1 for a few of such examples).

4.3 Experimental Analysis

As discussed in Section 4.1.2, the existing approach to determine the bending modulus in flicker spectroscopy experiments involves relating the time correlation function of the equatorial fluctuations, as given (4.20), to the fluctuation spectrum measured from the observed contours [103]. Analogous to the spectrum (4.20), we can construct a time correlation function for the fluctuations in the first radial moment of the intensity field (4.23), namely

$$\left\langle \bar{\mu}_q(t)\,\bar{\mu}_q^*(t)\right\rangle_t = \sum_{n\geq q}\mathcal{L}_{n,q}^2\left\langle\left|\mathcal{U}_{n,q}\right|^2\right\rangle\frac{\tau_{n,q}^2}{\tau^2}\left(1-e^{-\tau/\tau_{n,q}}\right)^2, \tag{4.39}$$

where the time-average $\bar{\mu}_q(t) := \tau^{-1}\int_0^\tau \mathrm{d}t'\;\hat{\mu}_q(t+t')$, τ is the acquisition time of the camera, $\tau_{n,q}$ is the characteristic relaxation time associated to each spherical harmonic mode, as given by (4.19), and the functions $\mathcal{L}_{n,q}$ and $\left\langle\left|\mathcal{U}_{n,q}\right|^2\right\rangle$ are defined by the equations (4.36) and (4.16), respectively.

In general, a point source observed under a microscope suffers by in-plane blurring in the focal plane of the objective, which is usually described by a two-dimensional convolution over a kernel that is commonly referred to as the point spread function [182]. By assuming a Gaussian point spread function of width Σ_w, it can be shown that the first radial moment of the intensity in equation (4.26) remains unchanged to first-order corrections in Σ_w. Moreover, since Σ_w is measured to be an order of magnitude smaller than the focal depth $\Delta\mathcal{R}$, we neglect the effect of

(n,q)	$\mathcal{L}_{n,q}$
$(2,2)$	$\dfrac{e^{-\frac{1}{4\Delta^2}}\left\{10\sqrt{30}\Delta^2 I_0\left(\frac{1}{4\Delta^2}\right)-\sqrt{15\pi}\,e^{\frac{1}{2\Delta^2}}\,\Delta\left[5\left(2\Delta^2-1\right)I_0\left(\frac{1}{4\Delta^2}\right)+3I_1\left(\frac{1}{4\Delta^2}\right)\right]\mathrm{erf}\left(\frac{1}{\sqrt{2}\Delta}\right)\right\}}{8\pi^{3/2}\left[I_0\left(\frac{1}{4\Delta^2}\right)\right]^2}$
$(4,2)$	$\dfrac{e^{-\frac{1}{4\Delta^2}}\left\{9\sqrt{10}\Delta^2\left(49\Delta^2+3\right)I_0\left(\frac{1}{4\Delta^2}\right)-3\sqrt{5\pi}\,e^{\frac{1}{2\Delta^2}}\,\Delta\left[\left(35\Delta^2+2\right)I_1\left(\frac{1}{4\Delta^2}\right)+\left(147\Delta^4-40\Delta^2-1\right)I_0\left(\frac{1}{4\Delta^2}\right)\right]\mathrm{erf}\left(\frac{1}{\sqrt{2}\Delta}\right)\right\}}{8\pi^{3/2}\left[I_0\left(\frac{1}{4\Delta^2}\right)\right]^2}$
$(4,4)$	$\dfrac{e^{-\frac{1}{4\Delta^2}}\left\{9\sqrt{70}\left(1-7\Delta^2\right)\Delta^2 I_0\left(\frac{1}{4\Delta^2}\right)+3\sqrt{35\pi}\,e^{\frac{1}{2\Delta^2}}\,\Delta\left[\left(5\Delta^2-1\right)I_1\left(\frac{1}{4\Delta^2}\right)+\left(21\Delta^4-10\Delta^2+2\right)I_0\left(\frac{1}{4\Delta^2}\right)\right]\mathrm{erf}\left(\frac{1}{\sqrt{2}\Delta}\right)\right\}}{16\pi^{3/2}\left[I_0\left(\frac{1}{4\Delta^2}\right)\right]^2}$
$(6,2)$	$\dfrac{\sqrt{1365}\,e^{-\frac{1}{4\Delta^2}}\,\Delta\left\{4\Delta\left(4455\Delta^4+414\Delta^2+35\right)I_0\left(\frac{1}{4\Delta^2}\right)+\sqrt{2\pi}\,e^{\frac{1}{2\Delta^2}}\left[\left(-8910\Delta^6+2142\Delta^4+41\Delta^2+20\right)I_0\left(\frac{1}{4\Delta^2}\right)-3\left(616\Delta^4+39\Delta^2+6\right)I_1\left(\frac{1}{4\Delta^2}\right)\right]\mathrm{erf}\left(\frac{1}{\sqrt{2}\Delta}\right)\right\}}{128\pi^{3/2}\left[I_0\left(\frac{1}{4\Delta^2}\right)\right]^2}$
$(6,4)$	$\dfrac{3\sqrt{91}\,e^{-\frac{1}{4\Delta^2}}\,\Delta\left\{\sqrt{\pi}\,e^{\frac{1}{2\Delta^2}}\left[\left(616\Delta^4-21\Delta^2+2\right)I_1\left(\frac{1}{4\Delta^2}\right)+\left(2970\Delta^6-966\Delta^4+53\Delta^2-4\right)I_0\left(\frac{1}{4\Delta^2}\right)\right]\mathrm{erf}\left(\frac{1}{\sqrt{2}\Delta}\right)-6\sqrt{2}\left(495\Delta^5+4\Delta^3+\Delta\right)I_0\left(\frac{1}{4\Delta^2}\right)\right\}}{64\pi^{3/2}\left[I_0\left(\frac{1}{4\Delta^2}\right)\right]^2}$
$(6,6)$	$\dfrac{\sqrt{3003}\,e^{-\frac{1}{4\Delta^2}}\,\Delta\left\{12\left(45\Delta^5-6\Delta^3+\Delta\right)I_0\left(\frac{1}{4\Delta^2}\right)+\sqrt{2\pi}\,e^{\frac{1}{2\Delta^2}}\left[\left(-56\Delta^4+11\Delta^2-2\right)I_1\left(\frac{1}{4\Delta^2}\right)+\left(-270\Delta^6+126\Delta^4-23\Delta^2+4\right)I_0\left(\frac{1}{4\Delta^2}\right)\right]\mathrm{erf}\left(\frac{1}{\sqrt{2}\Delta}\right)\right\}}{128\pi^{3/2}\left[I_0\left(\frac{1}{4\Delta^2}\right)\right]^2}$

Table 4.1: The closed form expressions of the functions $\mathcal{L}_{n,q}$ for a few values of n and q. Here, the functions I_0 and I_1 are the modified Bessel functions of the first kind of order zero and one, respectively, and erf is the error function. In general, we have that $\mathcal{L}_{n,q}=0$ if $n<q$ and also if $n+q$ is an odd integer number.

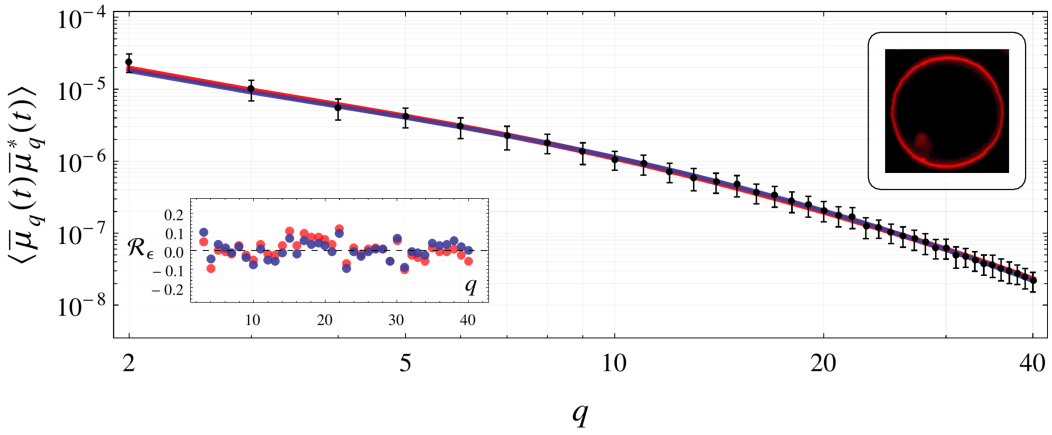

Figure 4.5: The fluctuation spectrum for a GUV of mean radius $\mathcal{R} \approx 23$ μm, which is imaged by using a confocal fluorescence technique, where $\tau = 1$ ms and $\Delta = 0.03$. The error-bars represent the corresponding standard errors in the mean, which are scaled by a factor of 10 to make them for visible on the plot. The spectrum is plotted on a log-log scale and their best-fit lines for the models (4.20), explicitly $\Delta = 0$, and (4.39), $\Delta = 0.03$, are shown by the red and blue curves, respectively. Although both fitting curves are of similar quality, importantly, their best-fit parameters are found to be: $\kappa = 19.1 \pm 0.2\ k_BT$ and $\bar{\sigma} = 119 \pm 3$ for $\Delta = 0$, and $\kappa = 14.8 \pm 0.2\ k_BT$ and $\bar{\sigma} = 176 \pm 4$ for the blue line with $\Delta = 0.03$. The inset plot shows the normalised residuals, $\mathcal{R}_\epsilon(q)$, by their corresponding standard deviation for each q-mode.

the point spread function on the intensity moment ρ_Δ. In addition, Σ_w can be used as an indicator of the optical resolution of our microscope, yielding as a result an optical cutoff for the fluctuation spectrum (4.39), namely $q \lesssim q_w := \mathcal{R}/\Sigma_w$, beyond which we expect the spectrum to be highly dominated by white noise associated with the imaging system (e.g. electronic noise related to the video-camera).

By comparing with a number of experiments on GUVs carried out by our collaborators, Dr. Pietro Cicuta and Dr. Davide Orsi, which are prepared by means of electroformation [183] with DOPC and the fluorescent labeled lipid Texas Red DHPE in proportions of 99.2% and 0.8%, respectively, the model (4.39) can be used to estimate the values of κ and $\bar{\sigma}$. Moreover, the interior of vesicles is filled with a 197 mM sucrose solution, whilst their exterior comprises of a 200 mM glucose solution. Hence, this gives rise to a density difference of about 0.05 g/mol, which leads to the sedimentation of GUVs onto the bottom of the object glass, conveniently reducing their diffusive motion in suspension[¶]. The sample preparation of the GUVs and the experimental measurements of their observed fluctuation spectrum were

[¶]Furthermore, this sucrose–glucose mixture provides a non-zero refractive index difference, which is required if one wants to image the vesicles by a phase-contrast technique.

performed entirely by Dr. Pietro Cicuta and Dr. Davide Orsi in the Cavendish Laboratory at the University of Cambridge (United Kingdom).

The microscopy experiments have been carried out on a Leica TCS SP5 confocal scanning inverted microscope, where each individual vesicle is imaged in a confocal fluorescence mode. Consequently, this allows control of the focal depth Δ by varying the pin-hole size of the microscope. The fluctuation spectrum is obtained from short-exposure time videos of the GUVs (with $\tau \sim 1$–10 ms), where the position of each contour in every frame is determined by using the maximum of the observed radial intensity. The analysis and detection of the contours (performed by Cicuta and Orsi) follows a procedure similar to one described in [103], which allows us to obtain the time-dependent position of the membrane and the corresponding mean-squared deviations in the Fourier space, which we denote here by $F(q, \Delta)$, where q is the Fourier mode number and Δ is the focal depth at which the measurements have been performed (see Figure 4.5 for a example).

The best-fit parameters to the experimental data are found by means of a maximum likelihood estimate [184] for the model (4.39), namely we seek to minimise the following function:

$$\chi^2_\ell(\kappa, \bar{\sigma}) = \sum_{q=q_{\min}}^{q_{\max}} \left(\frac{F(q, \Delta_\ell) - \left\langle \bar{\mu}_q(t)\, \bar{\mu}^*_q(t) \right\rangle_t}{\Sigma(q, \Delta_\ell)} \right)^2, \tag{4.40}$$

where $\Sigma(q, \Delta_\ell)$ is the standard error in the mean associated to $F(q, \Delta_\ell)$, and ℓ labels the data measured at different focal depths on the same vesicle. Here, $q_{\min}$ and $q_{\max}$ define the upper and lower bounds of the q-mode fitting range, respectively, as well as the statistical degrees of freedom of χ^2_ℓ (that is, $d_f := q_{\max} - q_{\min} + 1$). The lower bound is typically chosen to be $q_{\min} = 3$, because of the poor statistics of the second q-mode. Due to the rapid convergence to zero of $\mathcal{L}^2_{n,q}$, the summation in (4.39) is truncated at a mode number $n = q + 20$. In addition, the upper bound of the fitting range $q_{\max}$ is selected such that the exponential decay term in (4.39) only weakly affects each term in the sum, namely we choose $q_{\max}$ such that $\tau \simeq \tau_{n_{\max}, q_{\max}} \ln 2$ (half-life time), where $n_{\max} = q_{\max} + 20$. However, the relaxation time $\tau_{n,q}$ is a function of κ and $\bar{\sigma}$ whose values are determined by the fitting procedure itself. Thus, we need to solve for $q_{\max}$ recursively, where we additionally impose that its value is less or equal to twice the value of the crossover mode $q_c := \mathcal{R}/\lambda = \sqrt{\bar{\sigma}}$, where $\lambda = \sqrt{\kappa/\sigma}$ is the membrane correlation length, and the final equality holds as the mean spontaneous curvature $H_0 = 0$ in our experiments. As discussed in Section 2.2.2, this crossover q-mode separates the regimes in which the membrane is

Method	Bending modulus (κ/k_BT)
X-ray scattering on bilayer stacks	17 ± 2 (from [85, 185–188])
Micropipette aspiration of GUVs	19 ± 2 (from [71])
Pulling membrane tethers	19 ± 2 (from [189, 190])
Flicker spectroscopy of GUVs	27 ± 3 (from [67, 191])

Table 4.2: The measured values of the bending modulus κ of a DOPC membrane using different experimental techniques (at room temperature). The values of κ represent the mean estimates from each given citation. Adapted from [67].

mainly dominated by the surface tension term (when $q \lesssim q_c$) and the bending rigidity term (when $q \gtrsim q_c$). Since the fluctuation spectrum in these limits is characterised by different functional forms (particularly, from equation (2.37), we find the power-laws q^{-2} and q^{-4} if the modes $q \lesssim q_c$ and $q \gtrsim q_c$, respectively), this crossover mode is required to lie in the middle of the fitting range for q, leading therefore to the following condition $q_w \gtrsim q_{\max} \approx 2q_c$, with q_w the optical cutoff discussed above.

A systematic decrease in the estimated value of the bending modulus κ is found when the experimental data is fitted with the non-zero Δ-model (4.39) in comparison with the common approach given by (4.20), e.g. see the best-fit parameters in Figure 4.5. By imaging a relatively small GUV of radius $\mathcal{R} \approx 10$ μm at different pin-hole sizes, the fluctuation spectrum associated to each Δ_ℓ gives a number of ℓ individual estimates for the bending rigidity, as shown in Figure 4.6. Also, using a maximum likelihood estimate over all the spectra at different values of the focal depth Δ_ℓ, namely we minimise the function

$$\chi^2(\kappa, \bar{\sigma}) = \sum_\ell \chi^2_\ell(\kappa, \bar{\sigma}), \tag{4.41}$$

this yields $\kappa = 17 \pm 1\ k_BT$[‖]. However, if all the spectra is fitted instead with the standard model in (4.20), then we obtain $\kappa = 27 \pm 1\ k_BT$, which is considerably larger than the value one would obtain with $\Delta \neq 0$. To illustrate the dependence of the inferred values of κ with the focal depth Δ, the previous fitting procedure (4.41) used over all the spectra is repeated at arbitrary non-zero values of Δ in order to

[‖]It is noteworthy to mention that the estimation of the confidence interval is computed through the covariance matrix (or Hessian matrix) of the maximum likelihood function, which depends on the rather tight error-bars used in the spectra, that is, the standard error in the mean associated to each q mode. In addition to this statistical estimate, other systematic errors related to the experimental and imaging set-up can be included to obtain a more reliable measure of the confidence interval.

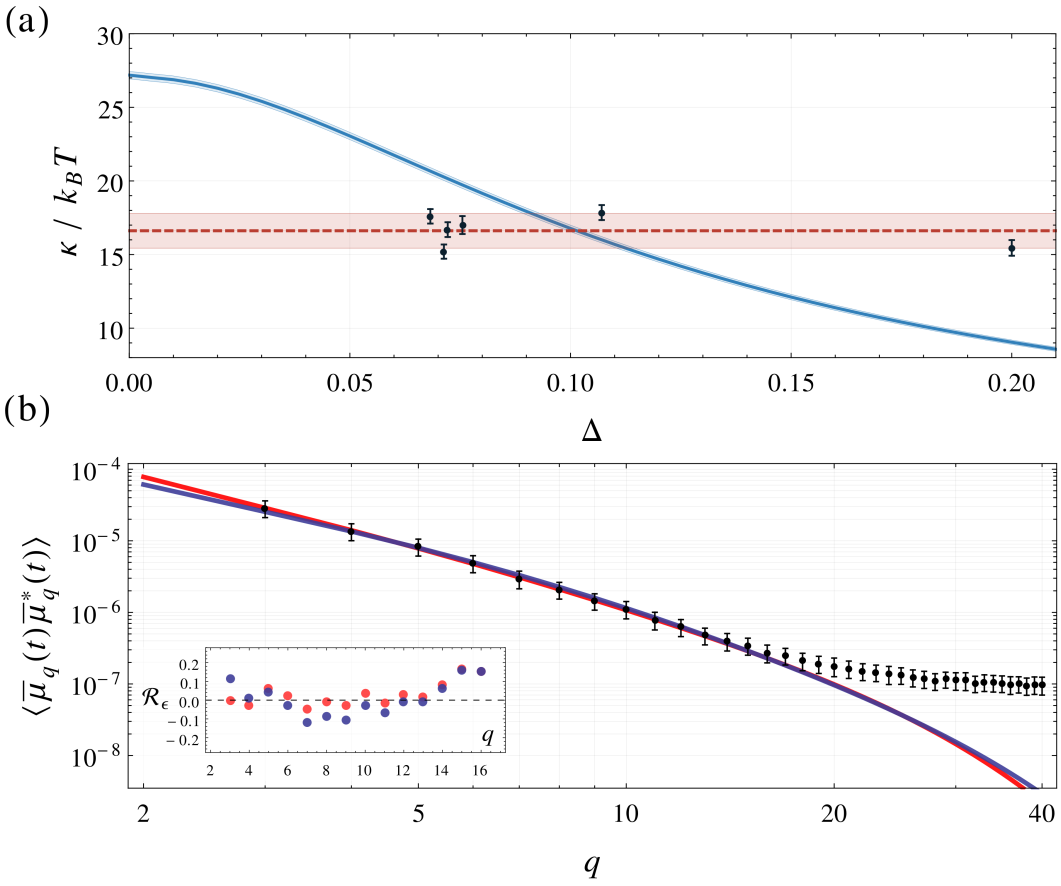

Figure 4.6: Data representation of a single GUV of mean radius $\mathcal{R} = 10.2$ μm, which is observed under a confocal microscope (with $\tau \simeq 1$ ms the inverse scanning rate). (a) The inferred values of the bending modulus κ from the fluctuation spectra of the vesicle individually measured at different focal depths Δ (black points). The error-bars represent the 95% confidence interval that are measured from the covariance matrix (or Hessian matrix) of $\chi^2_\ell(\kappa, \bar{\sigma})$ in equation (4.40). The dash red line represents a mean estimate of κ over all Δ measurements, whereas the blue curve illustrates the value of the bending rigidity one would find if the whole data is fitted at a fixed value of Δ. In particular, the estimate of $\kappa = 27\ k_BT$ at $\Delta = 0$ represents the value that one would obtain if the standard model in (4.20) is used to fit the data. Here, the shaded region around the red dashed line indicates the 95% confidence bands. (b) One of the spectra from figure (a), where $\Delta = 0.107$. The error-bars represent the standard error in the mean of each corresponding measurement, but scaled by a factor of 10 for clarity, and their best-fit lines for the models (4.20) and (4.39) are shown by the red and blue curves, respectively. Furthermore, the inset plot shows the normalised residuals $\mathcal{R}_\epsilon$ for each q-mode (same colour convention). Since the optical resolution cut-off is found to be $q_w \approx 25$, this may explain the flatting of the spectrum for $q \gtrsim 20$, being a regime mainly dominated by noise.

construct an interpolation curve, which is depicted in Figure 4.6 as the blue line. This shows that the effect of non-zero focal depth leads to a significant decrease in the estimated value of the bending modulus.

It is a primary result of the present work that this correction reveals that the flickering experiments are now in good agreement with the other methods, such as X-ray scattering on membrane stacks, the micropipette aspiration technique, and the method of pulling tethers from GUVs [67], as shown in Table 4.2. This disagreement has previously been noted in the literature: the values for κ determined from the shape analysis of giant unilamellar vesicles have previously been larger than those obtained from micromechanical manipulation methods [67]. Thus, the correction due to the projection of thermal shape fluctuations out of the focal plane of the microscope seems to represent a pivotal ingredient in the estimation of the membrane elastic constants by flicker spectroscopy experiments.

4.4 Summary

In this chapter we present the theoretical methodology necessary to obtain the bending rigidity of membranes by studying the thermal shape fluctuations of vesicles. The framework of quasi-spherical vesicles is discussed in Section 4.1.1, where the calculation of the partition function (over all possible shapes induced by thermal fluctuations) is analytically computed by restricting our analysis to quadratic fluctuations about a spherical configuration. In Section 4.1.2, we discuss the current approach to relate the theoretical model to the experimental data, which consists of an analysis of the equatorial fluctuations. This method neglects the fluctuations out of this plane. As a consequence, in Section 4.2, we develop a simple model to account for the correct projection of thermal shape undulations onto the equatorial plane. This involves an idealisation of the imaging system, in which we impose a Gaussian filter on the intensity of light arriving from membrane elements above or below the focal plane. This approach allows us to extract material information by comparing the statistics of the first radial moment of the projected intensity with the experimental data. This is detailed in Section 4.3, where a comparison of our model with the existing approach (that uses only equatorial fluctuations without averaging out of this plane) shows a systematic decrease in the value of the bending modulus by nearly a factor of two. Therefore, the correction due to the projection of shape fluctuations plays a crucial role in the estimation of the membrane rigidity by means of flicker spectroscopy experiments.

Chapter 5

Role of Recycling in Non-equilibrium Membranes

Biological membranes are highly dynamic two-dimensional systems, consisting of a multitude of different lipids and proteins, which are continuously exchanged with rest of the living cell by the secretion and absorption of small vesicles which are on the order of 100 nm in diameter [1]. This constant recycling of the cell membranes leads to a complete turnover of its constituents in about 12 minutes [192]. Furthermore, the membrane components are observed to be inhomogeneously distributed within the bilayer, where some of the lipids and proteins cluster into small-scale lateral domains with a diameter of few tens of nanometers, which are commonly referred to as lipid rafts [28, 29]. Although there is a growing evidence of their existence and biological significance to living cells, there are still many unanswered questions that concerns their origin and nature both *in vivo* and *in vitro* [45, 193–197]. Here, we explore the possibility of regulating the formation of stable nano-scale domains by recycling, where their size is controlled by the permanent exchange rates of membrane components with an external reservoir. Within a mean-field description of the domain kinetics, we show how a continuous recycling can provide a mechanism for the formation of raft-like structures in non-equilibrium fluid membranes.

5.1 Introduction

The presence of distinct nano-scale domains in biomembranes has been confirmed by numerous experiments. However, this evidence is based on indirect measurements, such as the diffusive trajectories of labelled lipids or proteins which show a temporary confinement to a small region of the cell membrane [198–201]. Further supporting

evidence is captured by the biochemical experiments on membrane samples which are dissolved in specific detergents. Since a significant portion of the biomembranes has been found to be resistant to the detergent, it has been hypothesised that this membrane fraction corresponds to some supermolecular structures (raft-like) that move within the membrane [39, 202]. There is also a body of accumulated evidence that certain proteins have high affinity to lipid rafts, which can be recruited to (or removed from) the rafts through the attachment (or the enzymatic cleavage) of their hydrocarbon anchors [39]. As a consequence, this protein–raft affiliation results in various membrane functions that can be associated with lipid rafts [203].

As discussed in Section 1.2, the characteristic features of lipid rafts are their average size and composition. Namely, they are small membrane domains with a typical size in the range of 10–200 nm, which are highly enriched in cholesterol, sphingolipids (e.g. sphingomyelin, abbreviated by SM, as shown in Figure 1.4), and saturated phospholipids [193]. As sphingolipids have a high melting temperature [39], together with the high concentration of cholesterol (which encourages the ordering of the hydrocarbon chains), this suggests than lipid rafts are membrane patches in a liquid-order phase (as discussed in Section 1.4). Because of this, many mixtures of few lipid species have been widely investigated using fluorescence microscopy (e.g. a mixture of DOPC, SM, and cholesterol), which show that lipid phase separation can occur in model membrane systems, giving rise to raft-like structures that resemble a liquid-order phase [196]. Nonetheless, the size of these domains are much larger than those observed in cells. This is expected as the phase separation in a two-component mixture manifests itself by the appearance of separated domains (below a critical temperature), which then grow until they reach the size of the system [204]. However, this separation occurs without any intermediate stable sizes, such as the nano-scale length of lipid rafts. This simple argument makes the existence of lipid rafts somewhat surprising from a physical point of view, as they posses a characteristic size that is much smaller than the typical diameter of cells.

A number of explanations have been put forth [45]. One simple solution relies on the observation that mixtures of cholesterol and saturated and unsaturated lipid molecules can undergo phase separation into two phases, namely, a phase in which the first two membrane components prevail, whereas the other phase is rich only in the third one [196]. As a result, raft-like structures can be obtained in this two-phase region as the domains of the minority phase which are completely enclosed by the other. The relatively small size of the domains can be attributed to the effects due to cytoskeleton pinning, binding of cross-linkers (such as Shiga toxin), extracellular adhesion (e.g. cell-cell junctions, or interactions with the extracellular matrix), or

membrane curvature [205] – just to name a few. The physical and biological aspects of these effects are beyond the scope of this study and thus the reader is referred to the interesting reviews in [45] and [205] for a fuller account.

Here we study the role of membrane recycling, which is ubiquitous in living cells, and its contribution to the stability of the membrane nano-domains. The small size of the latter emergences in this case from the non-equilibrium nature of biomembranes [206, 207], where its constituents are constantly brought to and removed from the membrane through a variety of biological processes that involve the transport of endosomes (that is, vesicles with a diameter on the order of tens of nanometers) within the interior of cells [208]. In the next section, using a planar two-component fluid membrane, we develop an out-of-equilibrium model for the aggregation and kinetics of lipid domains via membrane recycling and intramembrane dynamics. The interplay between the in-plane phase separation of the binary mixture and the constant exchange of membrane components leads to the formation of stable raft-like entities. A comparison of this model with experiments may allow the verification of the recycling mechanism as a regulator of domain size, and also the estimation of our parameters that control membrane recycling.

5.2 Membrane Domains under Recycling

In this section, we examine the dynamics and steady-state distribution of the domain sizes within a continuum theory of non-equilibrium phase separation under membrane recycling, which is based on a discrete model previously introduced by [206]. We consider an infinite planar membrane that is populated by two lipid species, where one of them undergoes a phase separation, giving rise to domains of various sizes, say a (and measured in area units), which are surrounded by the other membrane component. Under a continuous recycling, the dynamics of the domain size distribution is governed by the following master equation:

$$\frac{\mathrm{d}\mathcal{P}}{\mathrm{d}t} = \mathcal{R}(a,t) - D\int_0^\infty \mathcal{P}(a,t)\,\mathcal{P}(a',t)\,\mathrm{d}a' + \frac{D}{2}\int_0^a \mathcal{P}(a',t)\,\mathcal{P}(a-a',t)\,\mathrm{d}a', \quad (5.1)$$

where $\mathcal{P}(a,t)$ represents a density function at time t for the number-per-area of domains of size a. Here, the domain scission events are assumed to be rare and thus neglected in this model. As discussed in [206], this approximation corresponds to the asymptotic regime of large line tension. This parameter characterises the energy cost for having a finite boundary between the different phases. Since the lipids are assumed to phase separate, our regime of interest is high line tension. The low

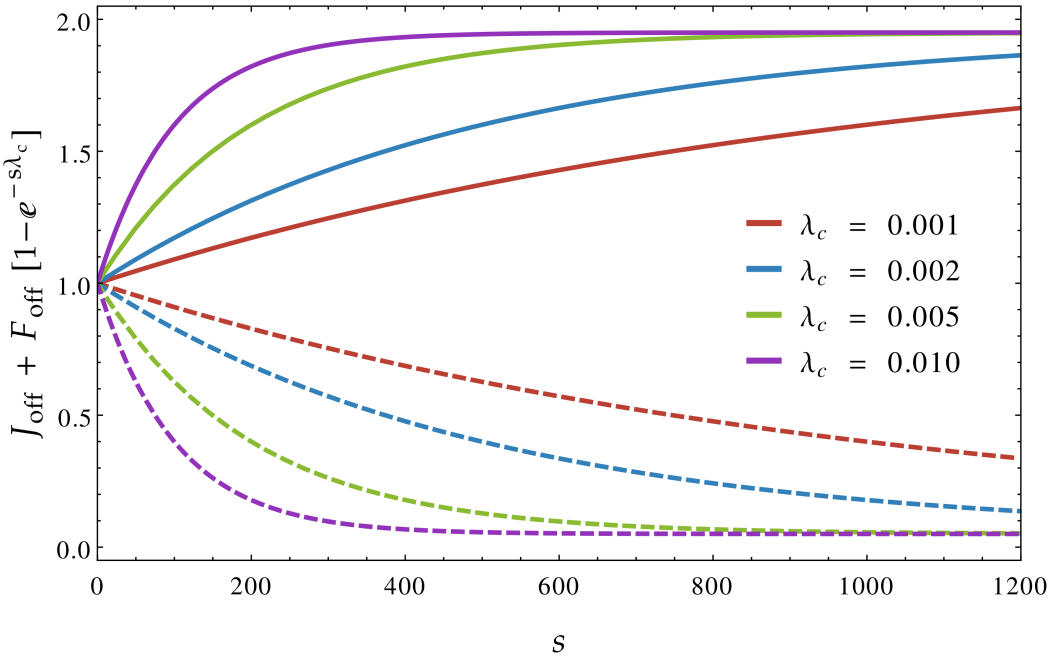

Figure 5.1: Raft removal rate in the recycling scheme (5.2) for various values of λ_c, where the dimensionless size $s = a\,\omega$, and the rescaled outward fluxes $J_{\text{off}} = j_{\text{off}}/(\omega\,D) = 1$ and $F_{\text{off}} = f_{\text{off}}/(\omega\,D) = -0.95$ (dashed lines) and $+0.95$ (solid lines), with the same colour convention. This illustrates that the model (5.2), depending on the sign of F_{off}, can account for both recycling at small and large scales.

tension case simply resembles a gas of non-interacting (mostly monomeric) domains. As a result, the in-plane diffusive dynamics of domains is primarily dominated by the aggregation events, where we assume that two domains fuse whenever they come into contact through diffusion. Hence, the fusion rate can be regarded as a constant proportional to the characteristic diffusion coefficient D of the lipid rafts*. Since this is the only parameter that describes the intramembrane dynamics, the fusion rate can be chosen to be identically D, corresponding to a simple rescaling which fixes the relevant time scale in our model. Furthermore, $\mathcal{R}(a,t)$ is a function that controls the lipid recycling and its explicit form is given by

$$\mathcal{R}(a,t) = j_{\text{on}}\,\omega\exp(-a\,\omega) - j_{\text{off}}\,\mathcal{P}(a,t) - f_{\text{off}}\,[1-\exp\left(-a\,\omega\lambda_c\right)]\,\mathcal{P}(a,t), \qquad (5.2)$$

where single domains are brought to the membrane at random with a rate j_{on} (in units of number-per-area-and-per-time) and with a size drawn from an exponen-

*Due to the logarithmic dependence of the diffusion coefficient on the size of the membrane domains, namely $D \sim \log(1/a)$, according to Saffman-Delbruck theory [209], we thus neglect any size-dependence of the fusion rate as result.

tial distribution for convenience. Here, $\omega > 0$ is the exponential decay constant, representing the characteristic inverse size of domains which are injected into the membrane. In addition to this, entire rafts are stochastically removed from the membrane with a constant rate j_{off} (a number-per-time) irrespective of their size, together with an explicit size-dependent outward flux, where the raft removal rate f_{off} is exponentially small for domains of size less than a characteristic area $a_c := (\omega\lambda_c)^{-1}$. Thus, this size dependence dictates whether one recycles only at large or small scales through the sign choice of f_{off}, as shown in Figure 5.1 (the former scenario is perhaps of greater biological relevance, due to the typical size associated with the endosomes, which are mainly enriched in the phase separated component [203]).

In the next section, to gain some familiarity with the solution of the master equation (5.1), first we focus on size-independent recycling schemes, namely $f_{\text{off}} = 0$, or equivalently, the critical size $a_c \to \infty$ (later, in Section 5.3, we explore the size-dependent case).

5.2.1 Scale-free Recycling Scheme

Here, we consider a recycling scheme of the form (5.2) with a vanishing size-dependent flux. Therefore, the recycling term $\mathcal{R}(a,t)$ in the master equation (5.1) reduces to

$$\mathcal{R}(a,t) = j_{\text{on}}\,\omega\exp(-a\,\omega) - j_{\text{off}}\,\mathcal{P}(a,t), \tag{5.3}$$

which allows us to rewrite the governing equation as follows:

$$\frac{\mathrm{d}\tilde{\mathcal{P}}}{\mathrm{d}\tau} = J_{\text{on}}\exp(-s) - J_{\text{off}}\,\tilde{\mathcal{P}}(s,\tau) - \tilde{\mathcal{P}}(s,\tau)\int_0^\infty \tilde{\mathcal{P}}\big(s',\tau\big)\,\mathrm{d}s' + \frac{1}{2}\int_0^s \tilde{\mathcal{P}}\left(s',\tau\right)\,\tilde{\mathcal{P}}\left(s-s',\tau\right)\mathrm{d}s', \tag{5.4}$$

where we define the following non-dimensionalised quantities: $s = a\,\omega$, $\tau = t\,\omega D$, $J_{\text{on}} = j_{\text{on}}/\left(\omega^2 D\right)$, $J_{\text{off}} = j_{\text{off}}/\left(\omega\,D\right)$, and $\tilde{\mathcal{P}}(s,\tau) = \mathcal{P}(s,\tau)/\,\omega^2$.

This integro-differential equation can be analytically solved in the Laplace transform space [49], namely

$$\hat{\mathcal{P}}(\lambda,\tau) = \mathcal{L}_s\{\tilde{\mathcal{P}}(s,\tau)\} = \int_0^\infty \tilde{\mathcal{P}}(s,\tau)\,e^{-s\,\lambda}\,\mathrm{d}s, \tag{5.5}$$

which yields that

$$\frac{\mathrm{d}\hat{\mathcal{P}}}{\mathrm{d}\tau} = \frac{J_{\text{on}}}{1+\lambda} - J_{\text{off}}\,\hat{\mathcal{P}}(\lambda,\tau) - \rho\,(\tau)\,\hat{\mathcal{P}}(\lambda,\tau) + \frac{1}{2}\,\hat{\mathcal{P}}^2(\lambda,\tau)\,, \tag{5.6}$$

where the function $\rho(\tau) := \hat{\mathcal{P}}(\lambda = 0, \tau)$ is the total number-per-area of domains (that is rescaled by ω). Thus, by evaluating (5.6) at $\lambda = 0$, we have that

$$\frac{\mathrm{d}\rho}{\mathrm{d}\tau} = J_{\mathrm{on}} - J_{\mathrm{off}}\,\rho(\tau) - \frac{1}{2}\,\rho^2(\tau), \tag{5.7}$$

which can be solved by identifying the right-hand side of the equation as a quadratic form in $\rho\,(\tau)$, that is,

$$\frac{\mathrm{d}\rho}{\mathrm{d}\tau} = -\frac{1}{2}\,(\rho - \rho_+)(\rho - \rho_-)\,, \tag{5.8}$$

where the constants $\rho_\pm$ are given by $\rho_\pm = -J_{\mathrm{off}} \pm \sqrt{J_{\mathrm{off}}^2 + 2J_{\mathrm{on}}}$.

In order to find $\hat{\mathcal{P}}(\lambda, \tau)$, we define a new function $\psi(\lambda, \tau) = \rho(\tau) - \hat{\mathcal{P}}(\lambda, \tau)$, which by direct substitution into (5.6) gives the following differential equation:

$$\frac{\mathrm{d}\psi}{\mathrm{d}\tau} = \frac{J_{\mathrm{on}}\lambda}{1+\lambda} - J_{\mathrm{off}}\,\psi(\lambda, \tau) - \frac{1}{2}\psi^2(\lambda, \tau), \tag{5.9}$$

which depends only on ψ and has the same form as equation (5.7). Consequently, using $\rho_0 = \rho(\tau = 0)$ and $\psi_0(\lambda) = \psi(\lambda, \tau = 0)$ as boundary conditions, the solutions to (5.7) and (5.9) are found to be

$$\rho(\tau) = \mathcal{Q}_\infty\,\frac{(\rho_0 + J_{\mathrm{off}}) + \mathcal{Q}_\infty \tanh\left[\dfrac{\tau\mathcal{Q}_\infty}{2}\right]}{(\rho_0 + J_{\mathrm{off}})\tanh\left[\dfrac{\tau\mathcal{Q}_\infty}{2}\right] + \mathcal{Q}_\infty} - J_{\mathrm{off}}, \tag{5.10}$$

and

$$\psi(\lambda, \tau) = \mathcal{Q}(\lambda)\,\frac{(\psi_0(\lambda) + J_{\mathrm{off}}) + \mathcal{Q}(\lambda)\tanh\left[\dfrac{\tau\mathcal{Q}(\lambda)}{2}\right]}{(\psi_0(\lambda) + J_{\mathrm{off}})\tanh\left[\dfrac{\tau\mathcal{Q}(\lambda)}{2}\right] + \mathcal{Q}(\lambda)} - J_{\mathrm{off}}, \tag{5.11}$$

respectively, where $\mathcal{Q}_\infty = \sqrt{J_{\mathrm{off}}^2 + 2J_{\mathrm{on}}}$ and the function $\mathcal{Q}(\lambda)$ is defined by

$$\mathcal{Q}(\lambda) = \sqrt{J_{\mathrm{off}}^2 + \frac{2\lambda J_{\mathrm{on}}}{1+\lambda}}. \tag{5.12}$$

Hence, the exact form of the solutions (5.10) and (5.11) in the steady state regime (or, equivalently, in the large time limit) are given by

$$\rho_\infty := \lim_{\tau\to\infty}\rho(\tau) = \mathcal{Q}_\infty - J_{\mathrm{off}}, \quad \text{and} \quad \psi_\infty(\lambda) := \lim_{\tau\to\infty}\psi(\lambda, \tau) = \mathcal{Q}(\lambda) - J_{\mathrm{off}}, \tag{5.13}$$

respectively. Moreover, the inverse Laplace transform of $\hat{\mathcal{P}}(\lambda, \tau) = \rho(\tau) - \psi(\lambda, \tau)$

yields the domain size distribution function $\tilde{\mathcal{P}}(s,\tau)$; however, a closed-form solution to this is not generally easy to calculate and therefore numerical methods would need to be employed. Instead, we consider the limiting case $\tau \to \infty$, namely the steady state distribution $\tilde{\mathcal{P}}_\infty(s)$, where an exact solution can be obtained. Using (5.13), we have that

$$\tilde{\mathcal{P}}_\infty(s) = \mathcal{L}_\lambda^{-1}\{\mathcal{Q}_\infty - \mathcal{Q}(\lambda)\}\,, \tag{5.14}$$

where $\mathcal{L}_\lambda^{-1}\{\cdot\}$ is the inverse Laplace transform with λ as the transform variable, namely

$$\mathcal{L}_\lambda^{-1}\{F(\lambda)\} = \frac{1}{2\pi i}\int_{c-i\infty}^{c+i\infty} e^{s\lambda}F(\lambda)\,\mathrm{d}\lambda, \tag{5.15}$$

where the integration is evaluated along the line $\Re\,[s] = c$ in the complex plane such that c is greater than the real part of all singularities of $F\,(\lambda)$ [49]. However, this Bromwich integration can be avoided by rewriting the expression inside the curly brackets of (5.14) as a product of two new functions given by

$$\bar{f}(\lambda) = \sqrt{\frac{J_{\mathrm{on}}}{(1+\lambda)\,\Omega}} \quad \text{and} \quad \bar{g}(\lambda) = \sqrt{1+\lambda} - \sqrt{1+\lambda-2\,\Omega} \tag{5.16}$$

where Ω is defined by

$$\Omega = \frac{J_{\mathrm{on}}}{J_{\mathrm{off}}^2 + 2J_{\mathrm{on}}}, \tag{5.17}$$

and their inverse Laplace transforms $f(s) := \mathcal{L}_\lambda^{-1}\big\{\bar{f}(\lambda)\big\}$ and $g(s) := \mathcal{L}_\lambda^{-1}\{\bar{g}(\lambda)\}$ are known to be

$$f(s) = e^{-s}\sqrt{\frac{J_{\mathrm{on}}}{s\,\pi\,\Omega}} \quad \text{and} \quad g(s) = \frac{e^{-s}\left(e^{2s\Omega}-1\right)}{2\sqrt{\pi}\,s^{3/2}}, \tag{5.18}$$

respectively. By employing the convolution theorem [49], we have that the inverse Laplace transform $\mathcal{L}_\lambda^{-1}\big\{\bar{f}(\lambda)\,\bar{g}(\lambda)\big\} = (f\star g)\,(s)$, where the convolution $(f\star g)$ is defined by the integral

$$(f\star g)\,(s) = \int_0^s f\big(s-s'\big)\,g\big(s'\big)\,\mathrm{d}s'. \tag{5.19}$$

By substituting (5.18) into equation (5.19), a closed-form solution to the steady-state distribution $\tilde{\mathcal{P}}_\infty(s)$ can be derived, namely

$$\tilde{\mathcal{P}}_\infty(s) = \frac{J_{\mathrm{on}}}{\mathcal{Q}_\infty}\,e^{-s(1-\Omega)}\big[I_0\,(s\,\Omega) - I_1\,(s\,\Omega)\big] \sim \frac{e^{-s(J_{\mathrm{off}}/\mathcal{Q}_\infty)^2}}{s^{3/2}}\sqrt{\frac{J_{\mathrm{on}}}{8\pi\Omega^2}}\,, \tag{5.20}$$

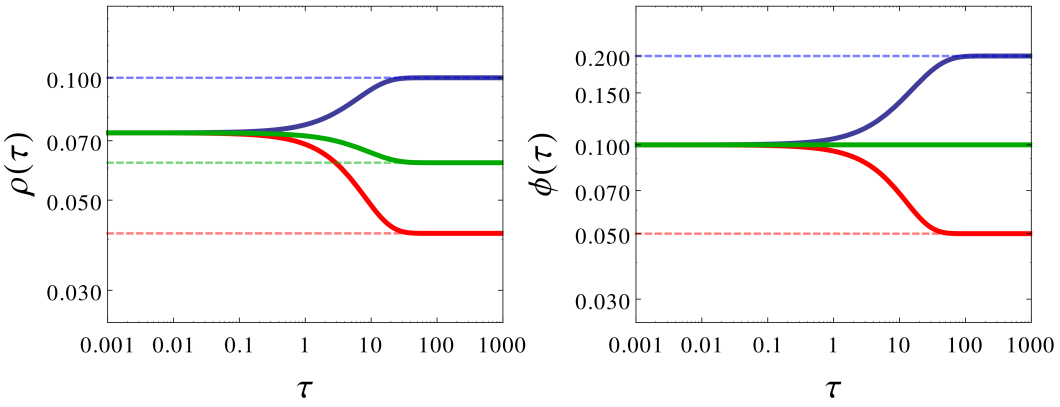

Figure 5.2: Plots of the total number-per-area of domains $\rho(\tau)$ and their area fraction $\phi(\tau)$, where we choose $J_{\text{on}} = 10^{-3}$ and $J_{\text{off}} = 10^{-1}$. The initial boundary conditions at $\tau = 0$ are given by the following step-like changes: 50% decrease in J_{off} (blue); 50% decrease in J_{on} (red); and 50% decrease in both J_{on} and J_{off} (green).

where I_1 and I_0 are the modified Bessel functions of the first kind of order one and zero, respectively. Also, the second expression in (5.20) represents the lowest order term in the asymptotic expansion as the domain size $s \to \infty$. Furthermore, in the opposite limit, when $s \to 0$, we have that $\mathcal{P}_\infty(0) = J_{\text{on}}/\mathcal{Q}_\infty$.

5.2.2 Dynamics of Lowest Moments

Though it has not been possible to find a simple form for the time dependence of $\tilde{\mathcal{P}}(s,\tau)$, its lowest (central) moments are readily obtained. The expressions for the first and second moment of $\tilde{\mathcal{P}}(s,\tau)$ can be found by differentiating $\hat{\mathcal{P}}(\lambda,\tau)$ with respect to λ under the integral sign and then evaluating the expression at $\lambda = 0$, that is,

$$\phi(\tau) := \int_0^\infty s\,\tilde{\mathcal{P}}(s,\tau)\,\mathrm{d}s = -\left.\frac{\mathrm{d}\hat{\mathcal{P}}}{\mathrm{d}\lambda}\right|_{\lambda=0}, \tag{5.21}$$

$$\sigma(\tau) := \int_0^\infty s^2\,\tilde{\mathcal{P}}(s,\tau)\,\mathrm{d}s = \left.\frac{\mathrm{d}^2\hat{\mathcal{P}}}{\mathrm{d}\lambda^2}\right|_{\lambda=0}. \tag{5.22}$$

Therefore, by substituting the expression of $\hat{\mathcal{P}}(\lambda,\tau)$ as given by the difference of (5.10) and (5.11) into the above equations, the total area fraction of domains $\phi(\tau)$ is found to be

$$\phi(\tau) = \frac{J_{\text{on}}}{J_{\text{off}}}\left[1 - e^{-\tau J_{\text{off}}}\left(1 - \frac{J_{\text{off}}}{J_{\text{on}}}\,\phi_0\right)\right], \tag{5.23}$$

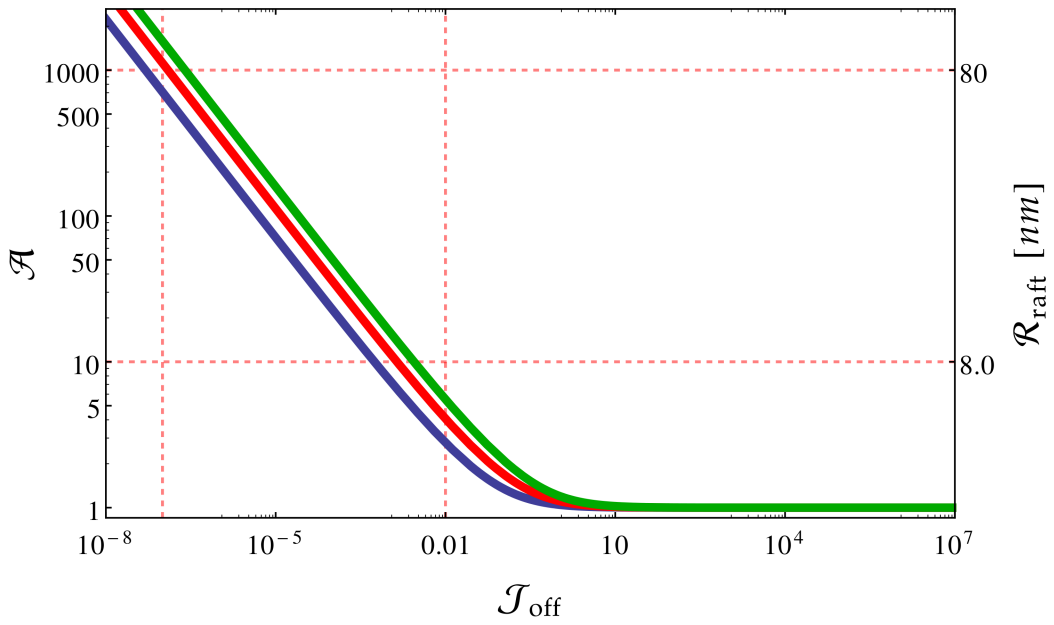

Figure 5.3: Log-log plot of the the steady state value of the dimensionless mean domain size $\mathcal{A} := \phi_\infty/\rho_\infty$, and its associated average domain radius $\mathcal{R}_{\rm raft}$ in nanometers, as a function of the recycling strength at a fixed area coverage: 10% (blue); 20% (red); and 50% (green). Here, the red dashed lines represent the upper and lower bounds of the physiological values of $J_{\rm off}$ and $\mathcal{R}_{\rm raft}$, which shows that the mean domain size is intermediate for a large interval of recycling removal rates.

where $\phi_0 = \frac{\rm d}{{\rm d}\lambda}\psi_0(\lambda = 0)$, while the second moment $\sigma(\tau)$ is given by

$$\sigma(t) = \frac{J_{\rm on}\left(J_{\rm on} + 2J_{\rm off}^2\right)}{J_{\rm off}^3} - \frac{e^{-2\tau J_{\rm off}}\left(J_{\rm on} - \phi_0\, J_{\rm off}\right)^2}{J_{\rm off}^3}$$
$$+ \frac{e^{-\tau J_{\rm off}}}{J_{\rm off}^2}\left[J_{\rm off}\left(2J_{\rm on}(\tau\phi_0 - 1) + \phi_0^2\right) - 2J_{\rm on}(\tau J_{\rm on} + \phi_0)\right] - \sigma_0\, e^{-\tau J_{\rm off}}, \quad (5.24)$$

where we define $\sigma_0 = \frac{{\rm d}^2}{{\rm d}\lambda^2}\psi_0(\lambda = 0)$. As the time $\tau \to \infty$ the area fraction ϕ decays exponentially to its steady-state value $\phi_\infty = J_{\rm on}/J_{\rm off}$ with a constant rate $J_{\rm off}$. Similarly, the second moment σ exhibits an exponential decrease (with $J_{\rm off}$ as the longest decay constant) that tends to a constant σ_∞ given by the first term in (5.24).

Although the time evolution of the central moments ρ, ϕ and σ are given in terms of the initial arbitrary parameters ρ_0, ϕ_0 and σ_0, these boundary terms can be fixed by considering a scenario where a step-change at $t = 0$ is made in either $J_{\rm on}$ or $J_{\rm off}$ after the system has reached its steady state configuration (such an assay could plausibility be performed experimentally by up-regulating or knocking down key elements of the synthesis or endocytic pathway). This corresponds to an initial-

value problem where $\{\rho_0,\, \phi_0,\, \sigma_0\} \mapsto \{\rho_\infty,\, \phi_\infty,\, \sigma_\infty\}$, while the coefficients $J_{\rm on}$ and $J_{\rm off}$ are rescaled by a constant factor, namely

$$J_{\rm on} \mapsto \beta\, J_{\rm on} \quad \text{and} \quad J_{\rm off} \mapsto \alpha\, J_{\rm off}, \tag{5.25}$$

where α and β are some positive real numbers, leading to a reduction or an increase in the recycling rates if they are less or greater than one, respectively (see Figure 5.2).

Moreover, from these central moments the average domain size can be computed from the ratio $\phi(\tau)/\rho(\tau)$, and its steady state value at fixed area coverage is shown in Figure 5.3 as a function the recycling removal rate $J_{\rm off}$. This shows that small finite size domains can be obtained within this model as non-equilibrium steady state structures which are stabilised by membrane recycling.

5.3 Size-dependent Membrane Recycling

We now consider the size-dependent recycling scheme given by (5.2) with $f_{\rm off} \neq 0$, so that the raft removal rate is exponentially small for domains of size less than a characteristic area $a_c = (\omega\lambda_c)^{-1}$, namely

$$\mathcal{R}(a,t) = j_{\rm on}\,\omega \exp(-a\,\omega) - j_{\rm off}\,\mathcal{P}(a,t) - f_{\rm off}\left[1 - \exp\left(-a\,\omega\lambda_c\right)\right]\mathcal{P}(a,t), \tag{5.26}$$

which reduces to the previous size-independent scheme (5.3) in the limit of $\lambda_c \to \infty$.

Therefore, by Laplace transforming the governing equation (5.1) and non-dimensionalising as done in equation (5.6), explicitly $s = a\,\omega$, $\tau = t\,\omega D$, and $\tilde{\mathcal{P}}(s,\tau) = \mathcal{P}(s,\tau)\,/\,\omega^2$, then we have that

$$\frac{{\rm d}\hat{\mathcal{P}}}{{\rm d}\tau} = \frac{J_{\rm on}}{1+\lambda} - F_{\rm off}\left[\hat{\mathcal{P}}(\lambda,\tau) - \hat{\mathcal{P}}(\lambda_c+\lambda,\tau)\right] - \left[J_{\rm off} + \rho\,(\tau)\,\right]\hat{\mathcal{P}}(\lambda,\tau) + \frac{\hat{\mathcal{P}}^2(\lambda,\tau)}{2}, \tag{5.27}$$

where $\rho(\tau) := \hat{\mathcal{P}}(\lambda = 0,\, \tau)$ and $\hat{\mathcal{P}}(\lambda,\tau) := \mathcal{L}_s\{\tilde{\mathcal{P}}(s,\tau)\}$ as before. Moreover, we set the coefficients $J_{\rm on} = j_{\rm on}\,/\left(\omega^2 D\right)$, $J_{\rm off} = j_{\rm off}\,/\,(\omega\, D)$, and $F_{\rm off} = f_{\rm off}\,/\,(\omega\, D)$.

Unlike the previous results obtained for the size-independent case, the time evolution even of the central moments is more difficult to determine analytically from the governing equation (5.27). Thus, we first obtain an analytic solution for the steady state distribution $\hat{\mathcal{P}}_\infty\,(\lambda) := \lim\limits_{\tau\to\infty} \hat{\mathcal{P}}(\lambda,\tau)$ and its associated lowest moments, and then study the time dependence of small perturbation about these solutions.

5.3.1 Steady State Solutions

First, we consider the steady-state distribution $\hat{\mathcal{P}}_\infty(\lambda)$, which is found to satisfy the following equation:

$$\frac{J_{\text{on}}}{1+\lambda} - F_{\text{off}}\left[\hat{\mathcal{P}}_\infty(\lambda) - \hat{\mathcal{P}}_\infty(\lambda_c+\lambda)\right] - (\rho_\infty + J_{\text{off}})\,\hat{\mathcal{P}}_\infty(\lambda) + \frac{1}{2}\,\hat{\mathcal{P}}_\infty^2(\lambda) = 0, \quad (5.28)$$

where ρ_∞ is the corresponding steady-state value for the total number of domains per unit area. In order to self-consistently solve for both ρ_∞ and $\hat{\mathcal{P}}_\infty(\lambda)$, we assume that the rate λ_c is small, that is, $\lambda_c \ll 1$. This allows us to rewrite (5.28) as

$$K_{\text{off}}\frac{\mathrm{d}}{\mathrm{d}\lambda}\hat{\mathcal{P}}_\infty(\lambda) - (\rho_\infty + J_{\text{off}})\,\hat{\mathcal{P}}_\infty(\lambda) + \frac{1}{2}\,\hat{\mathcal{P}}_\infty^2(\lambda) + \frac{J_{\text{on}}}{1+\lambda} = 0, \quad (5.29)$$

which is the lowest order in a Taylor expansion in λ_c, and $K_{\text{off}} = \lambda_c J_{\text{off}}$. Thus, by evaluating equation (5.29) at $\lambda = 0$, the total number of domains ρ_∞ is found to satisfy the following equation:

$$\frac{1}{2}\,\rho_\infty^2 = J_{\text{on}} - J_{\text{off}}\,\rho_\infty + K_{\text{off}}\left.\frac{\mathrm{d}\hat{\mathcal{P}}_\infty}{\mathrm{d}\lambda}\right|_{\lambda=0}. \quad (5.30)$$

By setting $\hat{\mathcal{P}}_\infty(\lambda) = 2K_{\text{off}}\,\mathcal{F}'(\lambda)/\mathcal{F}(\lambda)$ in equation (5.29), with $\mathcal{F}(\lambda)$ some function to be determined subsequently, we have

$$\mathcal{F}''(\lambda) - \frac{\rho_\infty + J_{\text{off}}}{K_{\text{off}}}\,\mathcal{F}'(\lambda) + \frac{J_{\text{on}}}{2K_{\text{off}}^2\,(1+\lambda)}\,\mathcal{F}(\lambda) = 0, \quad (5.31)$$

where the (double) prime symbol represents a (second) derivative with respect to the argument of the function. By defining

$$\kappa := \frac{J_{\text{on}}}{2\,(\rho_\infty + J_{\text{off}})\,K_{\text{off}}} \qquad \text{and} \qquad z := \frac{(1+\lambda)(\rho_\infty + J_{\text{off}})}{K_{\text{off}}}, \quad (5.32)$$

equation (5.31) reduces to

$$z\,\mathcal{F}''(z) + (\nu + 1 - z)\,\mathcal{F}'(z) + \kappa\,\mathcal{F}(z) = 0, \quad (5.33)$$

which is a special case of the more general associated Laguerre differential equation with $\nu = -1$ [168], and its solution is given in terms of the confluent hypergeometric function of the second kind $U(-\kappa;\,1+\nu;\,z)$, also known as a Tricomi function, and

the generalized Laguerre function $L(\kappa;\, \nu;\, z)$ [168], namely

$$\mathcal{F}(z) = \mathcal{C}_1\, U(-\kappa;\, 0;\, z) + \mathcal{C}_2\, L\,(\kappa;\, -1;\, z), \tag{5.34}$$

where $\mathcal{C}_1$ and $\mathcal{C}_2$ are arbitrary constants, and the corresponding Wronskian is given by $W = e^z \sin(\pi\kappa)\,\Gamma(\kappa)/\pi$, with Γ as the gamma function. By using the derivative identities $\frac{\partial}{\partial z} L\,(\kappa;\, -1;\, z) = -L\,(\kappa - 1;\, 0;\, z)$ and $\frac{\partial}{\partial z} U(-\kappa;\, 0;\, z) = \kappa\, U(1-\kappa;\, 1;\, z)$, the solution to (5.29) is found to be

$$\hat{\mathcal{P}}_\infty(\lambda) = \frac{J_{\text{on}}}{\kappa K_{\text{off}}}\, \frac{\mathcal{C}_1\, \kappa\, U(1-\kappa;\, 1;\, z) - \mathcal{C}_2\, L\,(\kappa - 1;\, 0;\, z)}{\mathcal{C}_1\, U(-\kappa;\, 0;\, z) + \mathcal{C}_2\, L\,(\kappa;\, -1;\, z)}. \tag{5.35}$$

To find a unique solution, we impose the condition that $\lim\limits_{\lambda\to\infty} \hat{\mathcal{P}}_\infty(\lambda) = 0$, which is a *de facto* condition for the existence of the Laplace transform. This yields

$$\hat{\mathcal{P}}_\infty(\lambda) = \frac{J_{\text{on}}\, U\Big(1-\kappa;\, 1;\, (1+\lambda)(\rho_\infty + J_{\text{off}})\,/\,K_{\text{off}}\Big)}{K_{\text{off}}\, U\Big(-\kappa;\, 0;\, (1+\lambda)(\rho_\infty + J_{\text{off}})\,/\,K_{\text{off}}\Big)}, \tag{5.36}$$

where we assume that $\kappa \notin \mathbb{Z}$ and $\mathcal{C}_2 = 0$ is used to remove the divergent terms when λ tends to infinity. Figure 5.4 shows a comparison between the steady-state distribution in (5.36) and the distribution computed in the size-independent case. Although this solution is written in terms of the (undetermined) constant ρ_∞, its value can be obtained by using the boundary condition $\rho_\infty = \hat{\mathcal{P}}_\infty(\lambda = 0)$, or equivalently, by substituting (5.36) into (5.30), leading to the following characteristic equation:

$$\mathcal{V}\,(\kappa) := \frac{1}{2} + \kappa\,\mathcal{K} - \frac{U(-\kappa;\, 1;\, \mathcal{J}/\kappa\,)}{U(-\kappa;\, 0;\, \mathcal{J}/\kappa\,)} = 0, \tag{5.37}$$

where the contiguous relations of the confluent hypergeometric function of the second kind are employed [168] and the constants $\mathcal{J}$ and $\mathcal{K}$ are defined by

$$\mathcal{J} = \frac{J_{\text{on}}}{2\,K_{\text{off}}^2} \qquad \text{and} \qquad \mathcal{K} = \frac{J_{\text{off}}\, K_{\text{off}}}{J_{\text{on}}}, \tag{5.38}$$

respectively. This allows us to determine the total number-per-area of domains through the equation $\rho_\infty = J_{\text{on}}\,/\,(2\kappa K_{\text{off}}) - J_{\text{off}}$, where κ is given by the positive zeros of $\mathcal{V}\,(\kappa)$. Although (5.37) has an infinite number of real roots, the first positive zero yields the physically relevant solution that is commensurate with the approximation $\lambda_c \ll 1$. This can be shown by expressing the function $\mathcal{V}\,(\kappa)$ as a power series in the parameter $\varepsilon = \kappa^2/\mathcal{J}$ (which is independent of λ_c to lowest order) and using the

asymptotic expansion of the confluent hypergeometric function U to give

$$\mathcal{V}(\kappa) = \frac{1}{2} + \sum_{n=0}^{\infty} C_n \, \varepsilon^{n+1} - \frac{J_{\text{off}}}{\sqrt{2J_{\text{on}}}} \varepsilon^{1/2} + \mathcal{O}\big[\lambda_c\big], \tag{5.39}$$

where C_n are the Catalan numbers [210]. Hence, using the generating function for the Catalan numbers, namely $\sum_{n=0}^{\infty} C_n \varepsilon^n = \left(1 - \sqrt{1-4\varepsilon}\,\right) / (2\varepsilon)$, (5.39) reduces to

$$\frac{1}{2}\sqrt{1 - \frac{2J_{\text{on}}}{(\rho_\infty + J_{\text{off}})^2}} - \frac{J_{\text{off}}}{2\,(\rho_\infty + J_{\text{off}})} + \mathcal{O}\big[\lambda_c\big] = 0, \tag{5.40}$$

which implies that the total number-per-area of domains $\rho_\infty^{(0)} = \sqrt{J_{\text{off}}^2 + 2J_{\text{on}}} - J_{\text{off}}$ by solving the quadratic-like equation from above, or equivalently,

$$\kappa^{(0)} = \frac{1}{2}\left(\mathcal{K}^2 + \frac{1}{\mathcal{J}}\right)^{-1/2} \tag{5.41}$$

using the definition of κ as given by (5.32). This value corresponds to the case where the size-dependent raft removal rate f_{off} vanishes, and it is consistent with the solution of (5.28) when $\lambda = \lambda_c = 0$ (as given by equation (5.13) in the previous section). As a result, $\kappa^{(0)}$ provides an order of magnitude estimate to the *physical* value of κ (that solves exactly the characteristic equation $\mathcal{V}(\kappa) = 0$), which is found to be in the vicinity of the first positive zero of $\mathcal{V}\,(\kappa)$ for small values of λ_c.

The equations (5.36) and (5.37) determine entirely the steady-state distribution $\mathcal{P}_\infty(s)$ which can be obtained by numerically inverse Laplace transforming $\hat{\mathcal{P}}_\infty(\lambda)$. As analogous to the expansion in (5.39), an approximate solution to $\hat{\mathcal{P}}_\infty(\lambda)$ can be found by expanding (5.36) to first order in λ_c. Thus, by noting that ρ_∞ is itself a function of λ_c at this order of the expansion, we find that

$$\begin{aligned}\hat{\mathcal{P}}_\infty(\lambda) = 2\left(\rho_\infty^{(0)} + J_{\text{off}}\right)\sum_{n=0}^{\infty} C_n \left(\frac{\varepsilon^{(0)}}{1+\lambda}\right)^{n+1} - \frac{\lambda_c F_{\text{off}}}{4J_{\text{on}}}\left(\rho_\infty^{(0)} + J_{\text{off}}\right)^2 \sum_{n=0}^{\infty}\left(\frac{4\varepsilon^{(0)}}{1+\lambda}\right)^{n+2} \\ - \lambda_c \sum_{n=0}^{\infty}(n+2)\, C_{n+1}\left(\frac{\varepsilon^{(0)}}{1+\lambda}\right)^{n+1} \left.\frac{\mathrm{d}\rho_\infty}{\mathrm{d}\lambda_c}\right|_{\lambda_c=0} + \mathcal{O}\big[\lambda_c^2\big],\end{aligned} \tag{5.42}$$

where we define $\varepsilon^{(0)} = \big[\kappa^{(0)}\big]^2/\mathcal{J}$. Each sum can be computed exactly and the derivative of ρ_∞ with respect to λ_c in (5.42) can be obtained by applying the boundary

condition that $\rho_\infty = \hat{\mathcal{P}}_\infty(\lambda = 0)$, which yields that

$$\hat{\mathcal{P}}_\infty(\lambda) = \mathcal{Q}_\infty - \mathcal{Q}(\lambda) + \frac{J_{\text{on}} K_{\text{off}}}{J_{\text{off}} \mathcal{Q}(\lambda)} \left[\frac{\mathcal{Q}_\infty - \mathcal{Q}(\lambda)}{\mathcal{Q}(\lambda)\, \mathcal{Q}_\infty} - \frac{J_{\text{off}}}{(1+\lambda)^2\, \mathcal{Q}(\lambda)} \right] + \mathcal{O}\big[\lambda_c^2\big], \quad (5.43)$$

where $\mathcal{Q}_\infty$ and $\mathcal{Q}(\lambda)$ are given by

$$\mathcal{Q}_\infty = \sqrt{J_{\text{off}}^2 + 2J_{\text{on}}} \quad \text{and} \quad \mathcal{Q}(\lambda) = \sqrt{J_{\text{off}}^2 + \frac{2\lambda J_{\text{on}}}{1+\lambda}}, \quad (5.44)$$

respectively, as previously defined in (5.12). Therefore, the total number-per-area of rafts within this approximation can be written as

$$\rho_\infty \approx \sqrt{J_{\text{off}}^2 + 2J_{\text{on}}} - J_{\text{off}} - \frac{J_{\text{on}} K_{\text{off}}}{J_{\text{off}} \sqrt{J_{\text{off}}^2 + 2J_{\text{on}}}}. \quad (5.45)$$

Moreover, using that $\mathcal{L}_\lambda^{-1}\{(1+\lambda)^{-n}\} = s^{n-1} e^{-s}/(n-1)!$ and the series representation of the modified Bessel functions of the first kind I_0 and I_1 [168], namely

$$\sum_{n=0}^{\infty} \frac{C_n\, x^n}{n!} = e^{2x} \left[I_0(2x) - I_1(2x) \right], \quad (5.46)$$

the approximate solution in (5.42) can be inverse Laplace transformed to give

$$\begin{aligned} \tilde{\mathcal{P}}_\infty(s) = & \frac{J_{\text{on}}}{\mathcal{Q}_\infty} e^{-s(1-\Omega)} \left[\left(1 + \frac{J_{\text{on}} K_{\text{off}}}{J_{\text{off}}\, \mathcal{Q}_\infty^2} \right) I_0(s\,\Omega) - \left(1 - \frac{J_{\text{on}} K_{\text{off}}}{J_{\text{off}}\, \mathcal{Q}_\infty^2} \right) I_1(s\,\Omega) \right] \\ & - K_{\text{off}}\, e^{-s(1-\Omega)} \sinh(s\,\Omega) + \mathcal{O}\big[\lambda_c^2\big], \end{aligned} \quad (5.47)$$

where the parameter Ω is defined by equation (5.17) in the preceding section.

The steady-state values of the first and second (central) moment of the distribution $\tilde{\mathcal{P}}(s, \tau)$ can be determined by substituting (5.36) into their definitions (5.21). This gives the steady-state area fraction of domains as

$$\phi_\infty = \frac{2J_{\text{on}} - 2\rho_\infty J_{\text{off}} - \rho_\infty^2}{2\, K_{\text{off}}} \approx \frac{J_{\text{on}}}{J_{\text{off}}} - \frac{J_{\text{on}} K_{\text{off}} \big(J_{\text{on}} + 2J_{\text{off}}^2 \big)}{J_{\text{off}}^4}, \quad (5.48)$$

which is consistent with (5.30), while the second moment σ_∞ is found to be

$$\sigma_\infty = \frac{J_{\text{on}} - \phi_\infty J_{\text{off}}}{K_{\text{off}}} \approx \frac{J_{\text{on}} \big(J_{\text{on}} + 2J_{\text{off}}^2 \big)}{J_{\text{off}}^3} - \frac{J_{\text{on}} K_{\text{off}} \big(6J_{\text{off}}^4 + 10\, J_{\text{on}} J_{\text{off}}^2 + 5J_{\text{on}}^2 \big)}{J_{\text{off}}^6}, \quad (5.49)$$

which can also be derived by differentiating (5.29) with respect to λ and subsequently

evaluating at $\lambda = 0$. In addition, the approximations in (5.48) and (5.49) are computed, respectively, through the first and second derivatives (at $\lambda = 0$) of the approximate distribution $\hat{\mathcal{P}}_\infty(\lambda)$ as given by equation (5.43). These low moments are in principle experimentally measurable, and therefore it allows us to estimate the values of the parameters J_{on}, J_{off}, and K_{off} by simultaneously solving (5.45), (5.48), and (5.49). Other measurable quantities are the relaxation times of the moments, which can be estimated, in principle, by comparison with the experiments. Thus, in the next section, we study the linearised dynamics about the steady state.

5.3.2 Linearised Dynamics

In contrast to the size-independent case, the dynamics of the central moments with size-dependent recycling is more difficult to determine analytically from the master equation (5.27). However, the long-time evolution can be obtained by employing a perturbation theory about the steady-state solutions – namely, we assume that

$$\rho(\tau) = \rho_\infty + \epsilon\, \delta\rho(\tau) \quad \text{and} \quad \hat{\mathcal{P}}(\lambda, \tau) = \hat{\mathcal{P}}_\infty(\lambda) + \epsilon\, \delta\hat{\mathcal{P}}(\lambda, \tau), \tag{5.50}$$

with $\delta\rho(\tau) = \delta\hat{\mathcal{P}}(\lambda = 0,\, \tau)$, which by direct substitution into (5.27) yields that

$$\begin{aligned}\frac{\mathrm{d}}{\mathrm{d}\tau}\delta\hat{\mathcal{P}}(\lambda, \tau) = K_{\text{off}}\, \frac{\mathrm{d}}{\mathrm{d}\lambda}\delta\hat{\mathcal{P}}(\lambda, \tau) - (\rho_\infty + J_{\text{off}})\, \delta\hat{\mathcal{P}}(\lambda, \tau) \\ - \delta\rho(\tau)\, \hat{\mathcal{P}}_\infty(\lambda) + \delta\hat{\mathcal{P}}(\lambda, \tau)\, \hat{\mathcal{P}}_\infty(\lambda)\end{aligned} \tag{5.51}$$

to lowest order in the (small) perturbation parameter ϵ (neglecting the quadratic terms). This equation can be solved by Laplace transforming in time, that is, $\varphi(\lambda, \mu) = \int_0^\infty \delta\hat{\mathcal{P}}(\lambda, \tau)\, e^{-\mu\tau}\, \mathrm{d}\tau$, which gives

$$K_{\text{off}}\, \frac{\mathrm{d}}{\mathrm{d}\lambda}\varphi(\lambda, \mu) - \Big[\mu + \rho_\infty + J_{\text{off}} - \hat{\mathcal{P}}_\infty(\lambda)\Big]\, \varphi(\lambda, \mu) = \hat{\mathcal{P}}_\infty(\lambda)\, \varphi(0, \mu) - \delta\hat{\mathcal{P}}_0(\lambda), \tag{5.52}$$

where μ is the transform variable and we define that $\delta\hat{\mathcal{P}}_0(\lambda) = \delta\hat{\mathcal{P}}(\lambda, 0)$ for brevity. By using the method of integrating factors, we find that (5.52) admits the following solution:

$$\varphi(\lambda, \mu) = e^{\gamma(\lambda,\, \mu)} \int_\lambda^\infty \frac{e^{-\gamma(\lambda',\, \mu)}}{K_{\text{off}}} \Big[\delta\hat{\mathcal{P}}_0(\lambda') - \hat{\mathcal{P}}_\infty(\lambda')\, \varphi(0, \mu)\Big]\, \mathrm{d}\lambda', \tag{5.53}$$

where the boundary condition $\lim_{\lambda\to\infty}\varphi(\lambda,\mu)=0$ is used to fix the integration constant, and $\gamma(\lambda,\mu)$ is given by

$$\gamma(\lambda,\mu)=\frac{1}{K_{\text{off}}}\int_0^{\lambda}\left[\mu+\rho_\infty+J_{\text{off}}-\hat{\mathcal{P}}_\infty\left(\lambda'\right)\right]\mathrm{d}\lambda'. \tag{5.54}$$

Equation (5.53) can be inverse Laplace transformed by exploiting the identity

$$\mathcal{L}_\mu^{-1}\left\{A(\mu)\exp\left(\mu\,\frac{\lambda-\lambda'}{K_{\text{off}}}\right)\right\}=\mathcal{L}_\mu^{-1}\left\{A(\mu)\right\}\star\delta\left(\tau+\frac{\lambda-\lambda'}{K_{\text{off}}}\right), \tag{5.55}$$

which is the convolution of the Dirac delta function δ with the inverse Laplace transform of an arbitrary function $A(\mu)$. Consequently, by employing this result with $A(\mu)=1$ or $A(\mu)=\varphi(0,\mu)$, we find

$$\begin{aligned}\delta\hat{\mathcal{P}}(\lambda,\tau)=e^{-H(\lambda,\,\tau)}\,\delta\hat{\mathcal{P}}_0(\lambda+\tau K_{\text{off}})\\ -\int_0^{\tau}e^{-H(\lambda,\,\tau')}\,\hat{\mathcal{P}}_\infty\big(\lambda+\tau' K_{\text{off}}\big)\;\delta\rho\left(\tau-\tau'\right)\mathrm{d}\tau',\end{aligned} \tag{5.56}$$

where we made the substitution $\tau'=(\lambda'-\lambda)/K_{\text{off}}$ and define the new function $H(\lambda,\tau)=\gamma(0,\lambda)-\gamma(0,\,\lambda+\tau K_{\text{off}})$, or equivalently,

$$H(\lambda,\tau)=(\rho_\infty+J_{\text{off}})\,\tau-\int_0^{\tau}\hat{\mathcal{P}}_\infty\big(\lambda+\tau' K_{\text{off}}\big)\,\mathrm{d}\tau'. \tag{5.57}$$

Because of the initial condition $\delta\rho(\tau)=\delta\hat{\mathcal{P}}(\lambda=0,\,\tau)$, the solution shown in equation (5.56) reduces, as a result, to a Volterra integral equation of second kind at $\lambda=0$, namely

$$\delta\rho(\tau)=e^{-h(\tau)}\,\delta\hat{\mathcal{P}}_0(\tau K_{\text{off}})-\int_0^{\tau}e^{-h(\tau')}\,\hat{\mathcal{P}}_\infty\big(\tau' K_{\text{off}}\big)\,\delta\rho\left(\tau-\tau'\right)\mathrm{d}\tau', \tag{5.58}$$

where the function $h(\tau)=H(\lambda=0,\,\tau)$. Since the kernel of the integral equation depends only on the difference $\tau-\tau'$, this can be solved (in principle) using a Laplace method transform, which yields in its full glory the following solution:

$$\delta\rho(\tau)=\frac{1}{2\pi i}\int_{c+i\infty}^{c-i\infty}e^{\kappa\tau}\left[\frac{\int_0^{\infty}e^{-\kappa\tau'-h(\tau')}\,\delta\hat{\mathcal{P}}_0(\tau' K_{\text{off}})\,\mathrm{d}\tau'}{1+\int_0^{\infty}e^{-\kappa\tau'-h(\tau')}\,\hat{\mathcal{P}}_\infty(\tau' K_{\text{off}})\,\mathrm{d}\tau'}\right]\mathrm{d}\kappa. \tag{5.59}$$

This includes a Bromwich integral over κ with c chosen such that it is greater than the real part of all the singularities of the function within the square brackets. By absorbing the small amplitude ϵ into the initial constants (in other words, assum-

ing that $\delta\hat{\mathcal{P}}_0(\lambda)$ is of order ϵ for all values of λ), then the time evolution of the distribution $\hat{\mathcal{P}}(\lambda,\tau)$ in the vicinity of its steady-state is described by

$$\hat{\mathcal{P}}(\lambda,\tau) = \hat{\mathcal{P}}_\infty(\lambda) + e^{-H(\lambda,\tau)}\,\delta\hat{\mathcal{P}}_0(\lambda+\tau K_{\text{off}}) - \int_0^\tau e^{-H(\lambda,\tau')}\,\hat{\mathcal{P}}_\infty\big(\lambda+\tau' K_{\text{off}}\big)\;\delta\rho\left(\tau-\tau'\right)\mathrm{d}\tau', \qquad (5.60)$$

where the boundary term $\delta\hat{\mathcal{P}}_0(\lambda')$ is found to be

$$\delta\hat{\mathcal{P}}_0(\lambda') = \hat{\mathcal{P}}(\lambda',\,\tau=0) - \hat{\mathcal{P}}_\infty(\lambda'), \qquad (5.61)$$

by imposing the boundary condition at $\tau = 0$, which can be chosen as the steady-state distribution (5.36) with the coefficients J_{on}, J_{off}, or/and K_{off} being rescaled by a constant factor. Using (5.21), this linearised solution (5.60) can now be used to attain the dynamics of the first and second moment by differentiating it with respect to λ and then setting $\lambda = 0$; however, their explicit expressions are cumbersome and for brevity they are not shown here. Instead, we study the Padé approximant solutions of the central moments, which give exact analytical results of the characteristic relaxation times when the dynamics of the system is linearised as in (5.50). This study is motivated by the numerical results obtained when comparing the exact steady state distribution in Laplace space given by (5.36) with its lowest Padé approximant solution (as shown in equation (5.67) of the next section) for some values of the free parameters (see Figure 5.4).

5.3.3 Padé Approximant Solutions

A Padé approximant of a function $f(z)$ is an approximation of that function by a fraction where its numerator and denominator are both expressed by polynomials in z, so that the power series expansion of this ratio about $z = z_0$ agrees with the power series of $f(z)$ at that point [211]. In general, the Padé approximant provides a much better approximation of the function than its truncated Taylor expansion, and it may work even when the Taylor series divergences [211].

Here, we consider a first order Padé approximant of the distribution $\hat{\mathcal{P}}(\lambda,\tau)$, such that it agrees with the power series expansion of the function in both limits of $\lambda \to 0$ and $\lambda \to \infty$. Since the total number-per-area of domains is given by $\rho(\tau) = \hat{\mathcal{P}}(\lambda = 0,\,\tau)$, and $\hat{\mathcal{P}}(\lambda,\tau)$ vanishes in limit of large λ, the Padé approximant

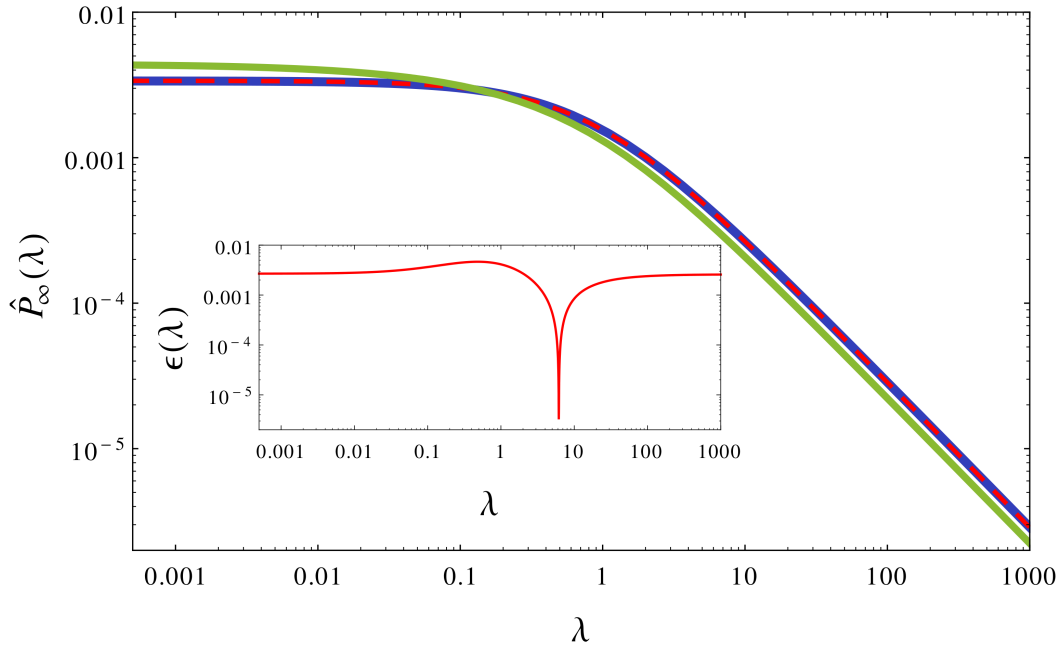

Figure 5.4: Log-log plot of the domain size distribution in Laplace space for the size-independent case (green curve) and the size-dependent case (blue curve), where the parameters $\lambda_c = 0.01$, $J_{\text{on}} = 10^{-5}$, $J_{\text{off}} = 10^{-4}$, and $F_{\text{off}} = 10^{-1}$. The red dashed line shows the steady-state solution of the Padé approximant in equation (5.67). The inset plot displays the magnitude $\epsilon(\lambda)$ of the fractional error between the blue curve and the red dashed line as function of the transform variable λ. The Padé approximant is seen to be extremely precise.

of the distribution $\hat{\mathcal{P}}(\lambda,\tau)$ can be written as the following rational approximation:

$$\hat{\mathcal{P}}(\lambda,\tau) = \frac{\rho(\tau)}{1+\lambda\eta(\tau)}, \tag{5.62}$$

which automatically satisfies the boundary conditions. By substitution into the governing equation (5.27), two coupled differential equations in terms of $\rho(\tau)$ and $\eta(\tau)$ are obtained by requiring that the leading coefficients in a series expansion as $\lambda \to 0$ and $\lambda \to \infty$ vanish identically. In other words, we impose that the distribution (5.62) is a solution to (5.27) as λ tends to either infinity or zero, which leads to

$$\rho'(\tau) + \rho(\tau)\left[J_{\text{off}} + \frac{K_{\text{off}}\,\eta(\tau)}{1+\lambda_c\eta(\tau)}\right] + \frac{\rho^2(\tau)}{2} = J_{\text{on}}, \tag{5.63}$$

and

$$J_{\text{on}}\,\eta(\tau) + \rho(\tau)\,\frac{\eta'(\tau)}{\eta(\tau)} = \rho'(\tau) + \rho(\tau)\big[\rho(\tau) + J_{\text{off}}\big], \tag{5.64}$$

respectively, where $K_{\text{off}} = \lambda_c\, J_{\text{off}}$. This allows us to find the central moments of the distribution for any value of λ_c (note that in this case there is no restriction on λ_c, as opposed to the previous section where we studied only the limiting case $\lambda_c \ll 1$). By linearizing the dynamics about the steady-state solutions, the system of equations given by (5.63) and (5.64) can be solved exactly. Therefore, we consider that

$$\rho(\tau) = \rho_\infty + \varepsilon\,\delta\rho(\tau), \quad \text{and} \quad \eta(\tau) = \eta_\infty + \varepsilon\,\delta\eta(\tau), \tag{5.65}$$

where ε is a small perturbation parameter. At the steady-state, we have that

$$\eta_\infty = \frac{\rho_\infty(J_{\text{off}} + \rho_\infty)}{J_{\text{on}}}, \tag{5.66}$$

which consequently yields the following distribution (5.62) as time $\tau \to \infty$ (its steady-state):

$$\hat{\mathcal{P}}_\infty(\lambda) = \frac{\rho_\infty J_{\text{on}}}{J_{\text{on}} + \lambda\,\rho_\infty(J_{\text{off}} + \rho_\infty)}, \tag{5.67}$$

where ρ_∞ is the steady-state value of the total number-per-area of rafts, which must satisfy the following characteristic equation:

$$\rho_\infty\left[J_{\text{off}} + \frac{\rho_\infty}{2} + \frac{\rho_\infty\lambda_c\,(J_{\text{off}} + \rho_\infty)\,F_{\text{off}}}{J_{\text{on}} + \rho_\infty\lambda_c\,(J_{\text{off}} + \rho_\infty)}\right] = J_{\text{on}}. \tag{5.68}$$

The stationary solutions of the first and second moment of the distribution (5.67) can be determined by evaluating the first and second derivative of equation

(5.67) at $\lambda = 0$, which give

$$\phi_\infty = \frac{\rho_\infty^2 (J_{\text{off}} + \rho_\infty)}{J_{\text{on}}}, \quad \text{and} \quad \sigma_\infty = \frac{2\rho_\infty^3 (J_{\text{off}} + \rho_\infty)^2}{J_{\text{on}}^2}, \tag{5.69}$$

respectively. Using equation (5.66), we find that $\phi_\infty = \rho_\infty \eta_\infty$ and $\sigma_\infty = 2\rho_\infty \eta_\infty^2$, which implies that the ratio of the central moments $\sigma_\infty / \phi_\infty = 2\eta_\infty$.

To first-order in the (small) perturbation parameter ε, the system of coupled equations (5.63) and (5.64) reduce to

$$\delta\rho'(\tau) + \left(J_{\text{off}} + \rho_\infty + \frac{K_{\text{off}}\, \eta_\infty}{1 + \lambda_c\, \eta_\infty} \right) \delta\rho(\tau) + \frac{K_{\text{off}}\, \eta_\infty}{(1 + \lambda_c\, \eta_\infty)^2}\, \delta\eta(\tau) = 0, \tag{5.70}$$

and

$$J_{\text{on}}\, \delta\eta(\tau) + \frac{\rho_\infty}{\eta_\infty}\, \delta\eta'(\tau) = \delta\rho'(\tau) + (J_{\text{off}} + 2\rho_\infty)\, \delta\rho(\tau). \tag{5.71}$$

These can be solved by differentiating (5.70) once with respect to τ, then substituting the form of $\delta\eta'(\tau)$ from equation (5.71) in terms of $\delta\eta(\tau)$ and $\delta\rho(\tau)$, and lastly eliminating $\delta\eta(\tau)$ through (5.70), which yields a homogeneous second-order differential equation with constant coefficients for $\delta\rho(\tau)$, namely

$$\delta\rho''(\tau) + 2\varphi\, \delta\rho'(\tau) + \left(\varphi^2 - \vartheta^2 \right) \delta\rho(\tau) = 0, \tag{5.72}$$

where ϑ and φ are given by

$$\vartheta^2 = \frac{(K_{\text{off}}\, \eta_\infty)^2}{(1 + \lambda_c\, \eta_\infty)^4} \left(1 + \frac{\lambda_c\, \eta_\infty}{2} \right)^2 - \frac{K_{\text{off}}\, \eta_\infty\, \rho_\infty}{(1 + \lambda_c\, \eta_\infty)^2}, \tag{5.73}$$

and

$$\varphi = \rho_\infty + J_{\text{off}} + \frac{K_{\text{off}}\, \eta_\infty}{(1 + \lambda_c\, \eta_\infty)^2} \left(1 + \frac{\lambda_c\, \eta_\infty}{2} \right), \tag{5.74}$$

respectively. Thus, equation (5.72) admits the following general solution:

$$\delta\rho(\tau) = e^{-\varphi\tau} \left[\mathcal{C}_1 \sinh(\tau\vartheta) + \mathcal{C}_2 \cosh(\tau\vartheta) \right], \tag{5.75}$$

where $\mathcal{C}_1$ and $\mathcal{C}_2$ are arbitrary constants. From the above solution, the expression of $\delta\eta(\tau)$ can be obtained through substitution into (5.70). Moreover, the unknown constants $\mathcal{C}_1$ and $\mathcal{C}_2$ can be fixed by imposing the conditions $\delta\rho_0 = \delta\rho(\tau = 0)$ and $\delta\eta_0 = \delta\eta(\tau = 0)$. These constants can be chosen as the difference between the steady-state values of $\rho(\tau)$ and $\eta(\tau)$ after and before a reduction/increase in the phenomenological parameters of the model. If we absorb the small perturbation

parameter ε into $\delta\rho_0$ and $\delta\eta_0$, then we have that time evolution of the total number-per-area of rafts is

$$\rho(\tau) = \rho_\infty + \delta\rho_0\, e^{-\tau\varphi}\left[\sinh(\tau\vartheta) - \frac{\lambda_c K_{\text{off}}\,\eta_\infty^2\cosh(\tau\vartheta)}{2\vartheta\,(1+\eta_\infty\lambda_c)^2}\right] + \delta\eta_0\, e^{-\tau\varphi}\,\frac{K_{\text{off}}\,\rho_\infty\cosh(\tau\vartheta)}{\vartheta\,(1+\eta_\infty\lambda_c)^2}, \tag{5.76}$$

while the function $\eta(\tau)$ is found to be

$$\eta(\tau) = \eta_\infty + \delta\eta_0\, e^{-\tau\varphi}\left[\sinh(\tau\vartheta) + \frac{\lambda_c K_{\text{off}}\,\eta_\infty^2\cosh(\tau\vartheta)}{2\vartheta\,(1+\eta_\infty\lambda_c)^2}\right] + \delta\rho_0\, e^{-\tau\varphi}\,\frac{\left[\lambda_c^2 K_{\text{off}}^2\,\eta_\infty^4 - 4\vartheta^2\,(1+\eta_\infty\lambda_c)^4\right]\cosh(\tau\vartheta)}{4K_{\text{off}}\,\rho_\infty\vartheta\,(1+\eta_\infty\lambda_c)^2}. \tag{5.77}$$

Analogous to the steady-state results of the first and second moment shown in (5.69), we find from equation (5.62) that the linearised dynamics of these central moments is given by

$$\phi(\tau) = \rho(\tau)\,\eta(\tau), \quad \text{and} \quad \sigma(\tau) = 2\,\rho(\tau)\,\eta^2(\tau), \tag{5.78}$$

where both the quadratic and cross terms in $\delta\rho_0$ and $\delta\eta_0$ are neglected as they correspond to higher-order terms in the perturbative expansion. This implies that the asymptotic behavior of $\rho(\tau)$, $\phi(\tau)$, and $\sigma(\tau)$ as time τ tends to infinity, shows an exponential decay with a rate given by the real part of $\varphi - \vartheta$.

5.4 Summary

In this chapter, we theoretically study an out-of-equilibrium model for the in-plane membrane dynamics of raft-like structures, where their stability and characteristic sizes are mediated by the exchange of components with an external reservoir. Thus, the formation of intermediate-scale domains in this model is a consequence of the non-equilibrium nature of biomembranes which are subjected to a continuous recycling through the transport of vesicles within the living cell. Using a mean-field approximation, the dynamics of the distribution of domain sizes is examined in a simple aggregation model which can accommodate both scale-free and size-dependent recycling schemes. Closed form solutions to the steady state distributions and its associated central moments are obtained for both types of schemes. Since these

moments are (in principle) measurable quantities, the free parameters in our model can be determined through comparison with experimental data. Moreover, for the size-independent case, the time evolution of the moments is analytically calculated, which provide us with exact results to their corresponding relaxation times. However, the theoretical study of the dynamics in the size-dependent case is found to be a very challenging task even in the linearised approximation. As a result, the Padé approximant solutions to the central moments of the domain size distribution are investigated as well, which allows us to obtain their steady-states and linearised dynamics. Moreover, this also allows the determination of the unknown biophysical parameters controlling recycling by comparing experimental measurements of the moments and their relaxation times with our theoretical predictions. The recycling mechanism studied in this chapter is of biological significance, representing a possible candidate which may contribute to the regulation of lateral membrane heterogeneity and perhaps the stability of lipid rafts observed in cells.

Chapter 6

Conclusions

Every living cell is bounded by a sac-like membrane that plays a central role in almost every cellular process. The fundamental architecture of all cell membranes consist of self-assemblies of lipid molecules which are driven by thermodynamics to the formation of a very thin and stable barrier. In its most basic form, a membrane is represented by a bilayer structure, which acts as a platform for a myriad of other biological entities. A multitude of proteins can be incorporated within the bilayer, with approximately one third of all proteins being membrane resident, and these representing the targets of most of the currently approved drugs. Consequently, biomembranes are of central interest to the physical, life, and medical sciences, which is also reflected by the large research community of scientists interested in their properties and applications.

Beside their biological significance, lipid membranes represent an abundant source of inspiration for physicists and applied mathematicians. In particular, one remarkable aspect which has been widely exploited is the separation of scales (due to the large difference between the membrane thickness and its lateral extent). In Chapter 2, we introduced the key concepts that lead to the formulation of the Canham–Helfinch theory. This is a phenomenological model proposed by Canham, Helfinch, and Evans in the early 1970s, where a fluid membrane is described by a thin elastic sheet and controlled by a handful of course-grained material parameters. The natural language to characterise the surface of the membrane is the framework of differential geometry, so that its effective free-energy can be constructed purely out of geometric invariants, such as the area of the membrane, its mean and Gaussian curvature. This physical description of membranes has been incredibly successful in the understanding of numerous mechanical and dynamical phenomena involving membranes from both theoretical and experimental perspectives. However, there

are still many unanswered questions and problems which have not been entirely elucidated or even considered. A number of problems, which are also of biological relevance, have been explored in this thesis. Namely, the role of membrane shape deformations and composition near transmembrane proteins is investigated in Chapter 3, the methodology of estimating the membrane rigidity from its thermal fluctuations is studied in Chapter 4, and lastly the non-equilibrium effects due to membrane recycling on the lipid phase separation is discussed in Chapter 5. Although the first two studies are concerned with the equilibrium properties of biological membranes, the latter explores aspects of their out-of-equilibrium nature, which is a key signature of biological systems.

In Chapter 3, we study a theoretical model based on the Canham–Helfrich theory, which describes the deformations of a fluid membrane due to the presence of a rigid membrane inclusion. Here, we phenomenologically couple the mean curvature of the membrane to the local compositional asymmetry between the two lipid layers. This allows us compute several properties of biological relevance, in particular, the membrane shape and its composition near a protein of non-trivial structure, and the total deformation energy in the ground state. Moreover, we study the possible effect on mechanosensitive channels that gate by protein tilt or composition variation. We find a crossover of the membrane shape (and its composition) from an overdamped to an underdamped regime driven by the curvature-composition coupling. When the strength of this coupling is strong enough, the system is found in the underdamped regime, which displays spatial undulations in the vicinity of the inclusion. In this scenario, we find that the membrane may suppress the activity of mechanosensitive channels and furthermore it promotes the early formation of protein coats. Importantly, the large shape undulations in the underdamped regime can be used to determine the phenomenological parameters in our model, which shows its predictive power and suggests a novel experimental approach. Other interesting aspects which can be investigated in the future concern the possibility of membrane-mediated interactions due to presence of two (or more) membrane rigid inclusions. Is the interaction attractive or repulsive, and how does it depend on the local compositional variations? Furthermore, another intriguing question is whether the present model can be generalised to many compositional fields in order to study the physics of multi-component membrane systems.

In Chapter 4, we re-examine the theoretical approach used to determine the bending rigidity of membranes, through the statistics of the thermal shape fluctuations of vesicles (particularly, the membrane undulations of GUVs), which is commonly referred to as flicker spectroscopy. We discuss the current methodology

that consists primarily of an analysis of the equatorial fluctuations of vesicles, neglecting as a result the shape undulations out of this plane. We then develop an improved model to account for the projection of thermal fluctuations onto the focal plane from within a finite focal depth associated to any microscope. We impose a Gaussian filter to describe the intensity of light arriving from membrane elements above or below the focal plane, idealising the optical considerations of the imaging system. However, this then allows us to estimate the elastic properties of membranes by comparing the statistics of the first radial moment of the projected intensity with the experimental data. A comparison of our model with the existing approach finds a systematic and significant decrease in the value of the bending rigidity, resolving a previously recognised discrepancy: the bending modulus obtained through shape measurements is significantly larger compare to the values found by other methods (e.g. X-ray scattering and micromechanical manipulation techniques). As a result, our improved analysis may play a pivotal role in the estimation of the membrane elastic constants by means of flicker spectroscopy experiments. Our approach also suggests the possibility of a new method that allows us to estimate the mechanical properties of membranes from the long time-average of the intensity of a fluorescent vesicle, which will be explored in the future. Here, the intensity profile can be theoretically computed, and its width can be found in terms of the membrane elastic constants. By measuring this width as a function of the membrane surface tension, we can determine the bending modulus. This can be achieved experimentally by controlling the surface tension through a micropipette aspiration technique.

In Chapter 5, we study the role of membrane recycling and how it controls the size and life-time of raft-like structures on the membrane. The size of these membrane domains is controlled by the permanent exchange rates of membrane constituents with an external reservoir, which occurs due to numerous processes involving the transport of endosomes within the interior of cells. Within a mean-field model of the domain kinetics, we show how a continuous recycling can provide a mechanism for the formation of raft-like entities in a non-equilibrium fluid membrane composed of two characteristic lipid species. Here, closed form solutions to the steady state distribution of the domain size and its associated central moments are determined for a certain recycling scheme. The latter includes both scale-free and size-dependent recycling processes. Since the total-number-per-area and the area fraction of domains (namely, the lowest moments of the distribution) are experimentally measurable quantities, the phenomenological parameters in our model can be obtained by comparing against experimental data. In addition, the time evolution of the lowest moments has been studied and exact analytic results are

derived for specific cases. Measurements of their relaxation times can constitute another way of experimentally testing and analysing this non-equilibrium model. The theoretical results may have important biological and physical consequences to the modulation of lateral heterogeneity in biomembranes and perhaps it may shed light on the understanding of nano-membrane domains (or lipid rafts) which are indirectly observed in cells.

In conclusion, we have developed a number of theoretical models to study both the equilibrium and non-equilibrium properties of biomembranes, which may be further applied to a wide range of other applications. However, there are various other unanswered questions that require a full theoretical and experimental analysis, and a great deal of research still has to be done in this exciting field.

Bibliography

[1] Alberts, B. *et al. Molecular Biology of the Cell* (Garland Science, New York, 2008), 5th edn.

[2] Lipowsky, R. & Sackmann, E. *Structure and Dynamics of Membranes: I. From Cells to Vesicles* (Elsevier Science, Amsterdam, 1995).

[3] Neher, E. & Sakmann, B. Single-channel currents recorded from membrane of denervated frog muscle fibres. *Nature* **260**, 799–802 (1976).

[4] Perozo, E. Gating prokaryotic mechanosensitive channels. *Nat. Rev. Mol. Cell Bio.* **7**, 109–119 (2006).

[5] Vásquez, V. & Perozo, E. Structural biology: A channel with a twist. *Nature* **461**, 47–49 (2009).

[6] Haswell, E. S., Phillips, R. & Rees, D. C. Mechanosensitive channels: What can they do and how do they do it? *Structure* **19**, 1356–1369 (2011).

[7] Gennis, R. B. *Biomembranes: Molecular Structure and Function* (Springer-Verlag, New York, 1989).

[8] Stadler, A. & Linderkamp, O. Flow behavior of neonatal and adult erythrocytes in narrow capillaries. *Microvasc. Res.* **37**, 267–279 (1989).

[9] Heimburg, T. *Thermal Biophysics of Membranes* (Wiley-VCH, Berlin, 2007).

[10] Yildirim, M. A., Goh, K.-I., Cusick, M. E., Barabási, A.-L. & Vidal, M. Drug-target network. *Nat. Biotechnol.* **25**, 1119–26 (2007).

[11] Torchilin, V. P. Multifunctional nanocarriers. *Adv. Drug Deliv. Rev.* **58**, 1532–55 (2006).

[12] Karlsson, A. *et al.* Networks of nanotubes and containers. *Nature* **409**, 150–2 (2001).

[13] Crespilho, F. N. *Nanobioelectrochemistry: From Implantable Biosensors to Green Power Generation* (Springer-Verlag, New York, 2012).

[14] Nelson, D., Piran, T. & Weinberg, S. *Statistical Mechanics of Membranes and Surfaces* (World Scientific Publishing Company, 2004), 2nd edn.

[15] Seifert, U. Configurations of fluid membranes and vesicles. *Adv. Phys.* **46**, 13–137 (1997).

[16] Deserno, M. Fluid lipid membranes: From differential geometry to curvature stresses. *Chem. Phys. Lipids* **185**, 11–45 (2015).

[17] Edidin, M. Lipids on the frontier: a century of cell-membrane bilayers. *Nat. Rev. Mol. Cell Bio.* **4**, 414–418 (2003).

[18] Overton, E. Über die osmotischen Eigenschaften der lebenden Pflanzenund Tierzelle. *Vierteljahresschr. Naturforsch. Ges. Zürich* **40**, 159–201 (1895).

[19] Langmuir, I. The constitution and fundamental properties of solids and liquids. II. Liquids. *J. Am. Chem. Soc.* **39**, 1848–1906 (1917).

[20] Gorter, E. & Grendel, F. On bimolecular layers of lipoids on the chromocytes of the blood. *J. Exp. Med.* **41**, 439–443 (1925).

[21] Danielli, J. F. & Davson, H. A contribution to the theory of permeability of thin films. *J. Cell. Comp. Physiol.* **5**, 495–508 (1935).

[22] Robertson, J. D. The ultrastructure of cell membranes and their derivatives. *Biochem. Soc. Symp.* **16**, 3–43 (1959).

[23] Branton, D. Fracture faces of frozen membranes. *Proc. Natl. Acad. Sci. USA* **55**, 1048–56 (1966).

[24] Chapman, D. Phase transitions and fluidity characteristics of lipids and cell membranes. *Quart. Rev. Biophys.* **8**, 185–235 (1975).

[25] Bretscher, M. S. Membrane structure: some general principles. *Science* **181**, 622–629 (1973).

[26] Singer, S. J. & Nicolson, G. L. The fluid mosaic model of the structure of cell membranes. *Science* **175**, 720–731 (1972).

[27] Engelman, D. M. Membranes are more mosaic than fluid. *Nature* **438**, 578–580 (2005).

[28] Simons, K. & Ikonen, E. Functional rafts in cell membranes. *Nature* **387**, 569–572 (1997).

[29] Simons, K. & Ikonen, E. How cells handle cholesterol. *Science* **290**, 1721–1726 (2000).

[30] Mouritsen, O. G. & Bloom, M. Mattress model of lipid-protein interactions in membranes. *Biophys. J.* **46**, 141–153 (1984).

[31] Huang, H. W. Deformation free energy of bilayer membrane and its effect on gramicidin channel lifetime. *Biophys. J.* **50**, 1061–1070 (1986).

[32] Aranda-Espinoza, H., Berman, A., Dan, N., Pincus, P. & Safran, S. A. Interaction between inclusions embedded in membranes. *Biophys. J.* **71**, 648–656 (1996).

[33] Sens, P. & Safran, S. A. Inclusions induced phase separation in mixed lipid film. *Eur. Phys. J. E* **1**, 237–248 (2000).

[34] Haselwandter, C. A. & Phillips, R. Directional interactions and cooperativity between mechanosensitive membrane proteins. *Eur. Lett.* **101**, 68002 (2013).

[35] Haselwandter, C. A. & Phillips, R. Connection between Oligomeric State and Gating Characteristics of Mechanosensitive Ion Channels. *PLoS Comput. Biol.* **9**, e1003055 (2013).

[36] McMahon, H. T. & Gallop, J. L. Membrane curvature and mechanisms of dynamic cell membrane remodelling. *Nature* **438**, 590–596 (2005).

[37] Callan-Jones, A., Sorre, B. & Bassereau, P. Curvature-driven lipid sorting in biomembranes. *Cold Spring Harb. Perspect. Biol.* **3**, a004648 (2011).

[38] Mouritsen, O. G. Lipids, curvature, and nano-medicine. *Eur. J. Lipid Sci. Tech.* **113**, 1174–1187 (2011).

[39] Mouritsen, O. G. *Life – As a Matter of Fat: The Emerging Science of Lipidomics* (Springer-Verlag, Berlin, 2005).

[40] Lasic, D. D. The mechanism of vesicle formation. *Biochem. J.* **256**, 1–11 (1988).

[41] Kozlov, M. M., Leikin, S. & Rand, R. P. Bending, hydration and interstitial energies quantitatively account for the hexagonal-lamellar-hexagonal reentrant phase transition in dioleoylphosphatidylethanolamine. *Biophys. J.* **67**, 1603–1611 (1994).

[42] Israelachvili, J. N., Mitchell, D. J. & Ninham, B. W. Theory of self-assembly of hydrocarbon amphiphiles into micelles and bilayers. *J. Chem. Soc. Faraday Trans.* **72**, 1525 (1976).

[43] Zasadzinski, J. & Schneider, M. Ripple wavelength, amplitude, and configuration in lyotropic liquid crystals as a function of effective headgroup size. *J. Phys. Fr.* **48**, 2001–11 (1987).

[44] Ipsen, J. H., Karlström, G., Mouritsen, O. G., Wennerström, H. & Zuckermann, M. J. Phase equilibria in the phosphatidylcholine-cholesterol system. *Biochim. Biophys. Acta* **905**, 162–72 (1987).

[45] Komura, S. & Andelman, D. Physical aspects of heterogeneities in multi-component lipid membranes. *Adv. Colloid Interface Sci.* **208**, 34–46 (2014).

[46] Spivak, M. *A Comprehensive Introduction to Differential Geometry* (Publish or Perish, Berkeley, 1999), 3rd edn.

[47] Kamien, R. The geometry of soft materials: a primer. *Rev. Mod. Phys.* **74**, 953–971 (2002).

[48] Kreyszig, E. *Differential Geometry* (Dover Publications Inc., Toronto, 1991).

[49] Riley, K., Hobson, M. & Bence, S. *Mathematical Methods for Physics and Engineering* (Dover Publications Inc., New York, 1992).

[50] Canham, P. B. The minimum energy of bending as a possible explanation of the biconcave shape of the human red blood cell. *J. Theor. Biol.* **26**, 61–81 (1970).

[51] Helfrich, W. Elastic properties of lipid bilayers: theory and possible experiments. *Z. Naturforsch. C Bio. Sci.* **28**, 693–703 (1973).

[52] Evans, E. A. Bending resistance and chemically induced moments in membrane bilayers. *Biophys. J.* **14**, 923–931 (1974).

[53] Capovilla, R., Guven, J. & Santiago, J. A. Deformations of the geometry of lipid vesicles. *J. Phys. A Math. Gen. 3* **36**, 6281–6295 (2003).

[54] Svetina, S. & Žekš, B. Membrane bending energy and shape determination of phospholipid vesicles and red blood cells. *Eur. Biophys. J.* **17**, 101–111 (1989).

[55] Heinrich, V., Svetina, S. & Žekš, B. Nonaxisymmetric vesicle shapes in a generalized bilayer-couple model and the transition between oblate and prolate axisymmetric shapes. *Phys. Rev. E* **48**, 3112–3123 (1993).

[56] Kralj-Iglič, V., Svetina, S. & Žekš, B. The existence of non-axisymmetric bilayer vesicle shapes predicted by the bilayer couple model. *Eur. Biophys. J.* **22**, 97–103 (1993).

[57] Miao, L., Seifert, U., Wortis, M. & Döbereiner, H.-G. Budding transitions of fluid-bilayer vesicles: The effect of area-difference elasticity. *Phys. Rev. E* **49**, 5389–5407 (1994).

[58] Nelson, P. & Powers, T. Renormalization of chiral couplings in titled bilayer membranes. *J. Phys. II Fr.* **3**, 1535–1569 (1993).

[59] Powers, T. & Nelson, P. Fluctuating Membranes with Tilt Order. *J. Phys. II Fr.* **5**, 1671–1678 (1995).

[60] Seifert, U., Shillcock, J. & Nelson, P. Role of Bilayer Tilt Difference in Equilibrium Membrane Shapes. *Phys. Rev. Lett.* **77**, 5237–5240 (1996).

[61] Tu, Z. & Seifert, U. Concise theory of chiral lipid membranes. *Phys. Rev. E* **76**, 031603 (2007).

[62] Baumgart, T., Das, S., Webb, W. W. & Jenkins, J. T. Membrane elasticity in giant vesicles with fluid phase coexistence. *Biophys. J.* **89**, 1067–80 (2005).

[63] Siegel, D. P. Determining the ratio of the Gaussian curvature and bending elastic moduli of phospholipids from Q(II) phase unit cell dimensions. *Biophys. J.* **91**, 608–18 (2006).

[64] Siegel, D. P. The Gaussian curvature elastic energy of intermediates in membrane fusion. *Biophys. J.* **95**, 5200–15 (2008).

[65] Semrau, S., Idema, T., Holtzer, L., Schmidt, T. & Storm, C. Accurate Determination of Elastic Parameters for Multicomponent Membranes. *Phys. Rev. Lett.* **100**, 088101 (2008).

[66] Morris, C. & Homann, U. Cell Surface Area Regulation and Membrane Tension. *J. Membr. Biol.* **179**, 79–102 (2001).

[67] Nagle, J. F. Introductory Lecture: Basic quantities in model biomembranes. *Farad. Discuss.* **161**, 11–29 (2013).

[68] Lipowsky, R. Spontaneous tubulation of membranes and vesicles reveals membrane tension generated by spontaneous curvature. *Farad. Discuss.* **161**, 305–331 (2013).

[69] Lipowsky, R. Coupling of bending and stretching deformations in vesicle membranes. *Adv. Colloid Interface Sci.* **208**, 14–24 (2014).

[70] Bassereau, P., Sorre, B. & Lévy, A. Bending lipid membranes: Experiments after W. Helfrich's model. *Adv. Colloid Interface Sci.* **208**, 47–57 (2014).

[71] Rawicz, W., Olbrich, K. C., McIntosh, T., Needham, D. & Evans, E. Effect of chain length and unsaturation on elasticity of lipid bilayers. *Biophys. J.* **79**, 328–339 (2000).

[72] Marsh, D. Elastic curvature constants of lipid monolayers and bilayers. *Chem. Phys. Lipids* **144**, 146–159 (2006).

[73] Chan, Y.-H. M. & Boxer, S. G. Model membrane systems and their applications. *Curr. Opin. Chem. Biol.* **11**, 581–7 (2007).

[74] Kahya, N. Protein-protein and protein-lipid interactions in domain-assembly: lessons from giant unilamellar vesicles. *Biochim. Biophys. Acta* **1798**, 1392–8 (2010).

[75] Sens, P., Johannes, L. & Bassereau, P. Biophysical approaches to protein-induced membrane deformations in trafficking. *Curr. Opin. Chem. Biol.* **20**, 476–82 (2008).

[76] Walde, P., Cosentino, K., Engel, H. & Stano, P. Giant vesicles: preparations and applications. *ChemBioChem* **11**, 848–65 (2010).

[77] Watts, T. H., Brian, A. A., Kappler, J. W., Marrack, P. & McConnell, H. M. Antigen presentation by supported planar membranes containing affinity-purified I-Ad. *Proc. Natl. Acad. Sci. USA* **81**, 7564–8 (1984).

[78] Watts, T. H., Gaub, H. E. & McConnell, H. M. T-cell-mediated association of peptide antigen and major histocompatibility complex protein detected by energy transfer in an evanescent wave-field. *Nature* **320**, 179–81 (1986).

[79] Castellana, E. T. & Cremer, P. S. Solid supported lipid bilayers: From biophysical studies to sensor design. *Surf. Sci. Rep.* **61**, 429–444 (2006).

[80] Wagner, M. L. & Tamm, L. K. Tethered polymer-supported planar lipid bilayers for reconstitution of integral membrane proteins: silane-polyethyleneglycol-lipid as a cushion and covalent linker. *Biophys. J.* **79**, 1400–14 (2000).

[81] Tanaka, M. & Sackmann, E. Polymer-supported membranes as models of the cell surface. *Nature* **437**, 656–63 (2005).

[82] Achalkumar, A. S., Bushby, R. J. & Evans, S. D. Cholesterol-based anchors and tethers for phospholipid bilayers and for model biological membranes. *Soft Matter* **6**, 6036 (2010).

[83] Lyatskaya, Y., Liu, Y., Tristram-Nagle, S., Katsaras, J. & Nagle, J. Method for obtaining structure and interactions from oriented lipid bilayers. *Phys. Rev. E* **63**, 011907 (2000).

[84] Mennicke, U. & Salditt, T. Preparation of Solid-Supported Lipid Bilayers by Spin-Coating. *Langmuir* **18**, 8172–8177 (2002).

[85] Kucerka, N. *et al.* Structure of fully hydrated fluid phase DMPC and DLPC lipid bilayers using X-ray scattering from oriented multilamellar arrays and from unilamellar vesicles. *Biophys. J.* **88**, 2626–37 (2005).

[86] Salditt, T. Thermal fluctuations and stability of solid-supported lipid membranes. *J. Phys. Condens. Matter* **17**, R287–R314 (2005).

[87] Pabst, G., Kucerka, N., Nieh, M.-P., Rheinstädter, M. C. & Katsaras, J. Applications of neutron and X-ray scattering to the study of biologically relevant model membranes. *Chem. Phys. Lipids* **163**, 460–79 (2010).

[88] Daillant, J. *et al.* Structure and fluctuations of a single floating lipid bilayer. *Proc. Natl. Acad. Sci. USA* **102**, 11639–44 (2005).

[89] Fragneto, G., Charitat, T., Bellet-Amalric, E., Cubitt, R. & Grane, F. Swelling of Phospholipid Floating Bilayers: The Effect of Chain Length. *Langmuir* **19**, 7695–7702 (2003).

[90] Hemmerle, A. *et al.* Controlling interactions in supported bilayers from weak electrostatic repulsion to high osmotic pressure. *Proc. Natl. Acad. Sci. USA* **109**, 19938–42 (2012).

[91] Brochard, F. & Lennon, J. Frequency spectrum of the flicker phenomenon in erythrocytes. *J. Phys. Fr.* **36**, 1035–1047 (1975).

[92] Helfrich, W. & Servuss, R. M. Undulations, steric interaction and cohesion of fluid membranes. *Nuovo Cim. D* **3**, 137–151 (1984).

[93] Peterson, M. A., Strey, H. & Sackmann, E. Theoretical and phase contrast microscopic eigenmode analysis of erythrocyte flicker : amplitudes. *J. Phys. II Fr.* **2**, 1273–1285 (1992).

[94] Strey, H., Peterson, M. & Sackmann, E. Measurement of erythrocyte membrane elasticity by flicker eigenmode decomposition. *Biophys. J.* **69**, 478–88 (1995).

[95] Schneider, M., Jenkins, J. & Webb, W. Thermal fluctuations of large quasi-spherical bimolecular phospholipid vesicles. *J. Phys. Fr.* **45**, 1457–1472 (1984).

[96] Bivas, I., Hanusse, P., Bothorel, P., Lalanne, J. & Aguerre-Chariol, O. An application of the optical microscopy to the determination of the curvature elastic modulus of biological and model membranes. *J. Phys. Fr.* **48**, 855–867 (1987).

[97] Faucon, J., Mitov, M. D., Méléard, P., Bivas, I. & Bothorel, P. Bending elasticity and thermal fluctuations of lipid membranes. Theoretical and experimental requirements. *J. Phys. Fr.* **50**, 2389–2414 (1989).

[98] Mutz, M. & Helfrich, W. Bending rigidities of some biological model membranes as obtained from the Fourier analysis of contour sections. *J. Phys. Fr.* **51**, 991–1001 (1990).

[99] Méléard, P., Faucon, J. F., Mitov, M. D. & Bothorel, P. Pulsed-Light Microscopy Applied to the Measurement of the Bending Elasticity of Giant Liposomes. *Eur. Lett.* **19**, 267–271 (1992).

[100] Häckl, W., Bärmann, M. & Sackmann, E. Shape Changes of Self-Assembled Actin Bilayer Composite Membranes. *Phys. Rev. Lett.* **80**, 1786–1789 (1998).

[101] Méléard, P. *et al.* Mechanical properties of model membranes studied from shape transformations of giant vesicles. *Biochimie* **80**, 401–413 (1998).

[102] Döbereiner, H.-G. *et al.* Advanced Flicker Spectroscopy of Fluid Membranes. *Phys. Rev. Lett.* **91**, 048301 (2003).

[103] Pécréaux, J., Döbereiner, H. G., Prost, J., Joanny, J. F. & Bassereau, P. Refined contour analysis of giant unilamellar vesicles. *Eur. Phys. J. E* **13**, 277–290 (2004).

[104] Méléard, P., Pott, T., Bouvrais, H. & Ipsen, J. H. Advantages of statistical analysis of giant vesicle flickering for bending elasticity measurements. *Eur. Phys. J. E* **34**, 116 (2011).

[105] Helfer, E. *et al.* Microrheology of Biopolymer-Membrane Complexes. *Phys. Rev. Lett.* **85**, 457–460 (2000).

[106] Brown, A. T., Kotar, J. & Cicuta, P. Active rheology of phospholipid vesicles. *Phys. Rev. E* **84**, 021930 (2011).

[107] Betz, T. & Sykes, C. Time resolved membrane fluctuation spectroscopy. *Soft Matter* **8**, 5317 (2012).

[108] Milner, S. T. & Safran, S. A. Dynamical fluctuations of droplet microemulsions and vesicles. *Phys. Rev. A* **36**, 4371–4379 (1987).

[109] Waugh, R. & Evans, E. A. Thermoelasticity of red blood cell membrane. *Biophys. J.* **26**, 115–31 (1979).

[110] Kwok, R. & Evans, E. Thermoelasticity of large lecithin bilayer vesicles. *Biophys. J.* **35**, 637–52 (1981).

[111] Evans, E. & Rawicz, W. Entropy-driven tension and bending elasticity in condensed-fluid membranes. *Phys. Rev. Lett.* **64**, 2094–2097 (1990).

[112] Zhelev, D. V., Needham, D. & Hochmuth, R. M. A novel micropipet method for measuring the bending modulus of vesicle membranes. *Biophys. J.* **67**, 720–7 (1994).

[113] Fournier, J.-B., Ajdari, A. & Peliti, L. Effective-Area Elasticity and Tension of Micromanipulated Membranes. *Phys. Rev. Lett.* **86**, 4970–4973 (2001).

[114] Henriksen, J. R. & Ipsen, J. H. Measurement of membrane elasticity by micro-pipette aspiration. *Eur. Phys. J. E* **14**, 149–67 (2004).

[115] Borghi, N., Rossier, O. & Brochard-Wyart, F. Hydrodynamic extrusion of tubes from giant vesicles. *Eur. Lett.* **64**, 837–843 (2003).

[116] Cans, A.-S. *et al.* Artificial cells: unique insights into exocytosis using liposomes and lipid nanotubes. *Proc. Natl. Acad. Sci. USA* **100**, 400–4 (2003).

[117] Hochmuth, R. M. & Evans, E. A. Extensional flow of erythrocyte membrane from cell body to elastic tether. I. Analysis. *Biophys. J.* **39**, 71–81 (1982).

[118] Hochmuth, R. M., Wiles, H. C., Evans, E. A. & McCown, J. T. Extensional flow of erythrocyte membrane from cell body to elastic tether. II. Experiment. *Biophys. J.* **39**, 83–9 (1982).

[119] Heinrich, V. & Waugh, R. E. A piconewton force transducer and its application to measurement of the bending stiffness of phospholipid membranes. *Ann. Biomed. Eng.* **24**, 595–605 (1996).

[120] Koster, G., Cacciuto, A., Derényi, I., Frenkel, D. & Dogterom, M. Force Barriers for Membrane Tube Formation. *Phys. Rev. Lett.* **94**, 068101 (2005).

[121] Cuvelier, D., Derényi, I., Bassereau, P. & Nassoy, P. Coalescence of membrane tethers: experiments, theory, and applications. *Biophys. J.* **88**, 2714–26 (2005).

[122] Derényi, I., Jülicher, F. & Prost, J. Formation and Interaction of Membrane Tubes. *Phys. Rev. Lett.* **88**, 238101 (2002).

[123] Powers, T. R., Huber, G. & Goldstein, R. E. Fluid-membrane tethers: Minimal surfaces and elastic boundary layers. *Phys. Rev. E* **65**, 041901 (2002).

[124] Kummrow, M. & Helfrich, W. Deformation of giant lipid vesicles by electric fields. *Phys. Rev. A* **44**, 8356–8360 (1991).

[125] Winterhalter, M. & Helfrich, W. Deformation of spherical vesicles by electric fields. *J. Colloid Interface Sci.* **122**, 583–586 (1988).

[126] Dimova, R. *et al.* Giant vesicles in electric fields. *Soft Matter* **3**, 817 (2007).

[127] Aranda, S., Riske, K. A., Lipowsky, R. & Dimova, R. Morphological transitions of vesicles induced by alternating electric fields. *Biophys. J.* **95**, L19–21 (2008).

[128] Dimova, R. *et al.* Vesicles in electric fields: Some novel aspects of membrane behavior. *Soft Matter* **5**, 3201 (2009).

[129] Bacri, J.-C., Cabuil, V., Cebers, A., Menager, C. & Perzynski, R. Flattening of ferro-vesicle undulations under a magnetic field. *Eur. Lett.* **33**, 235–240 (1996).

[130] Suchyna, T. M. *et al.* Bilayer-dependent inhibition of mechanosensitive channels by neuroactive peptide enantiomers. *Nature* **430**, 235–240 (2004).

[131] Moe, P. & Blount, P. Assessment of potential stimuli for mechano-dependent gating of MscL: effects of pressure, tension, and lipid headgroups. *Biochemistry* **44**, 12239–12244 (2005).

[132] Krepkiy, D. *et al.* Structure and hydration of membranes embedded with voltage-sensing domains. *Nature* **462**, 473–479 (2009).

[133] Milescu, M. *et al.* Interactions between lipids and voltage sensor paddles detected with tarantula toxins. *Nat. Struct. Biol.* **16**, 1080–1085 (2009).

[134] Lee, A. G. How lipids affect the activities of integral membrane proteins. *Biochim. Biophys. Acta* **1666**, 62–87 (2004).

[135] Mitra, K., Ubarretxena-Belandia, I., Taguchi, T., Warren, G. & Engelman, D. M. Modulation of the bilayer thickness of exocytic pathway membranes by membrane proteins rather than cholesterol. *Proc. Natl. Acad. Sci. USA* **101**, 4083–4088 (2004).

[136] Dowhan, W., Mileykovskaya, E. & Bogdanov, M. Diversity and versatility of lipid-protein interactions revealed by molecular genetic approaches. *Biochim. Biophys. Acta* **1666**, 19–39 (2004).

[137] Nyholm, T. K. M., Ozdirekcan, S. & Killian, J. A. How protein transmembrane segments sense the lipid environment. *Biochemistry* **46**, 1457–1465 (2007).

[138] Andersen, O. S. & Koeppe, R. E. Bilayer thickness and membrane protein function: an energetic perspective. *Annu. Rev. Biophys. Biomol. Struct.* **36**, 107–130 (2007).

[139] Phillips, R., Ursell, T., Wiggins, P. & Sens, P. Emerging roles for lipids in shaping membrane-protein function. *Nature* **459**, 379–385 (2009).

[140] Lundbaek, J. a., Collingwood, S. a., Ingólfsson, H. I., Kapoor, R. & Andersen, O. S. Lipid bilayer regulation of membrane protein function: gramicidin channels as molecular force probes. *J. R. Soc. Interface* **7**, 373–395 (2010).

[141] Kahya, N., Scherfeld, D., Bacia, K., Poolman, B. & Schwille, P. Probing lipid mobility of raft-exhibiting model membranes by fluorescence correlation spectroscopy. *J. Biol. Chem.* **278**, 28109–28115 (2003).

[142] Doeven, M. K. *et al.* Distribution, lateral mobility and function of membrane proteins incorporated into giant unilamellar vesicles. *Biophys. J.* **88**, 1134–1142 (2005).

[143] Guigas, G. & Weiss, M. Size-dependent diffusion of membrane inclusions. *Biophys. J.* **91**, 2393–2398 (2006).

[144] Dan, N., Pincus, P. & Safran, S. A. Membrane-induced interactions between inclusions. *Langmuir* **9**, 2768–2771 (1993).

[145] Nielsen, C., Goulian, M. & Andersen, O. S. Energetics of inclusion-induced bilayer deformations. *Biophys. J.* **74**, 1966–1983 (1998).

[146] Fournier, J.-B. Microscopic membrane elasticity and interactions among membrane inclusions: interplay between the shape, dilation, tilt and tilt-difference modes. *Eur. Phys. J. B* **11**, 261–272 (1999).

[147] Wiggins, P. & Phillips, R. Membrane-protein interactions in mechanosensitive channels. *Biophys. J.* **88**, 880–902 (2005).

[148] Ursell, T., Phillips, R., Kondev, J., Reeves, D. & Wiggins, P. The Role of Lipid Bilayer Mechanics in Mechanosensation. In Kamkin, A. & Kiseleva, I. (eds.) *Mechanosensitivity Cells Tissues 1 Mechanosensitive Ion Channels*, 37–70 (Springer, 2008).

[149] Weikl, T., Kozlov, M. & Helfrich, W. Interaction of conical membrane inclusions: Effect of lateral tension. *Phys. Rev. E* **57**, 6988–6995 (1998).

[150] Chou, T., Kim, K. S. & Oster, G. Statistical thermodynamics of membrane bending-mediated protein-protein attractions. *Biophys. J.* **80**, 1075–1087 (2001).

[151] Kim, K. S., Neu, J. & Oster, G. Effect of protein shape on multibody interactions between membrane inclusions. *Phys. Rev. E* **61**, 4281–4285 (2000).

[152] Kim, K. S., Neu, J. & Oster, G. Curvature-mediated interactions between membrane proteins. *Biophys. J.* **75**, 2274–2291 (1998).

[153] Goulian, M., Bruinsma, R. & Pincus, P. Long-Range Forces in Heterogeneous Fluid Membranes. *Eur. Lett.* **22**, 145–150 (1993).

[154] Park, J. & Lubensky, T. C. Interactions between membrane inclusions on fluctuating membranes. *J. Phys. I Fr.* **6**, 1217–1235 (1996).

[155] Turner, M. S. & Sens, P. Inclusions on fluid membranes anchored to elastic media. *Biophys. J.* **76**, 564–572 (1999).

[156] Markin, V. S. & Sachs, F. Thermodynamics of mechanosensitivity. *Phys. Biol.* **1**, 110–124 (2004).

[157] Ursell, T., Huang, K. C., Peterson, E. & Phillips, R. Cooperative gating and spatial organization of membrane proteins through elastic interactions. *PLoS Comput. Biol.* **3**, e81 (2007).

[158] Kumar, V. V., Malewicz, B. & Baumann, W. J. Lysophosphatidylcholine stabilizes small unilamellar phosphatidylcholine vesicles. Phosphorus-31 NMR evidence for the "wedge" effect. *Biophys. J.* **55**, 789–792 (1989).

[159] Turner, M. S. & Sens, P. Gating-by-Tilt of Mechanically Sensitive Membrane Channels. *Phys. Rev. Lett.* **93**, 118103 (2004).

[160] Heuser, J. Three-dimensional visualization of coated vesicle formation in fibroblasts. *J. Cell Biol.* **84**, 560–583 (1980).

[161] Fournier, J. B. & Dommersnes, P. G. Comment on "Long-range forces in heterogeneous fluid membranes. *Eur. Lett.* **39**, 681–682 (2007).

[162] Rautu, S. A., Rowlands, G. & Turner, M. S. Membrane Composition Variation and Underdamped Mechanics near Transmembrane Proteins and Coats. *Phys. Rev. Lett.* **114**, 098101 (2015).

[163] Leibler, S. Curvature instability in membranes. *J. Phys. Fr.* **47**, 507–516 (1986).

[164] Leibler, S. & Andelman, D. Ordered and curved meso-structures in membranes and amphiphilic films. *J. Phys. Fr.* **48**, 2013–2018 (1987).

[165] Sunil Kumar, P. B., Gompper, G. & Lipowsky, R. Modulated phases in multicomponent fluid membranes. *Phys. Rev. E* **60**, 4610–4618 (1999).

[166] Schick, M. Membrane heterogeneity: Manifestation of a curvature-induced microemulsion. *Phys. Rev. E* **85**, 1–4 (2012).

[167] Byron, F. W. & Fuller, R. W. *Mathematics of Classical and Quantum Physics* (Dover Publications Inc., 1992).

[168] Abramowitz & Stegun. *Handbook of Mathematical Functions* (Dover Publications Inc., 2008).

[169] Gradshteyn, I. S. *et al. Table of Integrals, Series, and Products*, vol. 103 (Academic Press, 1981), 6th edn.

[170] Lee, S.-Y., Lee, A., Chen, J. & MacKinnon, R. Structure of the KvAP voltage-dependent K+ channel and its dependence on the lipid membrane. *Proc. Natl. Acad. Sci. USA* **102**, 15441–15446 (2005).

[171] Unwin, N. Refined structure of the nicotinic acetylcholine receptor at 4A resolution. *J. Mol. Biol.* **346**, 967–989 (2005).

[172] Yamashita, A., Singh, S. K., Kawate, T., Jin, Y. & Gouaux, E. Crystal structure of a bacterial homologue of Na+/Cl- -dependent neurotransmitter transporters. *Nature* **437**, 215–223 (2005).

[173] Singh, S. K., Piscitelli, C. L., Yamashita, A. & Gouaux, E. A competitive inhibitor traps LeuT in an open-to-out conformation. *Science* **322**, 1655–1661 (2008).

[174] Booth, I. R., Edwards, M. D., Black, S., Schumann, U. & Miller, S. Mechanosensitive channels in bacteria: signs of closure? *Nat. Rev. Microbiol.* **5**, 431–440 (2007).

[175] Sukharev, S. I., Blount, P., Martinac, B., Blattner, F. R. & Kung, C. A large-conductance mechanosensitive channel in E. coli encoded by mscL alone. *Nature* **368**, 265–268 (1994).

[176] Kung, C., Martinac, B. & Sukharev, S. Mechanosensitive channels in microbes. *Annu. Rev. Microbiol.* **64**, 313–329 (2010).

[177] Chiang, C.-S., Anishkin, A. & Sukharev, S. Gating of the large mechanosensitive channel in situ: estimation of the spatial scale of the transition from channel population responses. *Biophys. J.* **86**, 2846–2861 (2004).

[178] Sukharev, S. Purification of the small mechanosensitive channel of Escherichia coli (MscS): the subunit structure, conduction, and gating characteristics in liposomes. *Biophys. J.* **83**, 290–298 (2002).

[179] Perozo, E., Kloda, A., Cortes, D. M. & Martinac, B. Physical principles underlying the transduction of bilayer deformation forces during mechanosensitive channel gating. *Nat. Struct. Biol.* **9**, 696–703 (2002).

[180] Kardar, M. *Statistical Physics of Fields* (Cambridge University Press, Cambridge, 2007).

[181] Henriksen, J. R. & Ipsen, J. H. Thermal undulations of quasi-spherical vesicles stabilized by gravity. *Eur. Phys. J. E. Soft Matter* **9**, 365–74 (2002).

[182] Mertz, J. *Introduction to Optical Microscopy* (Roberts and Company Publishers, Greenwood Village, Colorado, 2009).

[183] Bi, H., Yang, B., Wang, L., Cao, W. & Han, X. Electroformation of giant unilamellar vesicles using interdigitated ITO electrodes. *J. Mater. Chem. A* **1**, 7125 (2013).

[184] Sivia, D. S. & Skilling, J. *Data Analysis: A Bayesian Tutorial* (Oxford University Press, Oxford, 2006), second edn.

[185] Kucerka, N., Tristram-Nagle, S. & Nagle, J. F. Structure of fully hydrated fluid phase lipid bilayers with monounsaturated chains. *J. Membr. Biol.* **208**, 193–202 (2006).

[186] Pan, J., Mills, T. T., Tristram-Nagle, S. & Nagle, J. F. Cholesterol Perturbs Lipid Bilayers Nonuniversally. *Phys. Rev. Lett.* **100**, 198103 (2008).

[187] Li, D.-P., Hu, S.-X. & Li, M. Full q -space analysis of x-ray scattering of multilamellar membranes at liquid-solid interfaces. *Phys. Rev. E* **73**, 031916 (2006).

[188] Pan, J., Tristram-Nagle, S., Kucerka, N. & Nagle, J. F. Temperature dependence of structure, bending rigidity, and bilayer interactions of dioleoylphosphatidylcholine bilayers. *Biophys. J.* **94**, 117–24 (2008).

[189] Tian, A., Capraro, B. R., Esposito, C. & Baumgart, T. Bending stiffness depends on curvature of ternary lipid mixture tubular membranes. *Biophys. J.* **97**, 1636–46 (2009).

[190] Sorre, B. *et al.* Curvature-driven lipid sorting needs proximity to a demixing point and is aided by proteins. *Proc. Natl. Acad. Sci. USA* **106**, 5622–6 (2009).

[191] Gracià, R. S., Bezlyepkina, N., Knorr, R. L., Lipowsky, R. & Dimova, R. Effect of cholesterol on the rigidity of saturated and unsaturated membranes: fluctuation and electrodeformation analysis of giant vesicles. *Soft Matter* **6**, 1472 (2010).

[192] Hao, M. Characterization of Rapid Membrane Internalization and Recycling. *J. Biol. Chem.* **275**, 15279–15286 (2000).

[193] Pike, L. J. Rafts defined: a report on the Keystone Symposium on Lipid Rafts and Cell Function. *J. Lipid Res.* **47**, 1597–8 (2006).

[194] Leslie, M. Do Lipid Rafts Exist? *Science* **334**, 1046–1047 (2011).

[195] Munro, S. Lipid Rafts: Elusive or Illusive? *Cell* **115**, 377–388 (2003).

[196] Veatch, S. L. & Keller, S. L. Seeing spots: complex phase behavior in simple membranes. *Biochim. Biophys. Acta* **1746**, 172–185 (2005).

[197] Pike, L. J. The challenge of lipid rafts. *J. Lipid Res.* **50**, S323–8 (2009).

[198] Daumas, F. *et al.* Confined diffusion without fences of a g-protein-coupled receptor as revealed by single particle tracking. *Biophys. J.* **84**, 356–66 (2003).

[199] Destainville, N., Dumas, F. & Salomé, L. What do diffusion measurements tell us about membrane compartmentalisation? Emergence of the role of interprotein interactions. *J. Chem. Biol.* **1**, 37–48 (2008).

[200] Ying, W., Huerta, G., Steinberg, S. & Zúñiga, M. Time series analysis of particle tracking data for molecular motion on the cell membrane. *Bull. Math. Biol.* **71**, 1967–2024 (2009).

[201] Robson, A., Burrage, K. & Leake, M. C. Inferring diffusion in single live cells at the single-molecule level. *Phil. Trans. R. Soc. B* **368**, 20120029 (2012).

[202] Brown, D. A. Lipid rafts, detergent-resistant membranes, and raft targeting signals. *Physiol.* **21**, 430–9 (2006).

[203] Simons, K. & Sampaio, J. L. Membrane organization and lipid rafts. *Cold Spring Harb. Perspect. Biol.* **3**, a004697 (2011).

[204] Bray, A. Theory of phase-ordering kinetics. *Adv. Phys.* **43**, 357–459 (1994).

[205] Arumugam, S. & Bassereau, P. Membrane nanodomains: contribution of curvature and interaction with proteins and cytoskeleton. *Essays Biochem.* **57**, 109–19 (2015).

[206] Turner, M. S., Sens, P. & Socci, N. D. Nonequilibrium raftlike membrane domains under continuous recycling. *Phys. Rev. Lett.* **95**, 168301 (2005).

[207] Foret, L. A simple mechanism of raft formation in two-component fluid membranes. *Eur. Lett.* **71**, 508–514 (2005).

[208] Hancock, J. F. Lipid rafts: contentious only from simplistic standpoints. *Nat. Rev. Mol. Cell Biol.* **7**, 456–62 (2006).

[209] Saffman, P. G. & Delbruck, M. Brownian motion in biological membranes. *Proc. Natl. Acad. Sci. USA* **72**, 3111–3 (1975).

[210] Koshy, T. *Catalan Numbers with Applications* (Oxford University Press, Oxford, 2009).

[211] Baker, G. A. & Graves-Morris, P. *Padé Approximants* (Cambridge University Press, Cambridge, 1996), 2nd edn.